MEASURING STRESS IN THIN FILM - SUBSTRATE SYSTEMS

FEATURING SPATIAL NONUNIFORMITIES

OF FILM THICKNESS AND/OR MISFIT STRAIN

Thesis by

Michal A. Brown

In Partial Fulfillment of the Requirements

for the Degree of

Doctor of Philosophy

California Institute of Technology

Pasadena, CA

2007

(Defended May 25, 2007)

Acknowledgements

Lots of people have helped me get where I am today. Graduate school is not exactly the easiest thing in the world, and without the support of my friends and family I doubt I would have made it through.

So far as actual research goes, I must recognize those who have put forth their own effort to help my work succeed. These include Tae-Soon Park, former postdoc in my group, who taught me all I know about the optical measurements I have used, and answered many silly questions even long after he had finished at Caltech and moved on; Nobumichi Tamura, the beamline scientist who supported my work at the Advanced Light Source at Berkeley National Lab, and put up with phone calls at 3am when the equipment wasn't working - though it inevitably would work as soon as he came in; Ersan Ustundag, who guided me through the first couple of years of graduate school, and Ares Rosakis, who advised me through the rest; Donna Mojahedi - secretaries and administrative assistants actually do rule the world.

Thanks also go to my roommates throughout most of grad school, Alice and Jordan - they put up with a lot. I don't often admit it, but I have appreciated it. Tim, you managed to prod me into getting up and out when I really didn't want to - thanks. Did I mention my family? My parents, who have always encouraged me to achieve whatever goal I set my sights on (and just assumed I could); my sister, Charis, and brother, Ward.

I think this is supposed to take just a page, so for anyone I've forgotten to mention - I do appreciate what support you've given me, I just don't have any more room to say so. Please forgive me. And thanks!

Abstract

A configuration of central importance in many areas of engineering application is a thin film structure composed of one or more materials deposited on a substrate of yet another material. Stress in the thin film is accumulated during each of the many processing steps involved in making such a structure. It is necessary to be able to determine the stress levels and distribution in the thin film, as stress buildup can lead directly to failure and as such it is ultimately related to reliability and process yield. Examples of stress-induced failure include delamination, voiding, and cracking of the thin film.

The easiest and most common way of inferring film stress in a thin film-wafer substrate system due to some process is to measure the curvature of the system before and after that process. The change in curvature then can be directly related to the film stress. The classical relation between film stress and wafer curvature is known as the Stoney formula. The Stoney formula was derived based on a number of fairly restrictive assumptions. These assumptions include, but are not limited to, uniform film thickness and an equibiaxial, spatially uniform misfit strain between the film and substrate. The assumption of constant misfit strain leads to the requirement of spatial uniformity in curvature and stress that does not allow the components to vary across the wafer surface. These assumptions are routinely violated in practice, yet the Stoney formula is still arbitrarily applied. The accuracy of this formula in determining film stress is expected to decrease as spatial nonuniformities in the given system grow.

Recently an analysis was performed in which the assumptions of spatial uniformity in film thickness and misfit strain were relaxed and Stoney-like relations between film stress and wafer curvature were derived. These relations, called the HR relations, have not only terms that relate film stress at a given location to the curvature at that location, but also include additional terms that relate film stress at a given location to integrals of the curvature over the entire wafer surface. Therefore, full-field curvature information is needed in order to accurately determine film stress, even at a single location on the wafer.

The new analysis was validated by comparison with X-ray microdiffraction (XRD). The XRD techniques that were utilized for this validation effort allow both the film stress and the substrate curvature to be measured independently. Since these two measurements are not related, the substrate curvature was used as an input to the stress-curvature relations. The resulting film stresses, from both Stoney and the new HR analysis, were then compared with the film stress data from XRD. It was found that the accuracy of the HR analysis is much greater than that of Stoney, especially near the film edges. Near the edge of the film, the film thickness decreases sharply, which leads to a proportional increase in film stress. This increase is captured by the HR relations but completely missed by Stoney, which assumes a constant film thickness. Within the film center, differences as large as 60% were reported.

Next, a full-field curvature measurement was introduced. Coherent Gradient Sensing is suited to the HR analysis because it produces curvature information over the entire wafer surface, which is required for this analysis. CGS measurements were taken of several progressively more interesting test wafers, which feature various geometries of

W island films on otherwise bare Si wafer substrates. Both Stoney and the HR relations were then used to determine stress in the film. The difference in film stresses produced by the two methodologies was discussed. Also, the variations between film stresses of the different thin film-wafer geometries were examined.

It was found that film stress is not a strictly processing-dependent or an intrinsic material property, but also depends on the location of a thin film feature on the wafer surface. Also, features that are close to each other interact so as to change the wafer deformation and the stress distribution across the film.

Further studies are underway which also consider an additional source of wafer deformation, namely the effects of temperature gradients which can cause permanent deformation in a wafer substrate. This effect is completely separate from those caused by film stress.

Table of Contents

Introduction

A configuration of central importance in many areas of engineering application is a thin-film structure composed of one or more materials deposited on a substrate of yet another material. Integrated electronic circuits, integrated optical devices and optoelectronic circuits, compound semiconductors, micro-electro-mechanical systems (MEMS) deposited on wafers, three-dimensional electronic circuits, systems-on-a-chip structures, lithographic reticles, and flat panel display systems are examples of such thin film structures integrated on various types of plate substrates.

Especially as film thicknesses and other feature dimensions become ever smaller, film stress plays an important role in the manufacturing process because of its cumulative detrimental effect on process yield [1]. Stress is accumulated during each of the hundreds of fabrication and processing steps involved in creating a thin film structure, e.g., sequential film deposition, thermal anneal and subsequent cooling, and etch steps. Examples of known phenomena and processes that build up stresses in thin films include lattice mismatch, chemical reaction, doping by diffusion or implantation, and rapid deposition by evaporation or sputtering. Film stress buildup can lead to failure through many mechanisms, including stress-induced film cracking, buckling and delamination for brittle dielectric films, and through void nucleation and growth for more ductile metal films. Therefore, the accurate measurement and analysis of the film stress and stress distribution associated with each processing step, and modification of the processes as needed, is necessary for establishing appropriate product quality control methodologies.

The easiest, and probably most common, method to determine film stress due to some process is to measure substrate curvature before and after that specific process. The resulting change in curvature is then directly related to the film stress caused by that process. A simple, well-known formula that relates curvature and film stress was derived by G. G. Stoney [2]. Stoney used plate theory to describe a system composed of a thin film of thickness h_f deposited on a much thicker substrate of thickness h_s to derive what is known as the Stoney relation, or Stoney formula:

$$\sigma^f = \frac{E_s h_s^2}{6(1-\nu_s)h_f}\kappa. \tag{0.1}$$

In this formula the subscripts *f* and *s* are used to denote the film and substrate, respectively, while E and ν are the Young's modulus and Poisson ratio, respectively [3]. The film stress, σ_f, is related directly to the change in system curvature, κ. This formula was derived based on several explicit assumptions. These include:

(i) Both the film thickness h_f and the substrate thickness h_s are uniform and $h_f << h_s << R$, where R is the system radius;

(ii) The strains and rotations of the plate system are infinitesimal;

(iii) Both the film and substrate are homogeneous, isotropic, and linearly elastic or thermoelastic;

(iv) The misfit strain state is in-plane isotropic or equi-biaxial ($\varepsilon_{ij} = \varepsilon_m \delta_{ij}$); and

(v) The misfit strain state is spatially constant over the plate system's surface.

The above assumptions naturally result in the following properties of the system:

(vi) The film stress states are in-plane isotropic or equi-biaxial while the out-of-plane direct stress and all shear stresses vanish ($\sigma = \sigma_{xx} = \sigma_{yy}$, $\sigma_{xy} = \sigma_{yx} = 0$);

(vii) The system's curvature components are equi-biaxial, while the twist curvature vanishes in all directions ($\kappa = \kappa_{xx} = \kappa_{yy}$, $\kappa_{xy} = \kappa_{yx} = 0$); and

(viii) All surviving stress and curvature components are spatially constant over the plate system's surface.

Assumptions (iv) and (v), of equi-biaxial, spatially constant misfit strain, cannot be checked directly. However, the system curvature can be measured. An equi-biaxial, spatially constant curvature, as results from these assumptions, corresponds to a substrate deformation that is exactly spherical. That is practically never the case for a real thin film-substrate system. If the deformation is not spherical, the assumptions of equibiaxiality (iv) and of spatial uniformity (v) must necessarily not be met.

In practice, the Stoney formula is often, arbitrarily, applied in cases where these assumptions are violated. To deal with this, the Stoney formula is typically applied in a local fashion, that is, an average stress at each point is determined from the average curvature at that point. This approximation clearly ignores the assumption of spatial uniformity and, therefore, its accuracy is expected to deteriorate as spatial nonuniformities increase.

Over the years, many extensions to the Stoney formula have been derived by various researchers who have relaxed different assumptions made by the original Stoney analysis. Such extensions of the initial formulation include relaxation of the assumption of equi-biaxiality as well as the assumption of small deformations/deflections. A biaxial

form of Stoney, appropriate for anisotropic misfit strain, including different stress values at two different directions and non-zero, in-plane shear stresses, was derived by relaxing the requirement of curvature equi-biaxiality [3]. Related analyses treating discontinuous films in the form of bare periodic lines [4] or composite films with periodic line structures (e.g., bare or encapsulate periodic lines) have also been derived [5-7]. These latter analyses have also removed the requirement of equi-biaxiality and have allowed the existence of three independent curvature and stress components in the form of two, non-equal, direct components and one shear or twist curvature component. However, the uniformity requirement of all of these quantities over the entire plate system was retained. In addition to the above, single, multiple, and graded films and substrates have been treated in various large deformation analyses [8-11]. These analyses have removed both the restrictions of an equi-biaxial curvature state as well as the assumption of infinitesimal deformations. They have allowed for the prediction of kinematically nonlinear behavior and bifurcations in curvature states which have also been observed experimentally [12, 13]. These bifurcations are transformations from an initially equi-biaxial to a subsequently biaxial curvature state that may be induced by an increase in film stress beyond a critical level. This critical level is intimately related to the system's aspect ratio, i.e., the ratio of in-plane to thickness dimension and the elastic stiffness. These analyses also retain the requirement of spatial misfit strain, curvature and stress uniformity across the entire system. However, they allow for deformations to evolve from an initially spherical shape to an energetically favored shape (e.g., ellipsoidal,

cylindrical or saddle shapes) which features three different, yet still spatially constant, curvature components [12, 13].

The most restrictive requirement of the classical Stoney formulations and its extensions discussed above was recently relaxed to derive a more general Stoney-like equation [14-17]. This was done by considering deformations due to a non-uniform misfit strain distribution, where misfit strain refers to the intrinsic strain in the thin film that is not associated with the stress. Initially the analysis was performed by considering a misfit strain due to a non-uniform temperature distribution [14]. The Stoney analysis, which assumes spatially constant misfit strain, produces a relation between film stress and substrate curvature in which the misfit strain is eliminated; that is, the dependence of film stress on substrate curvature is not affected by the origin of the misfit strain. However, it was found that when considering misfit strain due to non-uniform temperature distributions, the resulting Stoney-like relations which associate film stress and substrate curvature did include a term which depended on difference of thermal expansion coefficients of the film and substrate.

The thermoelastic analysis, discussed above, was subsequently repeated for cases where the cause of system curvature and film stress was an athermal misfit strain such as epitaxial lattice mismatch. The first case considered was one of axisymmetric system geometry and misfit strain distribution [15]. This was followed by a generalization to arbitrary misfit strain distributions [16] and finally to both arbitrarily non-uniform film thickness and misfit strain variations. This last analysis is described in detail in chapter 1 of this thesis.

The above analyses produced relations between the dependent variables (film stress and system curvatures) and the in-plane misfit strain distribution. The dependence on misfit strain appeared in the form of integrals evaluated over the plate surface demonstrating the "non-local" nature of the dependence. Elimination of the misfit strain resulted in Stoney-like relations between film stress and system curvatures (referred to here as the HR relations) which also involve surface integrals of curvature evaluated over the place surface. The most interesting feature of the resulting relations is that film stress in a given location does not simply depend on the curvature at that location in a "local" manner. Instead, there are additional terms which depend on the curvature distribution over the entire plate system. This implies a "non-local" stress/curvature dependence and demonstrates that a simple, "local" curvature measurement is not sufficient for an accurate determination of stress in the presence of non-uniform deformations; instead, the full-field curvature is required.

Note that the term "non-local," as used here, applies to the relations between film stress and misfit strain, curvature and misfit strain, and stress and curvature. The formulation, however, is strictly local since only linear elasticity is assumed.

In this thesis, the derivation of the HR relations for both the case of arbitrarily varying non-uniform misfit strains and film thicknesses are summarized and are then specialized to the axisymmetric case. Once the stress/curvature relations are established, their differences from the "local" Stoney relations are discussed by means of an analytical example. In order to validate the non-local HR relations, a micromeasurement technique, X-ray microdiffraction (μXRD), is introduced. This technique is advantageous because it

is able to independently measure both film stress and substrate curvature within the same setup. Measurements of film stress made by μXRD of a highly non-uniform but axisymmetric wafer specimen are compared with the stress inferred by using the local and non-local formulas with curvature, measured by monochromatic μXRD, as a common input. The comparison provides conclusive validation of the axisymmetric version of the non-local stress/curvature relations.

Next, a full-field, interferometric curvature measurement technique, called Coherent Gradient Sensing (CGS), is introduced. This full-field measurement allows the non-local stress formulas, which require knowledge of the entire curvature field over the wafer surface, to be used appropriately. Finally, the full-field CGS technique is used to analyze the stress distributions of several interesting thin film-substrate systems. These systems include various non-axisymmetric geometries of W thin film islands deposited on single crystal Si substrates.

An ongoing collaborative study with Northrop Grumman Space Technologies is also briefly discussed. This study is examining the additional thermal effects of certain processing techniques on wafer deformation and film stress.

1. Theory

The Stoney formula (Eq. 0.1) is commonly used to relate film stress to system curvature. As mentioned in the introduction, the assumptions of this formula include spatial uniformity which does not allow the curvature or stress to vary over the plate system surface. In practice, however, this assumption is rarely met. In order to measure film stress when the system is not spatially uniform, the Stoney formula is often applied in a local manner. This is done by relating the first invariant of the film stress to the first invariant of curvature as follows:

$$\sigma_{xx}^{f} + \sigma_{yy}^{f} = \frac{E_s h_s^2}{6(1+\nu_s)h_f}(\kappa_{xx} + \kappa_{yy}) . \tag{1.1}$$

Note that this clearly violates the assumption of a single, constant curvature and a single, constant stress over the entire wafer.

In order to expand the Stoney formula to properly incorporate non-uniform deformations, an analysis was performed which considers a case in which a non-uniform misfit strain is present in the film [17]. This misfit strain, ε_m, refers to the intrinsic strain in the thin film which is not associated with the stress.

In this analysis, a thin film of arbitrary thickness $h_f(r,\theta)$ has been deposited on a much thicker substrate of uniform thickness h_s, and radius R, such that $h_f << h_s << R$ (Fig. 1-1). The film is modeled as a membrane, since it is too thin to be subject to bending forces. The thin film is subject to a non-uniform and isotropic misfit strain distribution $\varepsilon_{ij}^{m} = \varepsilon_m \delta_{ij}$, where $\varepsilon_m = \varepsilon_m(r,\theta)$. The misfit strain provides the "driving force" which is

ultimately responsible for the creation of both curvature in the system and stress in the thin film. The substrate, which is subject to bending, is modeled as a plate. A cylindrical coordinate system (r,θ,z) is used, with the origin in the center of the substrate (see Fig. 1-1).

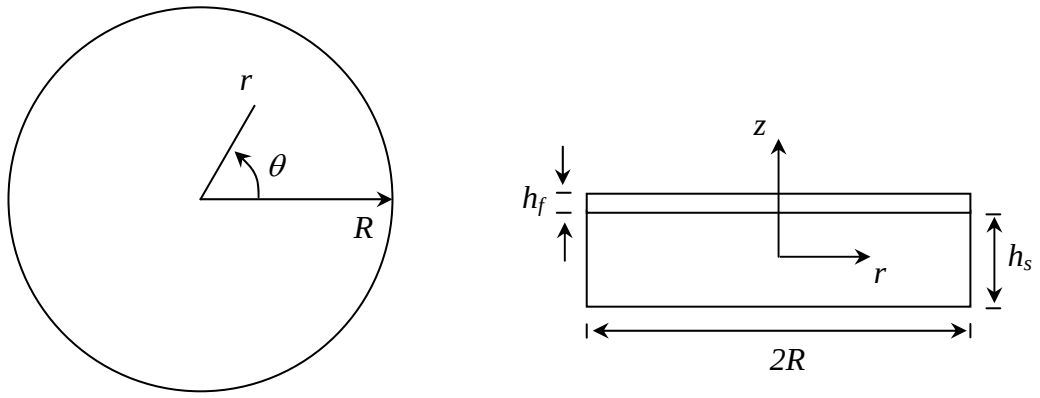

Figure 1-1. Schematic of the thin film-substrate system, showing the cylindrical coordinates (r, θ, z).

The film has radial (r) and circumferential (θ) in-plane displacements of u_r^f and u_θ^f, respectively. The strains in the film are $\varepsilon_{rr} = \partial u_\theta^f / \partial r$, $\varepsilon_{\theta\theta} = u_r^f / r + (1/r)\partial u_\theta^f / \partial\theta$ and $\gamma_{r\theta} = (1/r)\partial u_r^f / \partial\theta + \partial u_\theta^f / \partial r - u_\theta^f / r$. These strains are related to the misfit strain, ε_m, and the film stresses by $\varepsilon_{ij} = \frac{1}{E_f}\left[(1+\nu_f)\sigma_{ij} - \nu_f \sigma_{kk}\delta_{ij}\right] + \varepsilon_m \delta_{ij}$. The stresses in the film can now be expressed in terms of the film displacements as follows:

$$\sigma_{rr}^f = \frac{E_f}{1-\nu_f{}^2}\left[\frac{\partial u_r^f}{\partial r} + \nu_f\left(\frac{u_r^f}{r} + \frac{1}{r}\frac{\partial u_\theta^f}{\partial\theta}\right) - (1+\nu_f)\varepsilon_m\right],$$

$$\sigma_{\theta\theta}^f = \frac{E_f}{1-\nu_f{}^2}\left[\nu_f\frac{\partial u_r^f}{\partial r} + \frac{u_r^f}{r} + \frac{1}{r}\frac{\partial u_\theta^f}{\partial\theta} - (1+\nu_f)\varepsilon_m\right],$$

$$\sigma_{r\theta}^f = \frac{E_f}{2(1+\nu_f)}\left(\frac{1}{r}\frac{\partial u_r^f}{\partial\theta} + \frac{\partial u_\theta^f}{\partial r} - \frac{u_\theta^f}{r}\right). \qquad (1.2)$$

The membrane forces are now defined as

$$N_r^f = h_f \sigma_{rr}^f,\ N_\theta^f = h_f \sigma_{\theta\theta}^f,\ N_{r\theta}^f = h_f \sigma_{r\theta}^f. \tag{1.3}$$

For a uniform misfit strain distribution and uniform film thickness (ε_m, h_f constant), the normal and shear tractions associated with the thin film-substrate interface vanish except near the free edge $r = R$, i.e., $\sigma_{zz} = \sigma_{rz} = \sigma_{\theta z} = 0$ at $z = h_s/2$ and $r < R$. However, for non-uniform misfit strain and film thickness distributions, $\varepsilon_m = \varepsilon_m(r,\theta)$ and $h_f = h_f(r,\theta)$, the shear stresses σ_{rz} and $\sigma_{\theta z}$ at the interface may no longer vanish, and are denoted by τ_r and τ_θ, respectively. The normal stress traction σ_{zz} still vanishes (except at the free edge $r = R$) because the thin film cannot be subject to bending. The equilibrium equations for the film are thus

$$\frac{\partial N_r^f}{\partial r} + \frac{N_r^f - N_\theta^f}{r} + \frac{1}{r}\frac{\partial N_{r\theta}^f}{\partial \theta} - \tau_r = 0,$$

$$\frac{\partial N_{r\theta}^f}{\partial r} + \frac{2}{r} N_{r\theta}^f + \frac{1}{r}\frac{\partial N_\theta^f}{\partial \theta} - \tau_\theta = 0. \tag{1.4}$$

The substitution of Eqs. 1.2 and 1.3 into Eq. 1.4 yields the governing equations for the thin film, in terms of $u_r^{(f)}, u_\theta^{(f)}, \tau_r$ and τ_θ, as

$$\begin{aligned}
&\frac{\partial}{\partial r}\left[h_f\left(\frac{\partial u_r^f}{\partial r} + \frac{u_r^f}{r} - \frac{1}{r}\frac{\partial u_\theta^f}{\partial r}\right)\right] + \frac{1-\nu_f}{2}\frac{h_f}{r^2}\left[\frac{\partial^2 u_r^f}{\partial \theta^2} - \frac{\partial}{\partial r}\left(r\frac{\partial u_\theta^f}{\partial \theta}\right)\right] \\
&+ \frac{1+\nu_f}{2}\left\{\frac{\partial h_f}{\partial \theta}\left[\frac{\partial}{\partial r}\left(\frac{u_\theta^f}{r}\right) + \frac{1}{r^2}\frac{\partial u_r^f}{\partial \theta}\right] - \frac{2}{r}\frac{\partial h_f}{\partial r}\left(u_r^f + \frac{\partial u_\theta^f}{\partial \theta}\right)\right\} \\
&= \frac{1-\nu_f^{\,2}}{E_f}\tau_r + (1+\nu_f)\frac{\partial (h_f \varepsilon_m)}{\partial r},
\end{aligned}$$

$$\frac{1}{r}\frac{\partial}{\partial\theta}\left[h_f\left(\frac{\partial u_r^f}{\partial r}+\frac{u_r^f}{r}-\frac{1}{r}\frac{\partial u_\theta^f}{\partial r}\right)\right]+\frac{1-\nu_f}{2}h_f\left\{-\frac{\partial}{\partial r}\left(\frac{1}{r}\frac{\partial u_r^f}{\partial\theta}\right)+\frac{\partial}{\partial r}\left[\frac{1}{r}\frac{\partial}{\partial r}(ru_\theta^f)\right]\right\}$$
$$+\frac{1-\nu_f}{2}\left\{\frac{\partial h_f}{\partial r}\left[\frac{1}{r}\frac{\partial u_r^f}{\partial\theta}+r\frac{\partial}{\partial r}\left(\frac{u_\theta^f}{r}\right)\right]-\frac{2}{r}\frac{\partial h_f}{\partial\theta}\frac{\partial u_r^f}{\partial r}\right\} \tag{1.5}$$
$$=\frac{1-{\nu_f}^2}{E_f}\tau_\theta+(1+\nu_f)\frac{1}{r}\frac{\partial(h_f\varepsilon_m)}{\partial\theta}.$$

At its neutral axis, $z = 0$, the substrate has radial (r) and circumferential (θ) in-plane displacements of u_r^s and u_θ^s, respectively. Since the substrate undergoes bending, it also has a displacement, w, normal to the neutral axis. The strains in the substrate are then denoted by

$$\varepsilon_{rr}^s=\frac{\partial u_r^s}{\partial r}-z\frac{\partial^2 w}{\partial r^2},$$

$$\varepsilon_{\theta\theta}^s=\frac{u_s^r}{r}-+\frac{1}{r}\frac{\partial u_\theta^s}{\partial\theta}-z\left(\frac{1}{r}\frac{\partial w}{\partial r}+\frac{1}{r^2}\frac{\partial^2 w}{\partial\theta^2}\right),$$

$$\gamma_{r\theta}=\frac{1}{r}\frac{\partial u_r^s}{\partial\theta}+\frac{\partial u_\theta^s}{\partial r}-\frac{u_\theta^s}{r}-2z\frac{\partial}{\partial r}\left(\frac{1}{r}\frac{\partial w}{\partial\theta}\right). \tag{1.6}$$

The stresses are

$$\sigma_{rr}^s=\frac{E_s}{1-{\nu_s}^2}\left\{\frac{\partial u_r^s}{\partial r}+\nu_s\left(\frac{u_r^s}{r}+\frac{1}{r}\frac{\partial u_\theta^s}{\partial\theta}\right)-z\left[\frac{\partial^2 w}{\partial r^2}+\nu_s\left(\frac{1}{r}\frac{\partial w}{\partial r}+\frac{1}{r^2}\frac{\partial^2 w}{\partial\theta^2}\right)\right]\right\},$$

$$\sigma_{\theta\theta}^s=\frac{E_s}{1-{\nu_s}^2}\left[\nu_s\frac{\partial u_r^s}{\partial r}+\frac{u_r^s}{r}+\frac{1}{r}\frac{\partial u_\theta^s}{\partial\theta}-z\left(\nu_s\frac{\partial^2 w}{\partial r^2}+\frac{1}{r}\frac{\partial w}{\partial r}+\frac{1}{r^2}\frac{\partial^2 w}{\partial\theta^2}\right)\right],$$

$$\sigma_{r\theta}^s=\frac{E_s}{2(1+\nu_s)}\left[\frac{1}{r}\frac{\partial u_r^s}{\partial\theta}+\frac{\partial u_\theta^s}{\partial r}-\frac{u_\theta^s}{r}-2z\frac{\partial}{\partial r}\left(\frac{1}{r}\frac{\partial w}{\partial\theta}\right)\right]. \tag{1.7}$$

The forces and bending moments in the substrate are then found to be

$$N_r^s = \int_{-h_s/2}^{h_s/2} \sigma_{rr} dz = \frac{E_s h_s}{1-\nu_s^2}\left[\frac{\partial u_r^s}{\partial r} + \nu_s\left(\frac{u_r^s}{r} + \frac{1}{r}\frac{\partial u_\theta^s}{\partial \theta}\right)\right],$$

$$N_\theta^s = \int_{-h_s/2}^{h_s/2} \sigma_{\theta\theta} dz = \frac{E_s h_s}{1-\nu_s^2}\left(\nu_s \frac{\partial u_r^s}{\partial r} + \frac{u_r^s}{r} + \frac{1}{r}\frac{\partial u_\theta^s}{\partial \theta}\right),$$

$$N_{r\theta}^s = \int_{-h_s/2}^{h_s/2} \sigma_{r\theta} dz = \frac{E_s h_s}{2(1+\nu_s)}\left(\frac{1}{r}\frac{\partial u_r^s}{\partial \theta} + \frac{\partial u_\theta^s}{\partial r} - \frac{u_\theta^s}{r}\right); \tag{1.8}$$

$$M_r^s = -\int_{-h_s/2}^{h_s/2} z\sigma_{rr} dz = \frac{E_s h_s^3}{12(1-\nu_s^2)}\left[\frac{\partial^2 w}{\partial r^2} + \nu_s\left(\frac{1}{r}\frac{\partial w}{\partial r} + \frac{1}{r^2}\frac{\partial^2 w}{\partial \theta^2}\right)\right],$$

$$M_\theta^s = -\int_{-h_s/2}^{h_s/2} z\sigma_{\theta\theta} dz = \frac{E_s h_s^3}{12(1-\nu_s^2)}\left(\nu_s \frac{\partial^2 w}{\partial r^2} + \frac{1}{r}\frac{\partial w}{\partial r} + \frac{1}{r^2}\frac{\partial^2 w}{\partial \theta^2}\right),$$

$$M_{r\theta}^s = -\int_{-h_s/2}^{h_s/2} z\sigma_{r\theta} dz = \frac{E_s h_s^3}{12(1+\nu_s)}\frac{\partial}{\partial r}\left(\frac{1}{r}\frac{\partial w}{\partial \theta}\right). \tag{1.9}$$

The shear stresses τ_r and τ_θ at the thin film-substrate interface are equivalent to the distributed forces τ_r in the radial direction and τ_θ in the circumferential direction, and bending moments $(h_s/2)\tau_r$ and $(h_s/2)\tau_\theta$ applied at the neutral axis ($z = 0$) of the substrate. The in-plane force equilibrium equations for the substrate are then

$$\frac{\partial N_r^s}{\partial r} + \frac{N_r^s - N_\theta^s}{r} + \frac{1}{r}\frac{\partial N_{r\theta}^s}{\partial \theta} + \tau_r = 0,$$

$$\frac{\partial N_{r\theta}^s}{\partial r} + \frac{2}{r}N_{r\theta}^s + \frac{1}{r}\frac{\partial N_{\theta\theta}^s}{\partial \theta} + \tau_\theta = 0, \tag{1.10}$$

and the in-plane bending moment equilibrium equations for the substrate are

$$\frac{\partial M_r}{\partial r}+\frac{M_r-M_\theta}{r}+\frac{1}{r}\frac{\partial M_{r\theta}}{\partial \theta}+Q_r-\frac{h_s}{2}\tau_r=0,$$

$$\frac{\partial M_{r\theta}}{\partial r}+\frac{2}{r}M_{r\theta}+\frac{1}{r}\frac{\partial M_\theta}{\partial \theta}+Q_\theta-\frac{h_s}{2}\tau_\theta=0, \tag{1.11}$$

$$\frac{dQ_r}{dr}+\frac{Q_r}{r}+\frac{1}{r}\frac{\partial Q_\theta}{\partial \theta}=0, \tag{1.12}$$

where Q_r and Q_θ are the shear forces normal to the neutral axis. Substituting Eq. 1.8 into Eq. 1.10 gives the following governing equation for the substrate, in terms of u_r^s and u_θ^s (and τ), as

$$\frac{\partial}{\partial r}\left(\frac{\partial u_r^s}{\partial r}+\frac{u_r^s}{r}+\frac{1}{r}\frac{\partial u_\theta^s}{\partial \theta}\right)+\frac{1-\nu_s}{2}\frac{1}{r^2}\left[\frac{\partial^2 u_r^s}{\partial \theta^2}-\frac{\partial}{\partial r}\left(r\frac{\partial u_\theta^s}{\partial \theta}\right)\right]=-\frac{1-\nu_s^{\,2}}{E_s h_s}\tau_r,$$

$$\frac{1}{r}\frac{\partial}{\partial \theta}\left(\frac{\partial u_r^s}{\partial r}+\frac{u_r^s}{r}+\frac{1}{r}\frac{\partial u_\theta^s}{\partial \theta}\right)+\frac{1-\nu_s}{2}\left\{-\frac{\partial}{\partial r}\left(\frac{1}{r}\frac{\partial u_r^s}{\partial \theta}\right)+\frac{\partial}{\partial r}\left[\frac{1}{r}\frac{\partial}{\partial r}(ru_\theta^s)\right]\right\}=-\frac{1-\nu_s^{\,2}}{E_s h_s}\tau_\theta. \tag{1.13}$$

Similarly, substituting Eq. 1.9 into Eq. 1.10, and eliminating Q_r and Q_θ from Eq. 1.11, gives the governing equations for the substrate, in terms of *w* (and τ), as

$$\nabla^2\left(\nabla^2 w\right)=\frac{6\left(1-\nu_s^{\,2}\right)}{E_s h_s^{\,2}}\left(\frac{\partial \tau_r}{\partial r}+\frac{\tau_r}{r}+\frac{1}{r}\frac{\partial \tau_\theta}{\partial \theta}\right), \tag{1.14}$$

where $\nabla^2=\frac{\partial^2}{\partial r^2}+\frac{1}{r}\frac{\partial}{\partial r}+\frac{1}{r^2}\frac{\partial^2}{\partial \theta^2}$.

Also, from continuity of displacement at the thin film-substrate interface, the condition is imposed that

$$u_r^f = u_r^s - \frac{h_s}{2}\frac{\partial w}{\partial r},\ u_\theta^f = u_\theta^s - \frac{h_s}{2}\frac{1}{r}\frac{\partial w}{\partial \theta}. \tag{1.15}$$

Equtions 1.5 and 1.13-1.15 constitute seven ordinary differential equations for seven variables, namely u_r^f, u_θ^f, u_r^s, u_θ^s,w, τ_r and τ_θ. The following discussion explains how to decouple these seven equations under the limit $h_f/h_s << 1$ in order to solve u_r^s and u_θ^s first, then w, followed by u_r^f and u_θ^f, and finally τ_r and τ_θ.

(i) Elimination of τ_r and τ_θ from force-equilibrium equations for the thin film (Eq. 1.5) and for the substrate (Eq. 1.13) yields two equations for u_r^f, u_θ^f, u_r^s, and u_θ^s. Under the limit $h_f/h_s << 1$, u_r^f and u_θ^f disappear in these two equations, which become the following governing equations for u_r^s and u_θ^s only:

$$\begin{aligned}
&\frac{\partial}{\partial r}\left(\frac{\partial u_r^s}{\partial r} + \frac{u_r^s}{r} + \frac{1}{r}\frac{\partial u_\theta^s}{\partial \theta}\right) + \frac{1-\nu_s}{2}\frac{1}{r^2}\left[\frac{\partial^2 u_r^s}{\partial \theta^2} - \frac{\partial}{\partial r}\left(r\frac{\partial u_\theta^s}{\partial \theta}\right)\right] \\
&= \frac{E_f}{1-\nu_f}\frac{1-\nu_s{}^2}{E_s h_s}\frac{\partial (h_f \varepsilon_m)}{\partial r} + O\left(\frac{h_f^2}{h_s^2}\right),
\end{aligned}$$

$$\begin{aligned}
&\frac{1}{r}\frac{\partial}{\partial \theta}\left(\frac{\partial u_r^s}{\partial r} + \frac{u_r^s}{r} + \frac{1}{r}\frac{\partial u_\theta^s}{\partial \theta}\right) + \frac{1-\nu_s}{2}\left\{-\frac{\partial}{\partial r}\left(\frac{1}{r}\frac{\partial u_r^s}{\partial \theta}\right) + \frac{\partial}{\partial r}\left[\frac{1}{r}\frac{\partial}{\partial r}(r u_\theta^s)\right]\right\} \\
&= \frac{E_f}{1-\nu_f}\frac{1-\nu_s{}^2}{E_s h_s}\frac{1}{r}\frac{\partial (h_f \varepsilon_m)}{\partial \theta} + O\left(\frac{h_f^2}{h_s^2}\right).
\end{aligned} \tag{1.16}$$

The substrate displacements u_r^s and u_θ^s are on the order of h_f / h_s.

(ii) Elimination of u_r^f and u_θ^f from the continuity condition (Eq. 1.15) and equilibrium equation (Eq. 1.5) for the thin film gives τ_r and τ_θ in terms of u_r^s, u_θ^s and w (and ε_m). The substitution of these τ_r and τ_θ into the moment equilibrium equation (Eq.

1.14) yields the governing equation for the normal displacement *w*. For $h_f / h_s << 1$, this governing equation takes the form

$$\nabla^2\left(\nabla^2 w\right) = -6\frac{E_f}{1-\nu_f}\frac{1-\nu_s^{\,2}}{E_s h_s^{\,2}}\nabla^2(h_f \varepsilon_m)\,. \tag{1.17}$$

This is a biharmonic equation which can be solved analytically. The substrate displacement *w* is on the order of h_f / h_s.

(iii) The displacements u_r^f and u_θ^f in the thin film are obtained from Eq. 1.15, and they are also on the same order h_f / h_s as u_r^s, u_θ^s and *w*. The leading terms of the interface shear stresses τ_r and τ_θ are then obtained from Eq. 1.5 as

$$\tau_r = -\frac{E_f}{1-\nu_f}\frac{\partial(h_f \varepsilon_m)}{\partial r},\ \tau_\theta = -\frac{E_f}{1-\nu_f}\frac{1}{r}\frac{\partial(h_f \varepsilon_m)}{\partial \theta}. \tag{1.18}$$

Equations 1.16 - 1.18 show that h_f always appears together with ε_m. The interface shear stress is only proportional to gradients of $h_f\varepsilon_m$; when the misfit strain and film thickness are uniform, as is the case for the Stoney analysis, the interface shear stress vanishes. This result holds regardless of boundary conditions at *r* = *R*.

The boundary conditions at the free edge r = R require that the net forces and moments vanish:

$$N_r^f + N_r^s = 0 \text{ and } N_{r\theta}^f + N_{r\theta}^s = 0\,, \tag{1.19}$$

$$M_r - \frac{h_s}{2}N_r^f = 0 \text{ and } Q_r - \frac{1}{r}\frac{\partial}{\partial\theta}\left(M_{r\theta} - \frac{h_s}{2}N_{r\theta}^f\right) = 0\,. \tag{1.20}$$

Equations 1.16 - 1.18 and boundary conditions 1.19 - 1.20 are solved in the same way as that for uniform thickness and non-uniform misfit strain [16] by replacing ε_m with $h_f\varepsilon_m$. Then $h_f\varepsilon_m$ is expanded to the Fourier series as

$$h_f\varepsilon_m(r,\theta)=\sum_{n=0}^{\infty}(h_f\varepsilon_m)_c^n(r)\cos n\theta+\sum_{n=1}^{\infty}(h_f\varepsilon_m)_s^n(r)\sin n\theta\,, \tag{1.21}$$

where $(h_f\varepsilon_m)_c^0(r)=\dfrac{1}{2\pi}\int_0^{2\pi}h_f\varepsilon_m d\theta$, $(h_f\varepsilon_m)_c^n(r)=\dfrac{1}{\pi}\int_0^{2\pi}h_f\varepsilon_m\cos n\theta\,d\theta\ \ (n\ge 1)$ and

$(h_f\varepsilon_m)_s^n(r)=\dfrac{1}{\pi}\int_0^{2\pi}h_f\varepsilon_m\sin n\theta\,d\theta\ \ (n\ge 1)$.

Now the system curvatures $\kappa_{rr}=\dfrac{\partial^2 w}{\partial r^2}$, $\kappa_{\theta\theta}=\dfrac{1}{r}\dfrac{\partial w}{\partial r}+\dfrac{1}{r^2}\dfrac{\partial^2 w}{\partial\theta^2}$, and $\kappa_{r\theta}=\dfrac{\partial}{\partial r}\left(\dfrac{1}{r}\dfrac{\partial w}{\partial\theta}\right)$ are related to $h_f\varepsilon_m$ by

$$\kappa_{rr}+\kappa_{\theta\theta}=-12\,\frac{E_f}{1-\nu_f}\,\frac{1-\nu_s}{E_s h_s^{\,2}} *\left\{\begin{array}{l} h_f\varepsilon_m-\dfrac{1-\nu_s}{2}\left(h_f\varepsilon_m-\overline{h_f\varepsilon_m}\right) \\ +\dfrac{1-\nu_s^2}{3+\nu_s}\displaystyle\sum_{n=1}^{\infty}(n+1)\frac{r^n}{R^{2n+2}}\left[\begin{array}{l}\cos n\theta\displaystyle\int_0^R\eta^{n+1}(h_f\varepsilon_m)_c^n(\eta)d\eta \\ +\sin n\theta\displaystyle\int_0^R\eta^{n+1}(h_f\varepsilon_m)_s^n(\eta)d\eta\end{array}\right]\end{array}\right\}, \tag{1.22a}$$

$$\kappa_{rr}-\kappa_{\theta\theta}=-6\frac{E_f}{1-\nu_f}\frac{1-\nu_s^{\,2}}{E_s h_s^{\,2}}$$

$$*\left\{\begin{array}{l} h_f\varepsilon_m-\dfrac{2}{r^2}\displaystyle\int_0^r \eta(h_f\varepsilon_m)_c^0\,d\eta \\ +\dfrac{1-\nu_s}{3+\nu_s}\displaystyle\sum_{n=1}^{\infty}\frac{n+1}{R^{n+2}}\left[n\frac{r^n}{R^n}-(n-1)\frac{r^{n-2}}{R^{n-2}}\right]\left(\begin{array}{l}\cos n\theta\displaystyle\int_0^R \eta^{n+1}(h_f\varepsilon_m)_c^n\,d\eta \\ +\sin n\theta\displaystyle\int_0^R \eta^{n+1}(h_f\varepsilon_m)_s^n\,d\eta\end{array}\right) \\ -\displaystyle\sum_{n=1}^{\infty}\frac{n+1}{r^{n+2}}\left(\cos n\theta\int_0^r \eta^{n+1}(h_f\varepsilon_m)_c^n\,d\eta+\sin n\theta\int_0^r \eta^{n+1}(h_f\varepsilon_m)_s^n\,d\eta\right) \\ -\displaystyle\sum_{n=1}^{\infty}(n-1)r^{n-2}\left(\cos n\theta\int_r^R \eta^{1-n}(h_f\varepsilon_m)_c^n\,d\eta+\sin n\theta\int_r^R \eta^{1-n}(h_f\varepsilon_m)_s^n\,d\eta\right)\end{array}\right\},\quad(1.22b)$$

$$\kappa_{r\theta}=3\frac{E_f}{1-\nu_f}\frac{1-\nu_s^{\,2}}{E_s h_s^{\,2}}$$

$$*\left\{\begin{array}{l} \dfrac{1-\nu_s}{3+\nu_s}\displaystyle\sum_{n=1}^{\infty}\frac{n+1}{R^{n+2}}\left[n\frac{r^n}{R^n}-(n-1)\frac{r^{n-2}}{R^{n-2}}\right]\left(\begin{array}{l}\sin n\theta\displaystyle\int_0^R \eta^{n+1}(h_f\varepsilon_m)_c^n\,d\eta \\ -\cos n\theta\displaystyle\int_0^R \eta^{n+1}(h_f\varepsilon_m)_s^n\,d\eta\end{array}\right) \\ +\displaystyle\sum_{n=1}^{\infty}\frac{n+1}{r^{n+2}}\left(\sin n\theta\int_0^r \eta^{n+1}(h_f\varepsilon_m)_c^n\,d\eta-\cos n\theta\int_0^r \eta^{n+1}(h_f\varepsilon_m)_s^n\,d\eta\right) \\ -\displaystyle\sum_{n=1}^{\infty}(n-1)r^{n-2}\left(\sin n\theta\int_r^R \eta^{1-n}(h_f\varepsilon_m)_c^n\,d\eta-\cos n\theta\int_r^R \eta^{1-n}(h_f\varepsilon_m)_s^n\,d\eta\right)\end{array}\right\},\quad(1.22c)$$

where $\overline{h_f\varepsilon_m}=\dfrac{1}{\pi R^2}\displaystyle\iint_A h_f\varepsilon_m(\eta,\varphi)dA$ is the average misfit strain over the entire area A of the thin film, $dA=\eta d\eta d\varphi$, and $\overline{h_f\varepsilon_m}$ is also related to $(h_f\varepsilon_m)_c^0$ by

$$\overline{h_f\varepsilon_m}=\frac{2}{R^2}\int_0^R \eta(h_f\varepsilon_m)_c^0(\eta)d\eta\,.$$

The stresses in the thin film are obtained from Eq. 1.2. Specifically, the sum of film stresses, $\sigma_{rr}^{f}+\sigma_{\theta\theta}^{f}$, is related to $h_f\varepsilon_m$ by

$$\sigma_{rr}^{f}+\sigma_{\theta\theta}^{f}=\frac{E_f}{1-\nu_f}(-2\varepsilon_m)\,. \tag{1.23a}$$

The difference between stresses, $\sigma_{rr}^{f}-\sigma_{\theta\theta}^{f}$, and the shear stress, $\sigma_{r\theta}^{f}$, are given by

$$\begin{aligned}\sigma_{rr}^{f}-\sigma_{\theta\theta}^{f}=4E_f\,&\frac{E_f}{1-\nu_f{}^2}\frac{1-\nu_s{}^2}{E_s h_s}\\ &*\left\{\begin{array}{l} h_f\varepsilon_m-\dfrac{2}{r^2}\displaystyle\int_0^r \eta(h_f\varepsilon_m)_c^0\,d\eta \\ -\displaystyle\sum_{n=1}^{\infty}\frac{n+1}{r^{n+2}}\left(\cos n\theta\int_0^r \eta^{n+1}(h_f\varepsilon_m)_c^n\,d\eta+\sin n\theta\int_0^r \eta^{n+1}(h_f\varepsilon_m)_s^n\,d\eta\right) \\ -\displaystyle\sum_{n=1}^{\infty}(n-1)r^{n-2}\left(\cos n\theta\int_r^R \eta^{1-n}(h_f\varepsilon_m)_c^n\,d\eta+\sin n\theta\int_r^R \eta^{1-n}(h_f\varepsilon_m)_s^n\,d\eta\right) \\ -\dfrac{\nu_s}{3+\nu_s}\displaystyle\sum_{n=1}^{\infty}\frac{n+1}{R^{n+2}}\left[n\frac{r^n}{R^n}-(n-1)\frac{r^{n-2}}{R^{n-2}}\right]\left(\begin{array}{l}\cos n\theta\displaystyle\int_0^R \eta^{n+1}(h_f\varepsilon_m)_c^n\,d\eta \\ +\sin n\theta\displaystyle\int_0^R \eta^{n+1}(h_f\varepsilon_m)_s^n\,d\eta\end{array}\right)\end{array}\right\}\end{aligned} \tag{1.23b}$$

$$\sigma_{r\theta}^{f} = 2E_f \frac{E_f}{1-\nu_f^{\,2}} \frac{1-\nu_s^2}{E_s h_s}$$

$$* \left\{ \begin{array}{l} -\sum_{n=1}^{\infty} \frac{n+1}{r^{n+2}} \left(\sin n\theta \int_0^r \eta^{n+1} (h_f \varepsilon_m)_c^n \, d\eta - \cos n\theta \int_0^r \eta^{n+1} (h_f \varepsilon_m)_s^n \, d\eta \right) \\ +\sum_{n=1}^{\infty} (n-1) r^{n-2} \left(\sin n\theta \int_r^R \eta^{1-n} (h_f \varepsilon_m)_c^n \, d\eta - \cos n\theta \int_r^R \eta^{1-n} (h_f \varepsilon_m)_s^n \, d\eta \right) \\ +\frac{\nu_s}{3+\nu_s} \sum_{n=1}^{\infty} \frac{n+1}{R^{n+2}} \left[n \frac{r^n}{R^n} - (n-1) \frac{r^{n-2}}{R^{n-2}} \right] \left(\begin{array}{l} \sin n\theta \int_0^R \eta^{n+1} (h_f \varepsilon_m)_c^n \, d\eta \\ -\cos n\theta \int_0^R \eta^{n+1} (h_f \varepsilon_m)_s^n \, d\eta \end{array} \right) \end{array} \right\} . \quad (1.23c)$$

Note that if the film thickness and misfit strain are uniform, the shear stress of Eq. 1.18 vanishes. Then the curvatures of Eqs. 1.22 become

$$\kappa = \kappa_{rr} = \kappa_{\theta\theta} = -6 \frac{E_f h_f}{1-\nu_f} \frac{1-\nu_s}{E_s h_s^{\,2}} \varepsilon_m, \quad \kappa_{r\theta} = 0, \quad (1.24)$$

and the stresses in the thin film obtained from Eqs. 1.23 become

$$\sigma^f = \sigma_{rr}^f = \sigma_{\theta\theta}^f = \frac{E_f}{1-\nu_f} (-\varepsilon_m), \quad \sigma_{r\theta}^f = 0. \quad (1.25)$$

For this special case only, both stress and curvature states become equibiaxial. The elimination of misfit strain ε_m from the above two equations yields a simple relation $\sigma^f = \frac{E_s h_s^2}{6(1-\nu_s) h_f} \kappa$, which is exactly the Stoney formula in Eq. 0.1.

In order to extend such a Stoney-like relation for arbitrary non-axisymmetric misfit strain distribution, it is necessary to relate curvatures directly to stress. Currently

both curvature and stress are related to the misfit strain distribution in Eqs. 1.22 - 1.23, so eliminating misfit strain from these equations will produce an extension to the Stoney formula.

The coefficients C_n and S_n related to the substrate curvatures are first defined by

$$\begin{aligned} C_n &= \frac{1}{\pi R^2}\iint_A \left(\kappa_{rr}+\kappa_{\theta\theta}\right)\left(\frac{\eta}{R}\right)^n \cos n\varphi dA, \\ S_n &= \frac{1}{\pi R^2}\iint_A \left(\kappa_{rr}+\kappa_{\theta\theta}\right)\left(\frac{\eta}{R}\right)^n \sin n\varphi dA, \end{aligned} \tag{1.26}$$

where the integration is over the entire area A of the thin film, and $dA = \eta d\eta d\varphi$. Since both the substrate curvatures and film stresses depend on the misfit strain ε_m and film thickness h_f, elimination of these parameters gives the film stress in terms of substrate curvatures as

$$\sigma_{rr}^f - \sigma_{\theta\theta}^f = -\frac{E_f h_s}{6(1+\nu_f)}\left\{\begin{array}{l} 4\left(\kappa_{rr}-\kappa_{\theta\theta}\right) \\ -\sum_{n=1}^{\infty}(n+1)\left[n\left(\frac{r}{R}\right)^n-(n-1)\left(\frac{r}{R}\right)^{n-2}\right]\left(C_n\cos n\theta + S_n \sin n\theta\right) \end{array}\right\}, \tag{1.27a}$$

$$\sigma_{r\theta}^f = -\frac{E_f h_s}{6(1+\nu_f)}\left\{4\kappa_{r\theta}+\frac{1}{2}\sum_{n=1}^{\infty}(n+1)\left[n\left(\frac{r}{R}\right)^n-(n-1)\left(\frac{r}{R}\right)^{n-2}\right]\left(C_n\sin n\theta - S_n\cos n\theta\right)\right\}, \tag{1.27b}$$

$$\sigma_{rr}^f + \sigma_{\theta\theta}^f = \frac{E_s h_s^2}{6h_f(1-\nu_s)}\left[\begin{array}{l} \kappa_{rr}+\kappa_{\theta\theta}+\frac{1-\nu_s}{1+\nu_s}\left(\kappa_{rr}+\kappa_{\theta\theta}-\overline{\kappa_{rr}+\kappa_{\theta\theta}}\right) \\ -\frac{1-\nu_s}{1+\nu_s}\sum_{n=1}^{\infty}(n+1)\left(\frac{r}{R}\right)^n\left(C_n\cos n\theta + S_n\sin n\theta\right) \end{array}\right], \tag{1.27c}$$

where $\overline{\kappa_{rr}+\kappa_{\theta\theta}} = C_0 = \iint_A (\kappa_{rr}+\kappa_{\theta\theta})dA/\pi R^2$ is the average curvature over the entire area A of the thin film, and C_n and S_n are given in Eq. 1.26. Equations 1.27, which directly relate film stress to substrate curvatures, are known as the HR relations. It is important to note that stresses at a point in the thin film depend not only on curvatures at the same point (local dependence), but also on the curvatures in the entire substrate (non-local dependence) via the coefficients C_n and S_n. It should also be noted that Eq. 1.27b for shear stress $\sigma_{r\theta}^f$ and Eq. 1.27a for the difference in normal stresses $\sigma_{rr}^f - \sigma_{\theta\theta}^f$ are independent of the thin film thickness h_f, but Eq. 1.27c for the sum or normal stresses $\sigma_{rr}^f + \sigma_{\theta\theta}^f$ is inversely proportional to the local film thickness h_f at the same point.

The interface shear stresses τ_r and τ_θ are also directly related to substrate curvatures via

$$\tau_r = \frac{E_s h_s^2}{6(1-\nu_s^2)}\left[\frac{\partial}{\partial r}(\kappa_{rr}+\kappa_{\theta\theta}) - \frac{1-\nu_s}{2R}\sum_{n=1}^{\infty} n(n+1)(C_n\cos n\theta + S_n \sin n\theta)\left(\frac{r}{R}\right)^{n-1}\right],$$

$$\tau_\theta = \frac{E_s h_s^2}{6(1-\nu_s^2)}\left[\frac{1}{r}\frac{\partial}{\partial \theta}(\kappa_{rr}+\kappa_{\theta\theta}) + \frac{1-\nu_s}{2R}\sum_{n=1}^{\infty} n(n+1)(C_n\sin n\theta - S_n \cos n\theta)\left(\frac{r}{R}\right)^{n-1}\right], \quad (1.28)$$

which is also independent of the film thickness h_f. Equation 1.28 provides a way to estimate the interface shear stresses from the gradients of substrate curvatures. It also displays a non-local dependence via the coefficients C_n and S_n.

Since interfacial shear stresses are responsible for promoting system failures through delamination of the thin film from the substrate, Eq. 1.28 has particular

significance. It shows that such stresses are related to the gradients of $\kappa_{rr} + \kappa_{\theta\theta}$ and not to its magnitude as might have been expected of a local, Stoney-like formulation. Equation 1.28 provides an easy way of inferring these special interfacial shear stresses once the full-field curvature information is available. As a result, the methodology also provides a way to evaluate the risk of and to mitigate such important forms of failure. It should be noted that for the special case of spatially constant curvatures, the interfacial shear stresses vanish as is the case for all Stoney-like formulations described in the introduction.

The HR relations (Eq. 1.27) show a non-local dependence of film stress on substrate curvature, that is, when a non-uniform misfit strain distribution exists, the stress as a given point is related to not just the curvature at that point but also the difference between that curvature and the average curvature across the wafer. The presence of non-local contributions in these relations has implications regarding the nature of diagnostic methods needed to perform wafer-level film stress measurements. In the presence of non-uniform curvatures, a local curvature measurement, i.e., a measurement at a single point, simply does not provide sufficient information to determine the local stress, i.e., the stress at that point. The existence of non-local terms in these relations necessitates the use of full-field methods capable of measuring curvature components over the entire surface of the plate system (or wafer). Furthermore, measurement of all independent components of the curvature field is necessary because the stress state at a point depends on curvature contributions (κ_{rr}, $\kappa_{\theta\theta}$, and $\kappa_{r\theta}$) from the entire plate surface.

The present analysis also provides a very simple way to account for the effect of non-uniform film thickness on the Stoney formula. The most remarkable result is that for

arbitrarily non-uniform film thickness, the stress-curvature relations are identical to their counterparts for uniform film thickness [16, 17] except that thickness is replaced by its local value.

Axisymmetric HR Relations

In this section, the HR relations (Eq. 1.27) are simplified for a radially symmetric misfit strain [15]. The axisymmetric case is considered because the deformation of actual thin film-substrate systems often has radial symmetry, which implies a radially symmetric misfit strain. This is partially due to the circular wafers, and partially to the axisymmetric effects from many of the processing steps, such as heating and cooling processes. A full-field curvature measurement of a typical 300 mm patterned wafer, which illustrates its axisymmetry, is shown in Fig. 1-2.

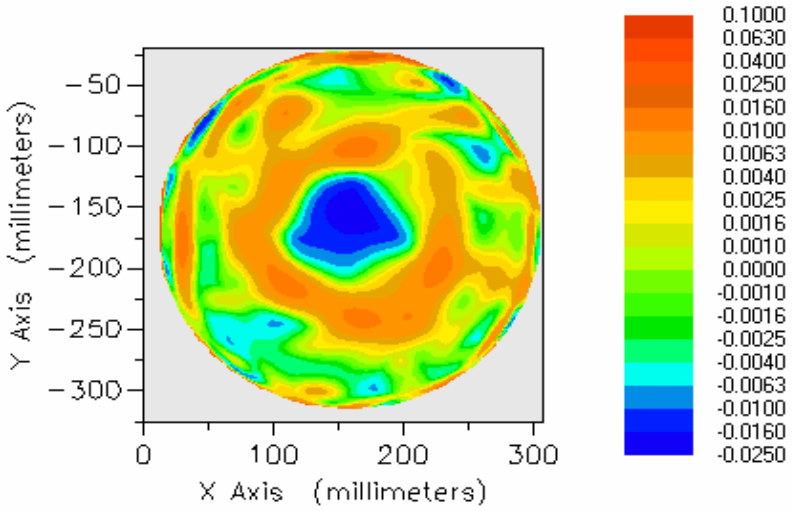

Figure 1-2. Principal curvature, κ_{max}. This curvature is axisymmetric, implying that the deformation is also radially symmetric.

For the axisymmetric case, much of the analysis is simplified. For example, the radial in-plane displacement becomes $u = u(r)$ for film and substrate. In the subsequent equations, all partial derivatives with respect to θ vanish, as do the cross derivatives.

Since a radially symmetric misfit strain has no θ terms, the Fourier series expansion of Eq. 1.21 reduces directly back to $h_f\varepsilon_m$: the leading term $(h_f\varepsilon_m)_c^0(r) = \int_0^{2\pi} h_f\varepsilon_m d\theta\ /(2\pi)$ is $h_f\varepsilon_m$, while the $(h_f\varepsilon_m)_c^n(r) = \int_0^{2\pi} h_f\varepsilon_m \cos n\theta d\theta/\pi$ and $(h_f\varepsilon_m)_s^n(r) = \int_0^{2\pi} h_f\varepsilon_m \sin n\theta d\theta/\pi$ terms both vanish.

The curvatures of Eq. 1.22 then simplify to

$$\kappa_{rr} + \kappa_{\theta\theta} = -12\frac{E_f h_f}{1-\nu_f}\frac{1-\nu_s}{E_s h_s^{\,2}}\left[\varepsilon_m + \frac{1-\nu_s}{2}(\varepsilon_m - \bar{\varepsilon}_m)\right],$$

$$\kappa_{rr} - \kappa_{\theta\theta} = -6\frac{E_f h_f}{1-\nu_f}\frac{1-\nu_s^{\,2}}{E_s h_s^{\,2}}\left[\varepsilon_m - \frac{2}{r^2}\int_0^r \eta\varepsilon_m(\eta)d\eta\right],$$

$$\kappa_{r\theta} = 0\,, \tag{1.29}$$

where $\bar{\varepsilon}_m \equiv (2/R^2)\int_0^R \eta\varepsilon_m(\eta)d\eta = \iint \varepsilon_m dA/(\pi R^2)$.

The stresses of Eq. 1.23 simplify to

$$\sigma_{rr}^f + \sigma_{\theta\theta}^f = \frac{E_f}{1-\nu_f}(-2\varepsilon_m)\ ,$$

$$\sigma_{rr}^f - \sigma_{\theta\theta}^f = 4E_f\,\frac{E_f}{1-\nu_f^{\,2}}\frac{1-\nu_s^{\,2}}{E_s h_s}\left[\varepsilon_m - \frac{2}{r^2}\int_0^r \eta\varepsilon_m(\eta)d\eta\right],$$

$$\sigma_{r\theta}^f = 0\ . \tag{1.30}$$

The coefficients C_n and S_n of Eq. 1.26 also vanish. Thus, the relations between film stress and substrate curvature (Eq. 1.27) become

$$\sigma_{rr}^{f} - \sigma_{\theta\theta}^{f} = -\frac{2E_f h_s}{3(1+\nu_f)}(\kappa_{rr} - \kappa_{\theta\theta}),$$

$$\sigma_{rr}^{f} + \sigma_{\theta\theta}^{f} = \frac{E_s h_s^2}{6(1+\nu_s)h_f}\left\{\kappa_{rr} + \kappa_{\theta\theta} + \frac{1-\nu_s}{1+\nu_s}\left[\kappa_{rr} + \kappa_{\theta\theta} - \overline{\kappa_{rr} + \kappa_{\theta\theta}}\right]\right\},$$

$$\sigma_{r\theta}^{f} = 0, \tag{1.31}$$

while the shear stress Eq. 1.28 simplifies to

$$\tau_r = \frac{E_s h_s{}^2}{6(1-\nu_s{}^2)}\frac{d}{dr}(\kappa_{rr} + \kappa_{\theta\theta}),$$

$$\tau_\theta = 0. \tag{1.32}$$

Note that there is still a non-local dependence of film stress on substrate curvature through the average curvature term $\overline{\kappa_{rr} + \kappa_{\theta\theta}}$.

Both the full HR relations (Eq. 1.27) and the axisymmetric, simplified HR relations (Eq. 1.31) will be used in this thesis.

An Analytical Example: Stoney vs. HR Relations

To illustrate the difference between the local Stoney formula and the new HR relations, consider a thin film-substrate system which is assumed to feature an out-of-plane displacement, *w*, due to some film stress, where

$$w = w_0\left(\frac{r}{R}\right)^n \cos n\theta, \tag{1.33}$$

w_0 is the maximum displacement, and *n* is an integer. For *n* = 2, this displacement corresponds to a saddle shape (Fig. 1-3).

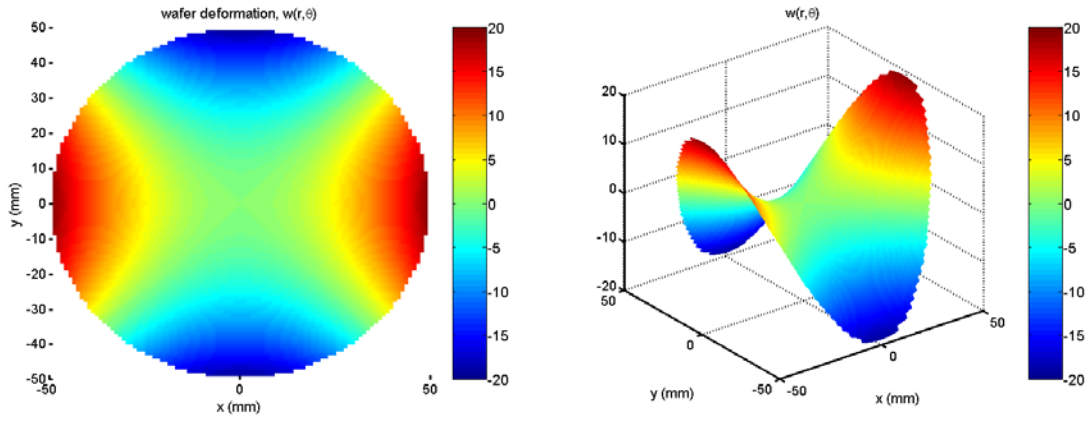

(a) (b)

Figure 1-3. Wafer deformation from Eq. 1.33, where $w_0 = 20$, $n = 2$, and $R = 37$.

Analytically, such a displacement gives curvatures of

$$\kappa_{rr} = -\kappa_{\theta\theta} = n(n-1)\frac{w_0}{R^2}\left(\frac{r}{R}\right)^{n-2}\cos n\theta, \quad \kappa_{r\theta} = -n(n-1)\frac{w_0}{R^2}\left(\frac{r}{R}\right)^{n-2}\sin n\theta\,, \quad (1.34)$$

which are shown in Fig. 1-4.

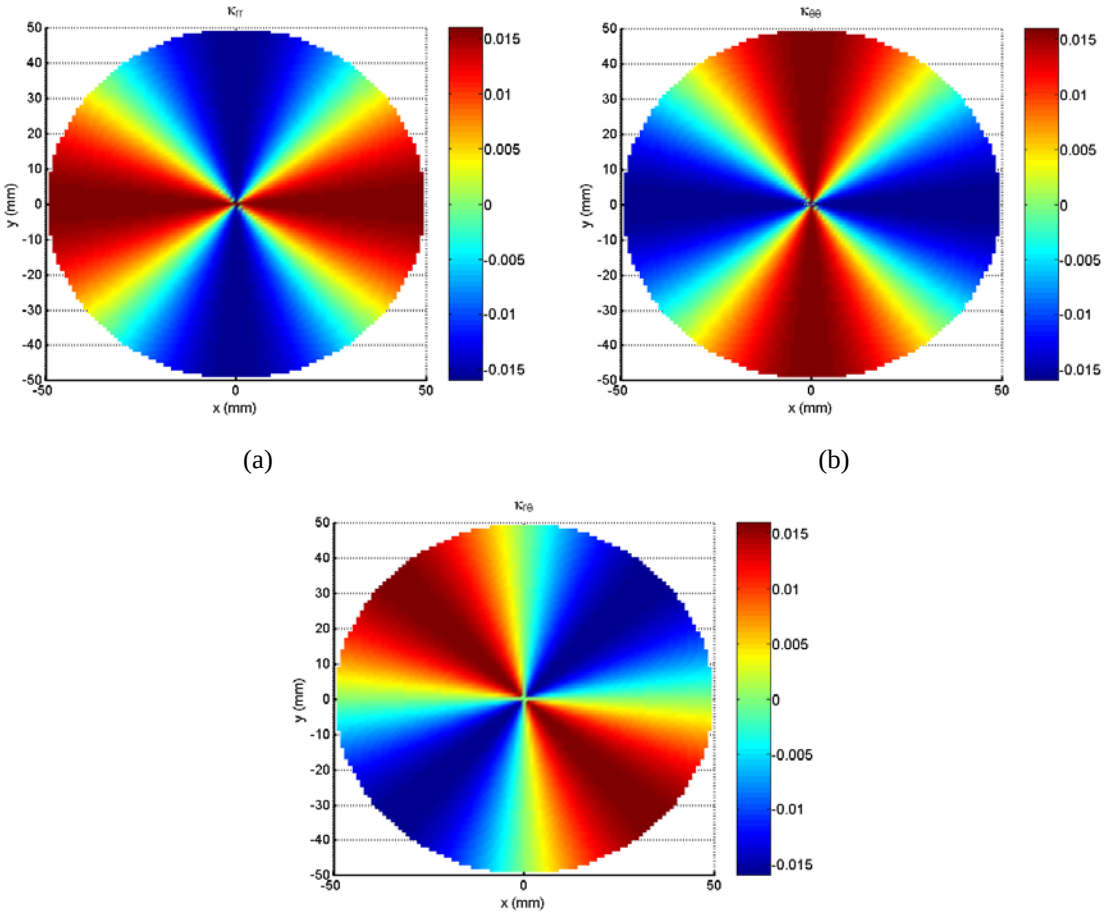

(a) (b)

(c)

Figure 1-4. κ_{rr}, $\kappa_{\theta\theta}$, and $\kappa_{r\theta}$ from Eq. 1.34

Since the radial and circumferential curvatures are equal and opposite, the localized Stoney formula (Eq. 1.1) predicts a vanishing stress state:

$$\begin{aligned}\sigma_{rr}^{f}+\sigma_{\theta\theta}^{f} &= \frac{E_s h_s^2}{6(1-\nu_s)h_f}(\kappa_{rr}+\kappa_{\theta\theta}) \\ &= \frac{E_s h_s^2}{6(1-\nu_s)h_f} n(n-1)\frac{w_0}{R^2}\left(\frac{r}{R}\right)^{n-2}\cos n\theta \times (1-1) \\ &= 0.\end{aligned} \tag{1.35}$$

The HR relations (Eq. 1.27), however, infer stresses that do not vanish and are given by

$$\sigma_{rr}^{(f)} = -\sigma_{\theta\theta}^{(f)} = -\frac{2E_f h_s}{3(1+\nu_f)} n(n-1)\frac{w_0}{R^2}\left(\frac{r}{R}\right)^{n-2} \cos n\theta\,, \tag{1.36}$$

$$\sigma_{r\theta}^{(f)} = \frac{2E_f h_s}{3(1+\nu_f)} n(n-1)\frac{w_0}{R^2}\left(\frac{r}{R}\right)^{n-2} \sin n\theta\ . \tag{1.37}$$

These stresses are pictured in Fig. 1-5.

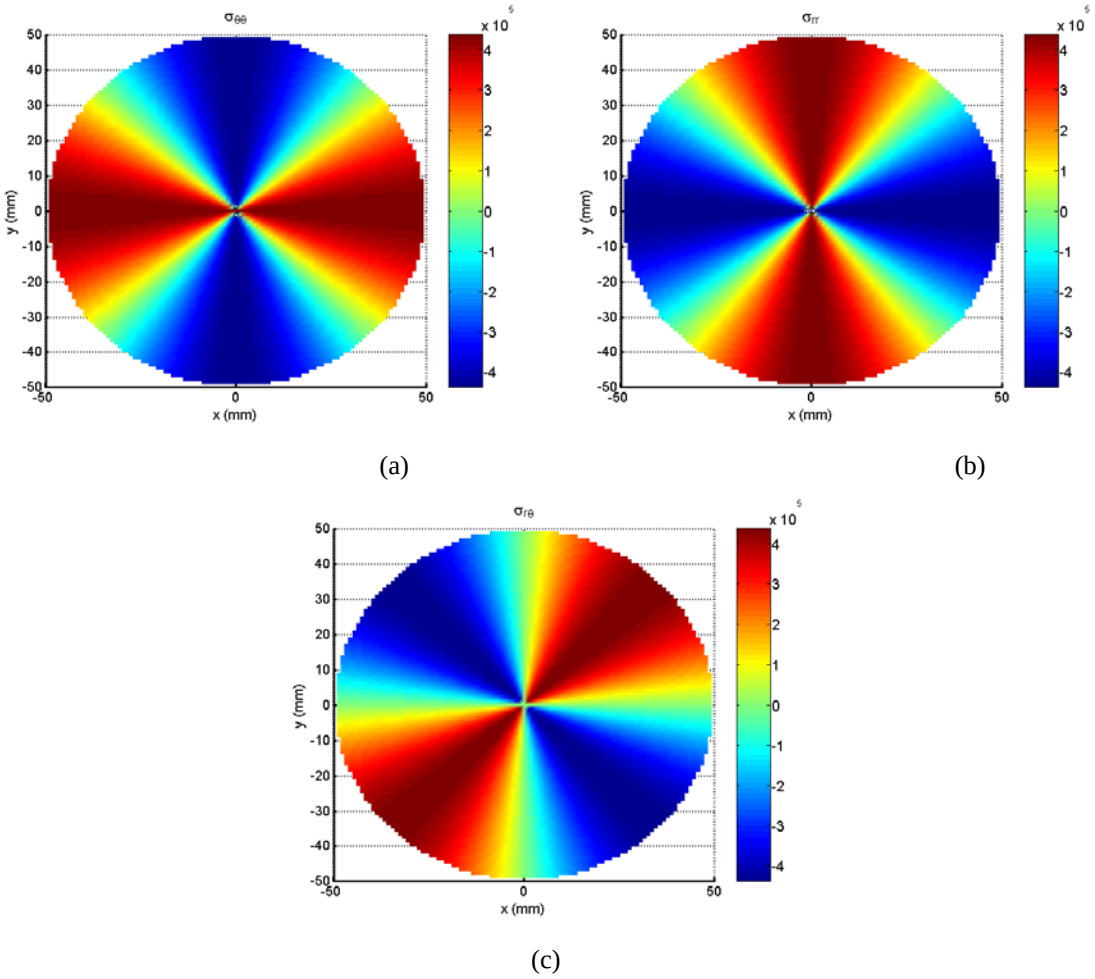

Figure 1-5. Radial, circumferential and twist curvature from Eqs. 1.36 and 1.37.

This simple example demonstrates that for a strongly non-uniform deformation (due to, e.g., a non-uniform misfit strain), the difference between the film stress predicted by Stoney and by the non-uniform HR relation can be significant.

Next, the validity of the axisymmetric HR relations, as compared to Stoney, will be established by comparing experimental results to the stresses predicted by each analysis. Then both the axisymmetric and the full HR relations will be used to infer film stress in various thin film-wafer substrate systems.

2. Measuring Stress: X-ray Microdiffraction (μXRD)

In order to determine the relative validity of the "nonlocal" stress/curvature relations compared to the "local" Stoney formula, it is necessary to employ a technique which is able to independently measure both the film stress and the substrate curvature at the same place on a wafer. The curvature can be used to calculate film stress using both types of relations (local and nonlocal), and the resulting stresses can be compared. The stresses from curvature can also be compared with the stresses determined from the direct measurement. The various implementations of X-ray microdiffraction (μXRD) provide such an opportunity. In general, X-ray diffraction (XRD) measures the crystalline lattice spacing in a material and uses the spacing change as a strain gage. Following the strain measurement, a constitutive law is used to infer stress in the film. In this particular project, synchrotron X-ray microdiffraction was used for these measurements. Synchrotron μXRD has several advantages over traditional lab X-rays. These advantages include higher flux, smaller spot size, and the ability to quickly change between a monochromatic and polychromatic beam. In our experiment, the monochromatic beam is used to measure film stress, and the white (polychromatic) beam to measure substrate curvature. Since the two types of measurements are using different wavelengths, they are effectively independent of each other. These μXRD experiments were performed at Beamline 7.3.3 at the Advanced Light Source at Lawrence Berkeley National Lab in Berkeley, CA.

X-ray Diffraction: An Overview

In its most basic form, X-ray diffraction consists of an X-ray beam that is shined onto a specimen and then bounces off, diffracted by the specimen's crystalline lattice (Fig. 2-1). The resulting diffraction pattern, known as a Laue pattern, is captured with a detector. Within this basic framework the specifics of specimen, beam characteristics, and detector size can vary widely. The diffraction process is governed by the well-known Bragg's Law, $d = \lambda / 2\sin\theta$, which relates the incoming wavelength to the lattice spacing and diffraction angle. In this equation, λ is the beam wavelength, d the lattice spacing, and θ the angle between the beam and the plane of interest.

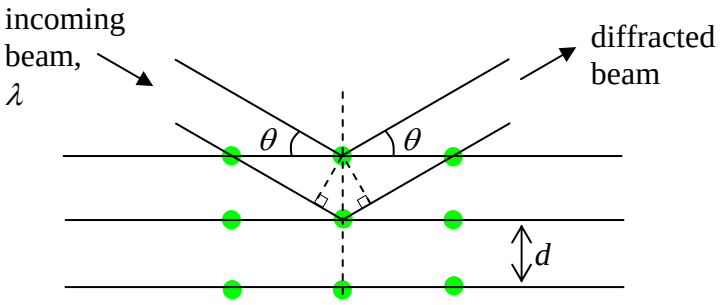

Figure 2-1. X-ray diffraction schematic

The diffracted beam forms Laue patterns, which are captured easily when using an area detector. Polychromatic diffraction patterns are composed of spots of high intensity (Fig. 2-2a), while monochromatic diffraction patterns, known as Debye rings, consist of high-intensity rings (Fig. 2-2b).

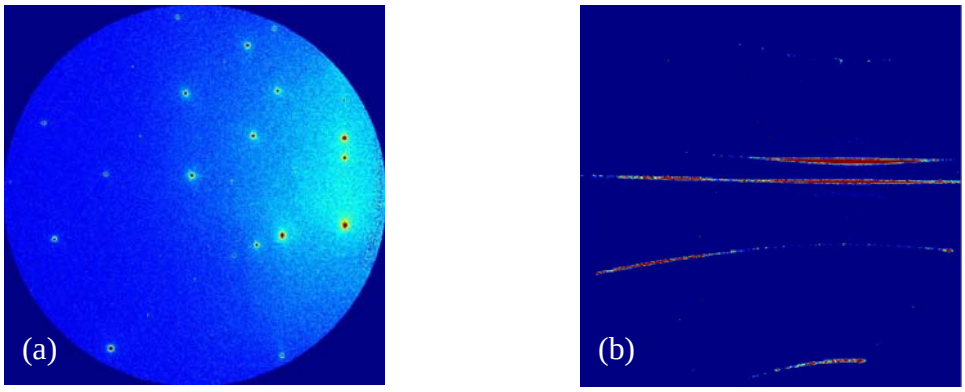

Figure 2-2. Diffraction patterns from (a) white and (b) monochromatic incoming beams.

In a typical experiment, the specimen is held at a known angle to the incoming beam so that the area detector is able to capture as much of the diffracted beam as possible (Fig. 2-3). The resulting patterns are analyzed to obtain the desired measurement at that location on the specimen. The specimen is translated across the beam in *x* and *y* so that a map is obtained, with images (or datapoints) taken at some specified spacing in *x* and *y*. For example, a line scan might have 10 datapoints spaced 0.1mm apart in *x*, while an area scan might have 5 of these *x*-lines spaced 0.5mm apart in *y*. In this case the total area covered in the line scan is 1mm, and in the area scan is 2.5mm^2. There are 50 images captured, so after analysis there will be 50 measurements across the sample surface (note: these are arbitrary numbers for illustrative purposes only.)

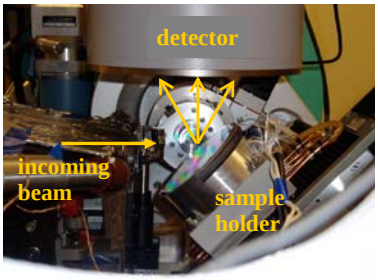

Figure 2-3. The microdiffraction setup at the Advanced Light Source. The incoming X-ray beam is reflected from the sample surface and captured by the detector.

This is a pointwise measurement, which scans over the area of interest but does not get information from the entire surface. Also, it is important to note that the monochromatic and white beam measurements, though performed using the same experimental setup, use different portions of the incoming X-ray beam and are effectively independent measurements.

Monochromatic μXRD

Monochromatic XRD uses a beam that is a single wavelength and diffracts into patterns called Debye rings. Each ring on the pattern is made up of many spots, and corresponds to a single lattice plane. Each spot corresponds to a single grain, but not every grain illuminated in the beam contributes to the diffraction pattern. Only the subset of grains that are oriented properly, namely whose specific lattice planes are at an angle to the incoming beam which corresponds to Bragg's law, will interact with the beam in such a way that it diffracts off of the crystal and impacts the area detector to create a spot. Therefore, in order to obtain well-populated rings, this technique works best when the grain size is much smaller than the beam spot size so that a large number of grains are illuminated at each point.

The average equibiaxial stress in the specimen (e.g., a thin film on some substrate) can be determined from the diffraction pattern using what is known as the "d vs $\sin^2\psi$" method [18]. The coordinate system of the images is made up of 2θ, χ, and ψ, where 2θ is across the rings, χ is horizontally across the image, and ψ is aligned along the rings (Fig. 2-4).

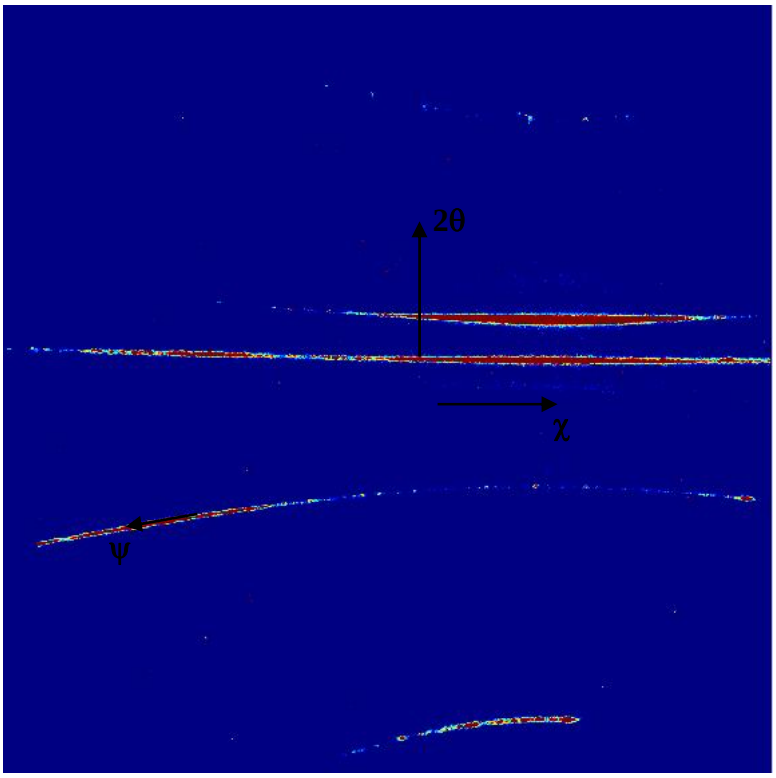

Figure 2-4. Monochromatic pattern with coordinate system

The relevant equation for the d vs $\sin^2\psi$ analysis as shown here is for equibiaxial stress (i.e., $\sigma_{xx} = \sigma_{yy} = \sigma$, $\sigma_{xy} = 0$).

$$\frac{d - d_0}{d_0} = \frac{1+\nu}{E}\sigma \sin^2\psi - \frac{2\nu}{E}\sigma \tag{2.1}$$

This stress is related to the lattice strain $(d - d_0)/d_0$ via the isotropic version of Hooke's law. Constitutive isotropy is indeed a very good assumption for certain polycrystalline films. For example, W, which is used in the present study, was chosen for its isotropic properties. Linear elasticity is also a good assumption for a material such as W, since its yield stress is very high compared to most commonly used metallic thin film materials.

To find the stress, a plot of d vs. $\sin^2\psi$ is obtained (thus the technique's name). The lattice spacing, d, can be obtained from 2θ via Bragg's Law. To find 2θ, the rings are

divided into small compartments of 2θ vs. ψ in a process known as binning. In each bin, *i*, the intensity is integrated and fit to a Lorentzian function to find 2θ at maximum intensity, or $2\theta^i$. Also, the average ψ for a bin, ψ^i, is found as $\psi^i = (\psi_{\max} + \psi_{\min})/2$.

Assuming the material constants are known, the other variable in this equation that must be determined in order to complete the analysis is d_0, or the unstressed lattice spacing. In practice, it is almost impossible to obtain this value, and the value at $\psi = 0$ is substituted. This is allowable because elastic strains introduce, at most, a 0.1% difference between the true d_0 and the d at any ψ. Since d_0 is a multiplier to the slope, the total error introduced by this assumption is less than 0.1% and is negligible compared to error from other sources [18].

To determine d_0, ψ^i vs. $2\theta^i$ is plotted and fit to a function (Fig. 2-5). Then 2θ is found at $\psi = 0$, and d_0 is calculated using Bragg's Law.

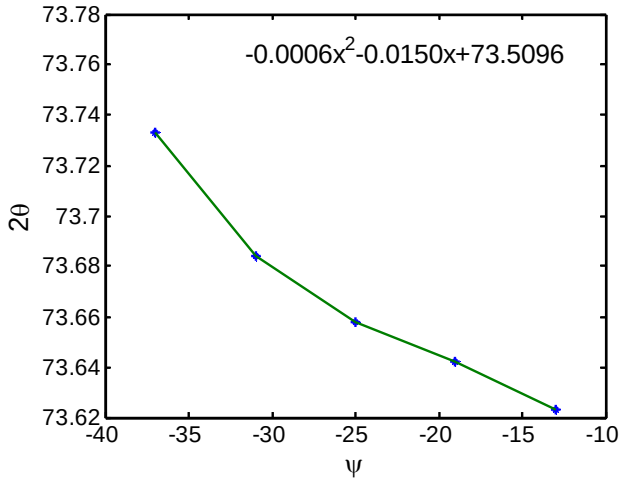

Figure 2-5. plot of ψ vs. 2θ

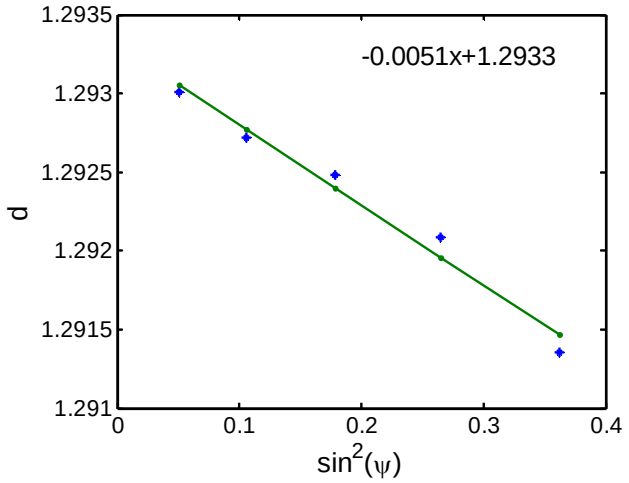

Figure 2-6. plot of d vs $\sin^2\psi$

Finally the plot of d vs. $\sin^2\psi$ is obtained (Fig. 2-6). For a truly equibiaxial stress state, the plot should be linear. A linear trend line is fit to the data, and by comparing the equation of that line with Eq. 2.1, the stress is easily found as

$$\sigma = \frac{Es}{(1+\nu)d_0}, \tag{2.2}$$

where s is the slope of the linear fit.

If the stress is not strictly equibiaxial, then this process determines the mean stress, or $\sigma = (\sigma_{xx} + \sigma_{yy})/2$. For a complete analysis, this procedure is performed for each ring in each image in a scan. Each ring corresponds to a given lattice plane in the specimen, and so the analysis for one ring determines the stress in that direction. For an isotropic system, such as W, the stress from a single ring is sufficient.

Polychromatic (White Beam) μXRD

A polychromatic, or white, beam incorporates a range of wavelengths into the incoming light. In this case, the Laue patterns consist of many high-intensity spots (Fig. 2-7a). Each spot corresponds to a given lattice plane in a given grain. For a single grain of a known material, a known pattern of spots will be diffracted. If the grain is strained, the pattern shifts in a predictable manner. When there are several grains illuminated, the pattern for each grain is superimposed on the image. A sophisticated software program deconvolutes these images and indexes them, identifying individual patterns from each grain [19]. The software calculates the orientation matrix for each grain, as well as the deviatoric strain tensor in that grain. (The deviatoric stress is then found using Hooke's law [18].) This technique is used when very few grains are in the illuminated region, since if there are too many superimposed patterns it becomes impossible for even the software to match the individual spots with the specific grain that produced them.

In the case of a single crystal specimen, the orientation matrix that is measured is always from the same grain. Once the crystal orientation is obtained at each location across the specimen, the relative slope and curvature are then determined by tracking the

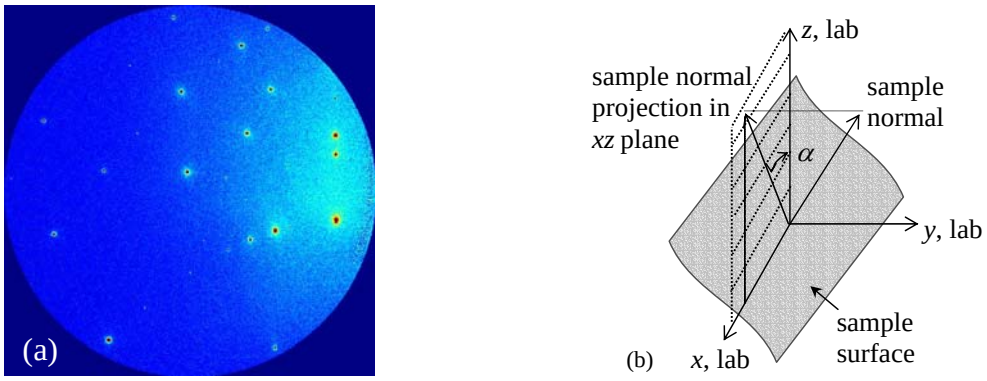

Figure 2-7. (a) Laue pattern from the single crystal Si wafer. (b) Definition of coordinate system and the projection angle α; slope in xz plane = tan(α).

changes in the vector defining the grain normal with respect to the lab coordinate system. For a scan along the *x* axis (sample diameter), we are only concerned with the slope changes in the *xz* plane. This slope is equal to tan(α), where α is defined as the angle between the projection of the grain normal in the *xz* plane and the *z* axis in the lab reference frame (Fig. 2-7b).

For a radially symmetric sample on which the scan is performed along the diameter, where $y = 0$, cylindrical coordinates can be used. The radial slope, $\partial f/\partial r = \tan(\alpha)$, and the circumferential curvatures κ_{rr} and $\kappa_{\theta\theta}$ are then determined from

$$\kappa_{rr} \equiv \frac{\partial^2 f}{\partial r^2} = \frac{\partial(\tan\alpha)}{\partial r}, \tag{2.3}$$

$$\kappa_{\theta\theta} \equiv \frac{1}{r}\frac{\partial f}{\partial r} = \frac{1}{r}(\tan\alpha). \tag{2.4}$$

3. Verifying Nonlocal Formulas: Comparison with XRD

In order to begin to verify the new analytical relations which allow for the inference of film stress from nonlocal curvature measurements (nonlocal relations), the two different types of μXRD measurements described in Chapter 2 were used to measure both substrate slope and film stress across the diameter of an axisymmetric thin film-substrate specimen composed of a circular W film island deposited in the center of a single-crystal Si substrate [20]. The substrate slopes, measured by polychromatic (white beam) μXRD, were used to calculate curvature fields and to thus infer the film stress distribution using both the "local" Stoney formula and the new, "nonlocal" HR relations. The variable film thickness, which was independently measured, was also an input to the HR relations. These stresses were then compared with the film stress calculated from lattice distortions measured independently through monochromatic μXRD, to determine the validity of the new formula and to quantify the improvement over the commonly accepted Stoney analysis.

Methodology

The specimen consisted of a circular, 24.8 mm diameter W film island deposited on the center of a 100 mm diameter, 525 μm thick Si <001> wafer (Fig. 3-1). The film thickness is variable across the island; the thickest portion, in the center of the island, is approximately 1.85 μm. The Young's modulus for Si and W are 130 GPa and 410 GPa, respectively, while the Poisson's ratio is 0.28 for both materials [21].

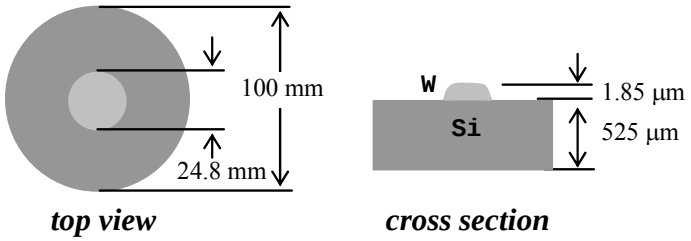

Figure 3-1. specimen schematic

Measurements were taken along the specimen diameter, $x = 0$. The spacing between data points was 0.25 mm for monochromatic beam measurements and 0.1mm for white beam measurements. Both types of μXRD were used in order to obtain information about both system orientation (for slope and curvature) and film strain (for stress).

The axisymmetric form of the nonlocal relations (Eq. 1.31) require full-field curvature information, in the form of the average of the first curvature invariant, $\kappa_{rr} + \kappa_{\theta\theta}$, of the curvature tensor across the entire specimen, in order to determine film stress. However, μXRD is a pointwise measurement, and as such it does not yield a full map. Since a circular film is deposited in the center of a circular SI substrate of the 001 type, the specimen topography (deformation due to misfit strain induced film stress) is expected to be radially symmetric provided that the film thickness profile and the misfit strain are also axisymmetric. If this is the case, then a measurement obtained along the specimen diameter can be used to produce a full-field map of the surface topography and curvature. An optical slope measurement technique called Coherent Gradient Sensing (CGS), which will be discussed in more detail later, was used to check the symmetry of the system. The Cartesian slopes obtained by CGS are integrated to provide the deformed specimen topography (Fig. 3-2) and to demonstrate that the specimen is, in fact, radially symmetric. Therefore, the measurements obtained from μXRD along a

wafer diameter are enough to generate both radial and circumferential curvature maps. Fig. 3-2b is a cross section of the topography map through the sytem center. It reveals a shape which features a "strong" negative radial curvature at the location covered by the film and "weaker" positive curvatures at the uncovered parts.

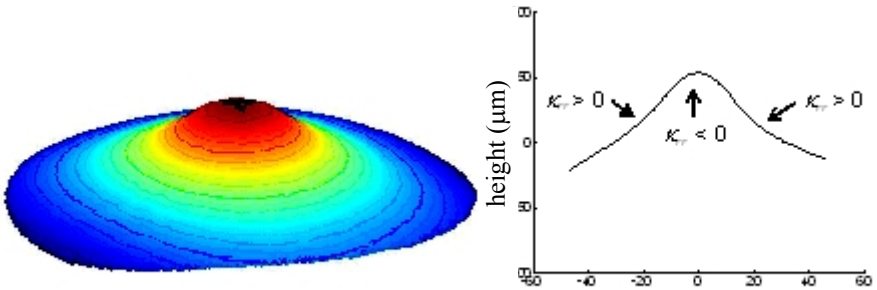

(a) (b)

Figure 3-2. (a) CGS topography (b) topography at $x = 0$

After the substrate slope and film stress were measured with μXRD, the specimen was broken into pieces so that the film thickness could be measured using a scanning electron microscope (SEM). Several images were taken along the film radius. Since the specimen topography is axisymmetric, the thickness across the island diameter was extrapolated from these measurements. In each image, the film thickness was determined by comparing the length of a line drawn through the thickness to the length of the scale bar (Fig. 3-3). Each image covers approximately 8 μm, and five thickness measurements within each image were averaged to obtain the film thickness at that image location. The film thickness variation with radial position is shown in Fig. 3-3b. Near the island edge, the thickness drops off precipitously from an approximate level of 1.85 μm in the center to approximately 0.8 μm at the edge of the island. From Eq. 1.31, this is expected to correspond with a rapid increase in film stress in that location.

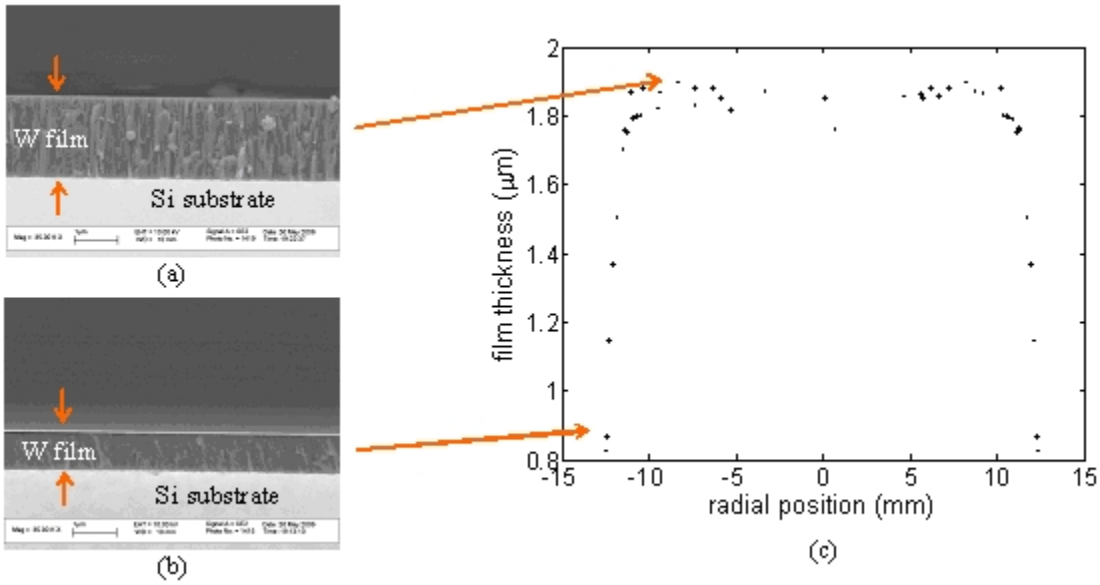

Figure 3-3. SEM images of film cross-section (a) within the central approximately constant thickness region and (b) near the film edge; (c) radial film thickness measured from the SEM images

White Beam μXRD System Slope and Curvature Measurements

The radial slope, $\partial f / \partial r$, across the wafer diameter is shown in Fig. 3-4a. In the central part of the film-covered region of the wafer the slope appears to be approximately linear, but it substantially deviates from linearity as the film edges are approached from within. At the film edges, the radial gradient of the slope (radial curvature κ_{rr}) suffers a large but finite jump and changes sign from negative to positive, consistent with the topography map of Fig. 3-2 obtained by integration of the CGS slopes. As the wafer edges are approached, the radial curvature decreases gradually to a small but finite value. The overall shape of the radial slope is antisymmetric about the wafer origin, as would be expected from the axisymmetry of the topography. To conclusively demonstrate this, the data from one side were reflected about the origin and overlayed on the data of the other side. This exercise, shown here in Fig. 3-4b, demonstrates that the reflected slopes from either side agree to within 5%.

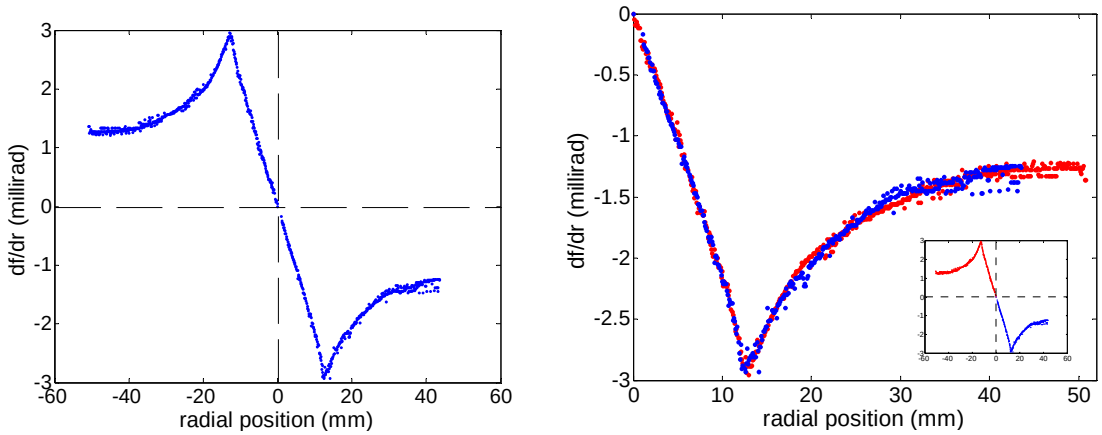

(a) (b)

Figure 3-4. (a) Slope along the sample diameter. (b) Slope from the center, overlapped, to show antisymmetry.

Since the specimen geometry, shape measured by CGS, and slope measured by XRD all suggest radial symmetry, the linear slope measurement from μXRD is used to construct full-field slope data. Indeed, the slope can now be replaced by two piecewise fits of two polynomials, one taken within the film portion and the other outside it. Figure 3-5 shows the high quality of the polynomial fits of the raw μXRD slope data. It should be noted that the two polynomial fits are required to pass through the same point corresponding to the estimated location of the film edge.

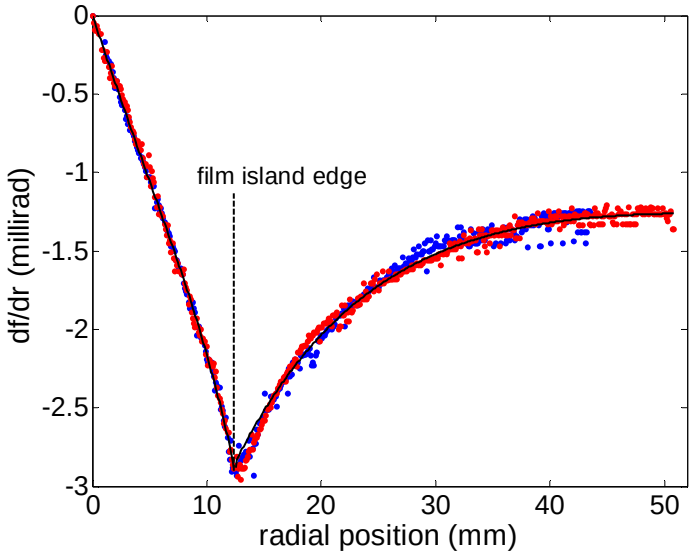

Figure 3-5. Polynomial fit of the XRD data

Figure 3-6 shows the radial and circumferential curvature distributions obtained when the polynomial fit of the slope, shown in Fig. 3-5, was used to determine the two independent wafer curvature components through Eqs. 2.3 and 2.4. The circumferential curvature, $\kappa_{\theta\theta}$, is continuous across the film boundary, but the radial curvature, κ_{rr}, suffers a finite jump at the island edges. This is consistent with the observation of Brown et al. [20]. What is perhaps more interesting is that even within the area of film coverage, both curvature components vary with radial position.

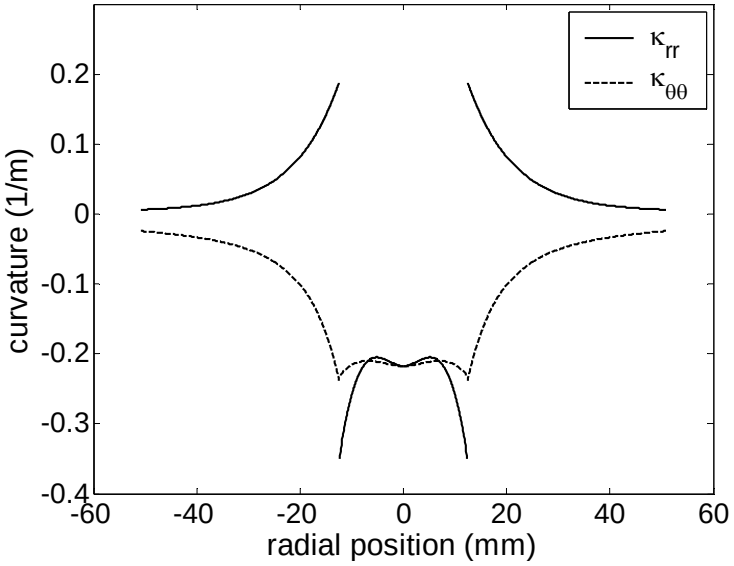

Figure 3-6. Curvatures (κ_{rr} and $\kappa_{\theta\theta}$) obtained from the polynomial fit of white beam μXRD slope data

By further invoking axisymmetry, we may also use the film thickness measurement conducted along the island radius to construct the island thickness profile in the absence of full-field thickness measurements. The film thickness is considered as an axisymmetric function of the radial coordinate, r, and can be fitted by the following radial distribution:

$$h_f = h_f(r) = 1.85 + 0.00713\left(1 + \frac{1.49}{r - 12.6}\right)(r - 5.82)^2 H(r - 5.82);\ r \le R_f = 12.4\,mm, \quad (3.1)$$

where the radius r is in millimeters, the film thickness h_f is in micrometers, and H is the Heavyside step function. Figure 3-7 compares the polynomial fit of Eq. 3.1 with the actual SEM thickness data and demonstrates their good agreement.

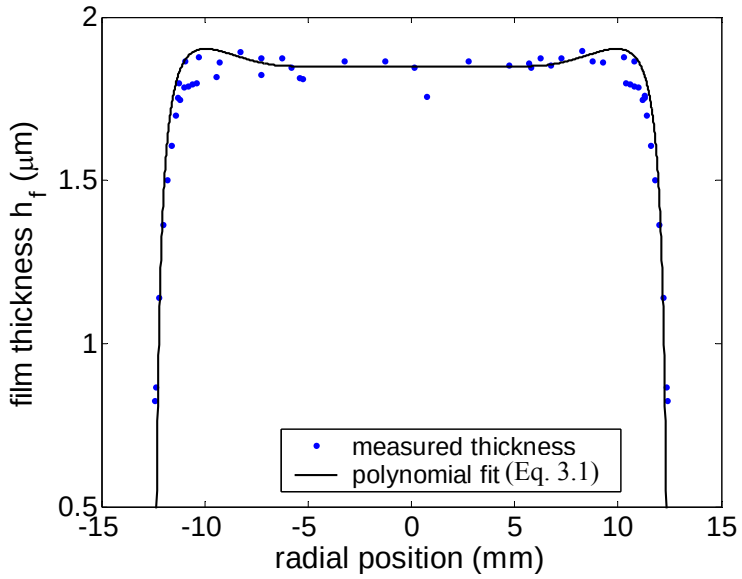

Figure 3-7. Thickness data compared with fit.

Monochromatic Beam μXRD Film Stress Measurements

The absolute magnitude of the mean stress, $-(\sigma_{rr}+\sigma_{\theta\theta})/2$, obtained through the monochromatic μXRD measurement of misfit strain is shown in Fig. 3-8.[1]

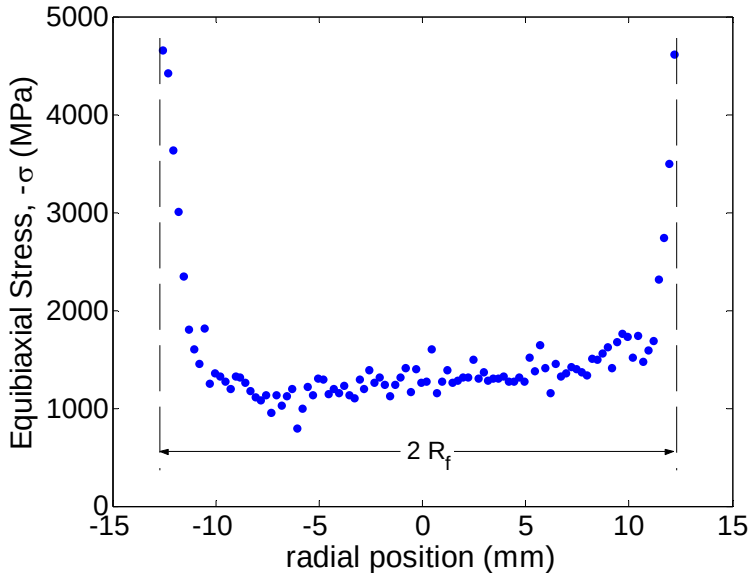

Figure 3-8. Average equibiaxial film stress from monochromatic X-ray measurement.

[1] Although the mean stress itself is compressive, its absolute magnitude is displayed here for reasons of clarity of discussion.

The stress varies slowly throughout most of the island diameter. However, near the island edge the stress increases very steeply to over five times its central value within a small (~2 mm) boundary layer from the film edge. This is due to the existence of a strong thickness gradient near this edge (Fig. 3-3c). It is also due to the eventual existence of a traction-free boundary at the end of the film. These two geometrical effects, which result in a substantial stress concentration gradient (huge compressive stresses developing from 1 to 5 GPa over a few millimeters of length), provide a substantial prediction challenge to any theoretical model used for the inference of stress through substrate curvature measurements. In the following sections, we will concentrate on the ability of various techniques to independently predict this directly measured stress amplification.

Comparison with Various Analyses of Film Stress Inference

In this section the results of the mean film stress distribution obtained through the monochromatic μXRD measurement are compared with the stress distributions predicted via the use of three different analytical stress/curvature relations, one local (Stoney) and two nonlocal (HR). The common input to these relations is the substrate curvatures (Fig. 3-6) obtained through the independent white beam μXRD substrate slope measurement.

Figure 3-9 illustrates this comparison. The discrete points are the stress distribution results of the direct monochromatic beam μXRD measurement. The dotted line shows the prediction of the Stoney equation (Eq. 1.1) with $\kappa(r) = [\kappa_{rr}(r) + \kappa_{\theta\theta}(r)]/2$ and $\sigma(r) = [\sigma_{rr}(r) + \sigma_{\theta\theta}(r)]/2$ being the mean stress and curvature, respectively. The Stoney relation assumes that the radius of the film, R_f, and

that of the substrate, R_s, are equal and that the film thickness is uniform. Although the Stoney equation was derived strictly for constant κ and σ, it is used here in a "local" sense in which $\kappa(r)$ as measured (Fig. 3-6) is input into Eq. 1.1 to obtain the dotted stress distribution shown. The Stoney prediction underestimates the discrete stress data by as much as 50% in the central portion of the film and completely misses the dramatic 500% stress increase at the edges.

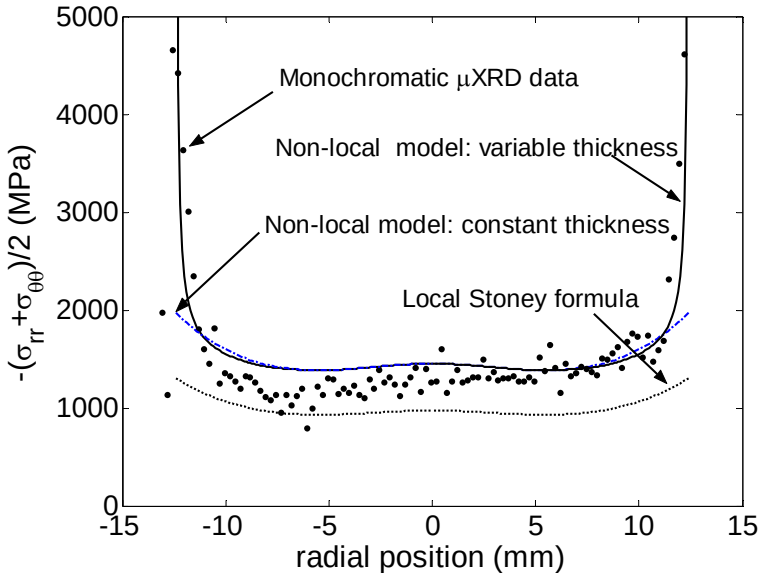

Figure 3-9. Monochromatic μXRD stress data compared with calculated stress.

The dashed line shows a prediction of a nonlocal model in which the island film radius is different from the substrate radius ($R_s > R_f$) but the film thickness inside the island is assumed to be constant. The stresses are obtained by using Eq. 1.31, specialized to the case of constant film thickness h_f = 1.85 μm for $r \le R_f$ and zero thickness for $r > R_f$ (h_f is taken to be the approximate film thickness measured at the island center). This is still a nonlocal calculation since it also involves averaging the curvature field over the entire wafer (both covered and uncovered parts) to obtain $\overline{\kappa_{rr} + \kappa_{\theta\theta}}$. However, it does not take into account the drastic reduction of the film thickness over a distance of a

few millimeters from the edge (see Fig. 3-3c). As is obvious from Fig. 3-9, this prediction approaches the discrete monochromatic μXRD measurement much better than the result based on Stoney, but still completely misses the severe stress concentration near the film edges.

Finally, the solid line represents the result of utilizing Eq. 1.31 in its most general form, in which thickness and curvatures are both allowed to vary with radial position *r*. The radial profile of the island film thickness $h_f(r)$ from Eq. 3.1 was used as input in this calculation. It is evident from Fig. 3-9 that this last calculation, utilizing the most general axisymmetric nonlocal relation, agrees very well with the monochromatic μXRD stress measurement over the entire film diameter, including the region close to the film edge. In particular, the success of the generalized nonlocal stress/curvature relation in capturing the dramatic compressive stress increase that has been independently measured provides validation to the generalized nonlocal analysis.

An important by-product of this analysis is its ability to also estimate interfacial shear stresses acting between the film and the substrate. These shear stresses are a direct consequence of in-plane nonuniformities. For our radially symmetric experiment, the only surviving shear stress, τ_r, is given by Eq. 1.32 and can readily be evaluated by differentiating $\kappa_{rr}(r)+\kappa_{\theta\theta}(r)$ of Fig. 3-6. This interfacial shear stress, shown here in Fig. 3-10, is not nearly as large as the direct film stress, but it climbs to approximately 400 MPa near the film edges. The combined presence of huge direct film stresses ($\sigma \sim$ -5 GPa) at the film edge and substantial interfacial shears may be enough to trigger interfacial delamination [3]. In fact, careful scrutiny of the film/substrate adhesion through SEM has revealed a well-defined, circular delamination front surrounding the

island at r = 12.4 mm, very close to its edge. A local, SEM, view of this delamination is shown in Fig. 3-11.

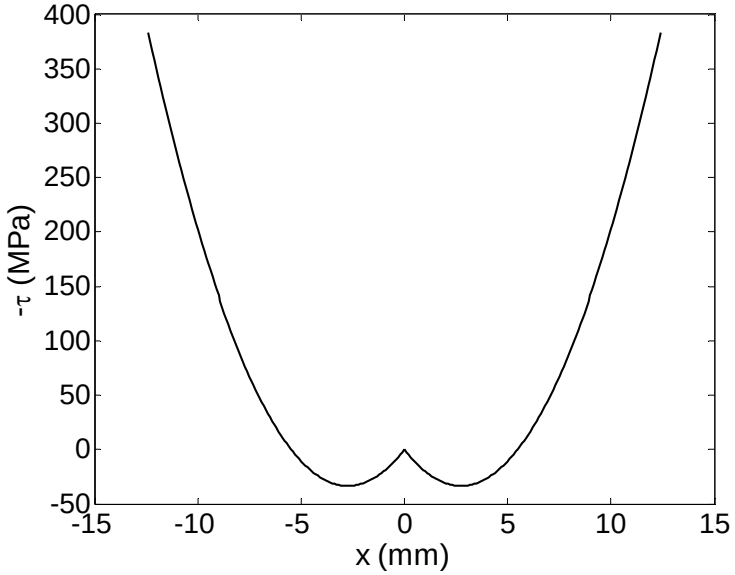

Figure 3-10. Interfacial shear stress.

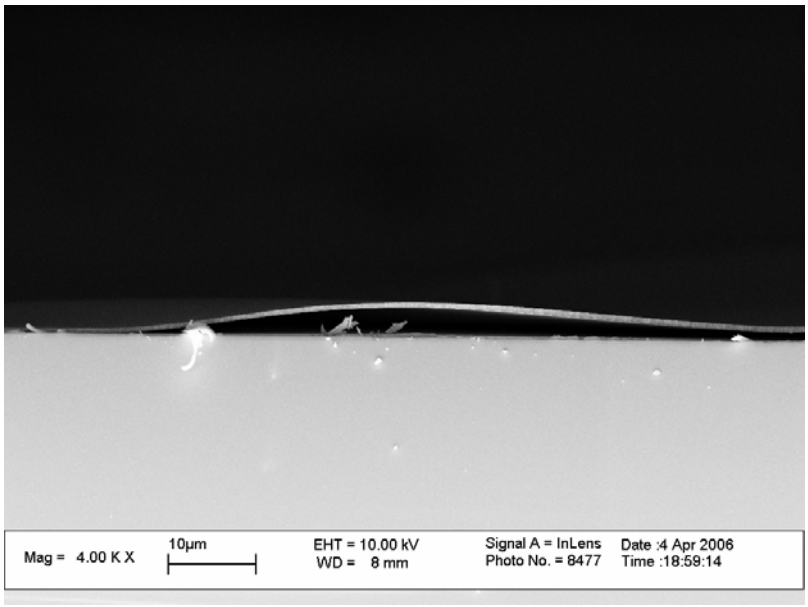

Figure 3-11. SEM image showing delamination at film edge.

The maximum in-plane shear stress $(\sigma_{rr}^{f} - \sigma_{\theta\theta}^{f})/2$ can also be calculated from Eq. 1.31 and from the curvature distributions (Fig. 3-6) obtained through the white beam μXRD measurement. The in-plane shear stress distribution across the island is shown in

Fig. 3-12. The maximum absolute value of this stress is less than 7 MPa or 0.2% of the in-plane mean stress, which suggests that the film stress state of this specimen is, to all practical purposes, equibiaxial. This fact justifies the assumptions of equibiaxiality used in the analysis of the monochromatic μXRD measurement.

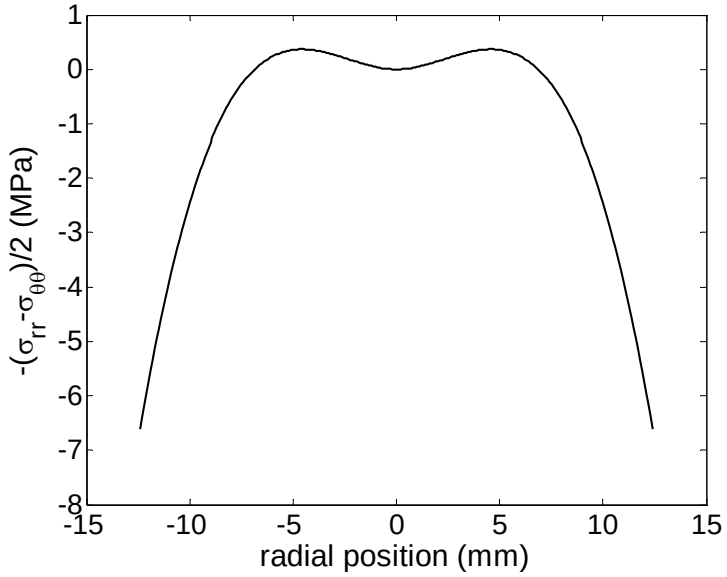

Figure 3-12. In-plane shear stress

An Aside: Necessity of Full-Field Measurement

Thus far, it has been shown that the nonlocal stress/curvature relations introduced in chapter 1 do a better job of predicting stress in a thin film than the classical "local" Stoney formula does in the presence of strong nonuniformities in film thickness and system curvature. However, these nonlocal relations require a full-field measurement of all curvature components. Consequently, a natural next step is to introduce a measurement technique which provides a means of determining the stress tensor across the entire system (in full field). The method of choice in the present thesis is Coherent Gradient Sensing interferometry, otherwise known as CGS.

4. Coherent Gradient Sensing (CGS)

The coherent gradient sensing (CGS) method is a self-referencing interferometric technique that produces fringe patterns of surface slope by laterally shearing an initially planar wave front which has been reflected from a specimen (e.g., wafer). Figure 4-1 shows a schematic of the CGS setup in reflection [13, 14, 22]. A coherent, collimated laser beam (300 mm or less in diameter) is directed to a specularly reflecting wafer surface via a beam splitter. In general, the wafer is nonplanar and its surface shape, or distortion relative to a flat surface, can be described by the equation $z = f(x, y)$. In this relation, z provides the wafer surface height for each in-plane wafer position defined by x and y. The beam reflected from the wafer is distorted by the nonplanar shape of the wafer. After reflection, the resulting distorted wave form is described by a two-dimensional surface in space whose equation is given by $z = S(x, y)$, where $S(x, y) \approx 2f(x, y)$. This distorted wave front is again passed through the beam splitter and is then incident upon a pair of identical high-density gratings, G_1 and G_2, separated by a distance Δ. The gratings act to optically "shear" or "differentiate" the incident wave front to produce a series of diffracted beams. These beams are separated using a filtering lens to form distinct diffraction spots on a filter plane. An aperture placed in this plane serves to isolate the diffraction order of interest, which is then imaged onto the photographic film plane. For present purposes, either of the ± 1 diffraction orders is of interest, as will be clear in the following discussion.

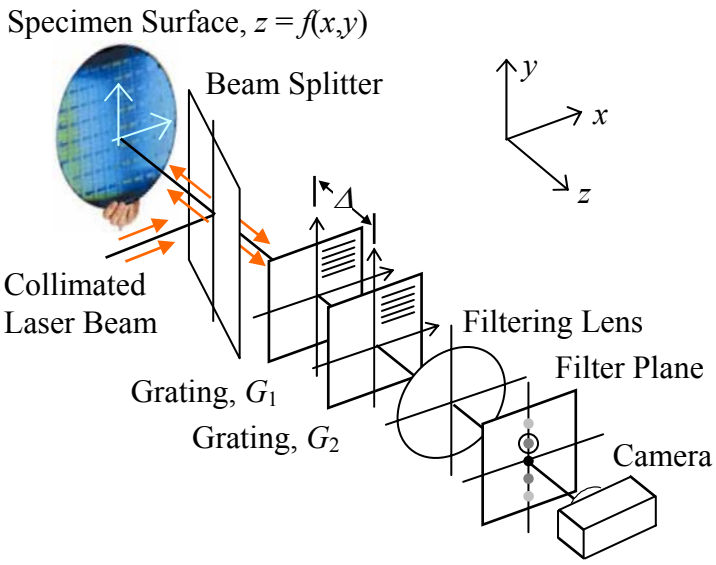

Figure 4-1. CGS schematic

Figure 4-2 is a two-dimensional schematic illustrating the principles of the CGS method. The figure shows the distorted optical wave front, $S(x, y)$, incident on the two gratings in which the lines are taken to be oriented along x. At the first grating, G_1, the incident wave front is diffracted into several wave fronts, E_0, E_1, E_{-1}, E_2, E_{-2}, etc., of which only the first three are drawn in Fig. 4-2. Each of these wave fronts, in turn, is diffracted by the second grating, G_2, to generate additional wave fronts, such as $E_{0,0}$, $E_{0,1}$, and $E_{0,-1}$. The diffracted beams are combined by a filtering lens to produce diffraction spots, such as D_0, D_{+1}, and D_{-1}, in the focal plane of lens (filter plane). One of the diffraction spots, typically the first diffraction order, the D_{+1} spot, is chosen with an aperture for imaging onto the film plane.

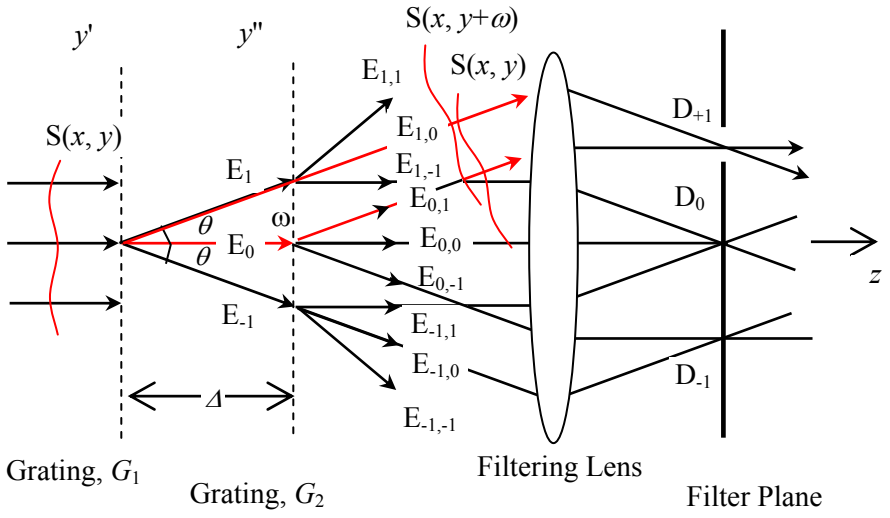

Figure 4-2. CGS schematic describing the optical differentiation

The presence of the two gratings in the path of the optical wave front generates a lateral shift (or shearing) of the wave front. For example, the diffracted beam $E_{1,0}$, whose wave front is denoted as $S(x, y+\omega)$, is shifted from the beam $E_{0,1}$, whose wave front is denoted as $S(x, y)$, by a distance ω in the y direction. The shift distance, ω, is expressed as $\Delta tan\theta$, where $\theta = arcsin(\lambda/p)$ is the diffraction angle and λ and p are the wavelength of light and the pitch of the gratings, respectively. For small angles of diffraction, $\omega \approx \Delta\theta \approx \Delta(\lambda/p)$. The condition for constructive interference of the original and shifted wave fronts is given by

$$S(x, y+\omega) - S(x, y) = n^{(2)}\lambda, \qquad n^{(2)} = 0, \pm 1, \pm 2\ldots \quad (4.1)$$

where $n^{(2)}$ is an integer that represents fringes associated with shearing along the y direction. By dividing Eq. 4.1 by ω, taking ω to be sufficiently small, and substituting $\omega = \Delta(\lambda/p)$, it is seen that

$$\frac{\partial S(x, y)}{\partial y} = \frac{n^{(2)}\lambda}{\omega} = \frac{n^{(2)}p}{\Delta}, \qquad n^{(2)} = 0, \pm 1, \pm 2\ldots \quad (4.2)$$

Recalling that $S = 2f$ and repeating the above analysis for gratings aligned along the y-direction, it can be shown that the alternating dark and bright interference fringes correspond to constant values of components of the in-plane gradient of the wafer surface topography as follows:

$$\frac{\partial f(x,y)}{\partial x_\alpha} = \frac{n^{(\alpha)} p}{2\Delta}, \qquad n^{(\alpha)} = 0,\pm 1,\pm 2\ldots \quad (4.3)$$

where $\alpha, \beta \in \{x,y\}$. A relative rotation of the gratings to the wafer allows for both orthogonal components of slope to be recorded in the form of full-field slope maps. The three independent components of curvature tensor field, $\kappa_{\alpha\beta}$, can now be determined directly from two orthogonal CGS slope maps by partial differentiation along the x- and y- directions as

$$\kappa_{\alpha\beta}(x,y) \approx \frac{\partial^2 f(x,y)}{\partial x_\alpha\, \partial x_\beta} \approx \frac{p}{2\Delta}\left\{\frac{\partial n^{(\alpha)}(x,y)}{\partial x_\beta}\right\}. \quad (4.4)$$

In order to determine the full curvature tensor, the gradient fields in two orthogonal directions must be recorded. Equation 4.4, which applies to the shear (or twist) curvature component, $\kappa_{xy} = \kappa_{yx} = \partial^2 f/\partial x \partial y = \partial f^2/\partial y \partial x$, as well as the direct (or normal) Cartesian curvature components, $\kappa_{xx} = \partial^2 f/\partial x^2$ and $\kappa_{yy} = \partial^2 f/\partial y^2$, is the equation governing the curvature tensor field at any in-plane location (x, y). It enables the global, full-field measurement of the curvature tensor for the film-substrate system.

It can also be useful to obtain the principal curvature maps, i.e., the maximum and minimum values of curvature. In order to derive the principal curvatures, first the effect of an in-plane rotation on the two independent slope and the three independent curvature

components is derived, i.e., the transformation equations from the original coordinate system to one that is rotated by some arbitrary angle, β. Once these have been established, the two mutually orthogonal directions of the principal curvatures can be found by setting the transformed curvature derivative, with respect to the angle of rotation, to zero. These two angles, defining the principal directions, are then plugged into the curvature transformation equations to obtain the principal curvatures.

Consider axes x', y' which are rotated by an angle, β, from the original axes x, y. The coordinates of some point, P, with respect to the two sets of axes are then

$$\begin{aligned} x &= x'\cos\beta - y'\sin\beta, \\ y &= x'\sin\beta + y'\cos\beta, \end{aligned} \tag{4.5}$$

and the equation of the surface (e.g., wafer) with respect to the two coordinate systems is $z = f(x,y) = g(x',y')$. The two independent slope components are related to each other as

$$\begin{aligned} \frac{\partial g}{\partial x'} &= \frac{\partial f}{\partial x}\frac{\partial x}{\partial x'} + \frac{\partial f}{\partial y}\frac{\partial y}{\partial x'} = \frac{\partial f}{\partial x}\cos\beta + \frac{\partial f}{\partial y}\sin\beta, \\ \frac{\partial g}{\partial y'} &= \frac{\partial f}{\partial x}\frac{\partial x}{\partial y'} + \frac{\partial f}{\partial y}\frac{\partial y}{y'} = -\frac{\partial f}{\partial x}\sin\beta + \frac{\partial f}{\partial y}\cos\beta. \end{aligned} \tag{4.6}$$

The curvature components are found from differentiating the slope components according to the first part of Eq. 4.4 and using the identities $\cos 2\theta = 1\text{-}\sin 2\theta$ and $\sin 2\theta = 2\sin\theta\cos\theta$. The curvature components, κ_{xx}', κ_{yy}', and κ_{xy}', in the rotated coordinate system are then given by:

$$\begin{aligned}
\kappa_{xx}^{'} &= \frac{\partial^2 g}{\partial x'^2} = \frac{\kappa_{xx}+\kappa_{yy}}{2} + \frac{\kappa_{xx}-\kappa_{yy}}{2}\cos 2\beta + \kappa_{xy}\sin 2\beta, \\
\kappa_{yy}^{'} &= \frac{\partial^2 g}{\partial y'^2} = \frac{\kappa_{xx}+\kappa_{yy}}{2} - \frac{\kappa_{xx}-\kappa_{yy}}{2}\cos 2\beta - \kappa_{xy}\sin 2\beta, \\
\kappa_{xy}^{'} &= \frac{\partial^2 g}{\partial x'\partial y'} = \frac{\kappa_{yy}-\kappa_{xx}}{2}\sin 2\beta + \kappa_{xy}\cos 2\beta.
\end{aligned} \tag{4.7}$$

The angles corresponding to the two extrema in direct curvature in the rotated coordinate system are found by setting the following derivatives to zero.

$$\begin{aligned}
\frac{\partial \kappa_{xx}^{'}}{\partial \beta} = 0 &\Rightarrow -(\kappa_{xx}-\kappa_{yy})\sin 2\beta + 2\kappa_{xy}\cos 2\beta = 0 \\
&\Rightarrow \frac{2\kappa_{xy}}{\kappa_{xx}-\kappa_{yy}} = \frac{\sin 2\beta}{\cos 2\beta} = \tan 2\beta \\
\frac{\partial \kappa_{yy}^{'}}{\partial \beta} = 0 &\Rightarrow (\kappa_{xx}-\kappa_{yy})\sin 2\beta - 2\kappa_{xy}\cos 2\beta = 0 \\
&\Rightarrow \frac{2\kappa_{xy}}{\kappa_{xx}-\kappa_{yy}} = \frac{\sin 2\beta}{\cos 2\beta} = \tan 2\beta
\end{aligned} \tag{4.8}$$

Both equations result in the same relation for β. Indeed, the angles defining the principal direction of curvature are thus $\beta = \tan^{-1}\left(2\kappa_{xy}/(\kappa_{xx}-\kappa_{yy})\right)$ and $\beta+\pi/2$. This clearly shows that the two principal directions are orthogonal. To find the equations for principal curvature, these angles are plugged back into Eq. 4.7 and the identities $\sin 2\theta = \tan 2\theta / \sqrt{1+\tan^2 2\theta}$ and $\cos 2\theta = 1/\sqrt{1+\tan^2 2\theta}$ are used. The principal curvatures are then found to be

$$\begin{aligned}
\kappa_{xx}^{'} &= \frac{\kappa_{xx}+\kappa_{yy}}{2} + \frac{\sqrt{(\kappa_{xx}-\kappa_{yy})^2 + (2\kappa_{xy})^2}}{2} \\
\kappa_{yy}^{'} &= \frac{\kappa_{xx}+\kappa_{yy}}{2} - \frac{\sqrt{(\kappa_{xx}-\kappa_{yy})^2 + (2\kappa_{xy})^2}}{2} \\
\kappa_{xy} &= 0
\end{aligned} \tag{4.9}$$

and the curvature maps determined from CGS using Eq. 4.4 can be used to calculate principal curvature maps.

For thin film-thick substrate systems, the full-field recording of all system curvature components is crucial since they can be related to the individual components of stress acting on the thin film, through analyses of the type presented in chapter 1 or other types of plate theory [3, 23-25]. This provides an easy and quick way of film stress measurement that can be instantaneously performed across an entire wafer surface. Similarly, principal stresses can be related to principal curvatures once these are obtained from measurement of individual stress component maps via Eq. 4.9.

CGS at Caltech

The method of CGS was initially developed at the Graduate Aeronautical Laboratories (GALCIT) and was applied to the study of out of plane deformation gradients at the vicinity of dynamically growing cracks in structural solids [26, 27]. The first application of CGS to the analysis of film stress is described in references [13, 14, 22]. The current CGS interferometer used for our experiments is housed in a Class 1 cleanroom in the subbasement of Firestone at Caltech (Fig. 4-3). Since the environment is quite clean, it is possible to measure wafers in between various steps of processing without having problems with wafer contamination. The current CGS system, called ALEX, was a prototype of a production tool donated to GALCIT by Oraxion Diagnostics, a Caltech start-up.

ALEX is enclosed in an outer shell. This looks quite streamlined, but makes it difficult to modify the setup or use large specimen stages (as for heating). Therefore, the

CGS measurements that were performed for our experiments are at room temperature, and are all made with the same optical setup, including laser wavelength, lens focal length, grating pitch and grating distance, etc.

Figure 4-3. Cleanroom in the basement of Firestone at Caltech, with ALEX.

The inner workings of ALEX can be seen in Fig. 4-4. ALEX uses a red collimated laser, expanded to 300 mm in diameter. The diffraction grating pitch is

1/40 mm and the distance between gratings is 60 mm. A proprietary software program called Intelliwave is used to control ALEX and analyze the data.

Figure 4-4. Inner workings of ALEX.

ALEX was intended to be a quality control tool for wafer processing, and therefore is configured to allow it to measure very small curvatures, or specimens with an average radius of curvature greater than 50 m. In order for these small curvatures to be

measured, the beam path length must be rather long. Thus, there are many mirrors reflecting the beam back and forth to increase the overall path length.

A schematic of the beam path is shown in Fig. 4-5. The practical differences between this schematic and the one in Fig. 4-1 are to allow for the longer path length. Figure 4-6 reproduces the photograph of the inside of ALEX, with the beam path traced. The laser is housed on top of the tool, and although shown in the schematic it cannot be seen in the images of Fig. 4-6.

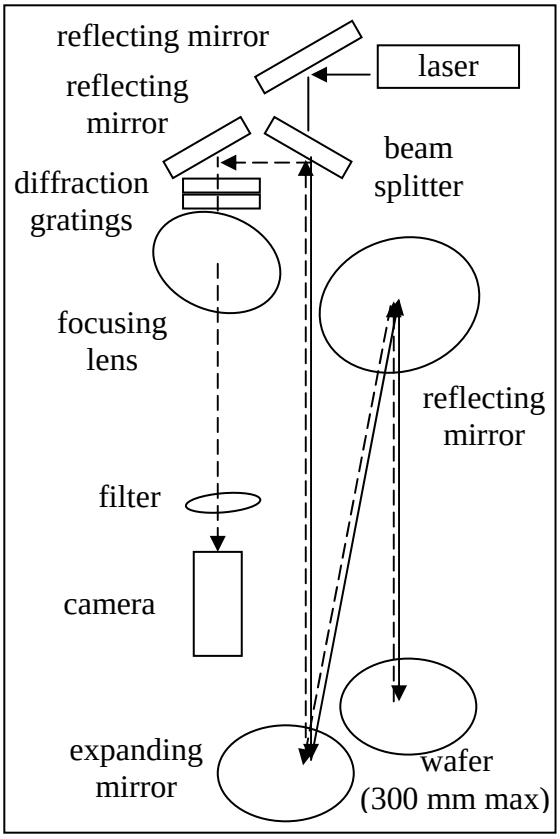

Figure 4-5. Schematic of ALEX.

The following explanation can be followed using either the schematic of Fig. 4-5 or the images in Fig. 4-6. The beam emitted from the laser is directed down into the tool, through a beam splitter, to a mirror that functions as a beam expander (Fig. 4-6a). From here, the beam is reflected up to a collimating mirror (Fig. 4-6b) which directs it down to the specimen surface (Fig. 4-6c). The beam which reaches the specimen is collimated and at near-normal incidence. Once reflected from the specimen surface, the light follows the same path in reverse until it reaches the beam splitter which is located in the center top of the figure. The portion of the reflected beam that is deflected by the beam splitter (rather than passing through it) is then reflected by another mirror that directs it down to the diffraction gratings, where the optical differentiation is performed (Fig. 4-6d). The diffracted beams subsequently pass through a focusing lens, which focuses the two diffraction orders of interest into one spot, which is allowed to pass through an aperture placed at the filter plane. Finally, the camera records the resulting interferograms.

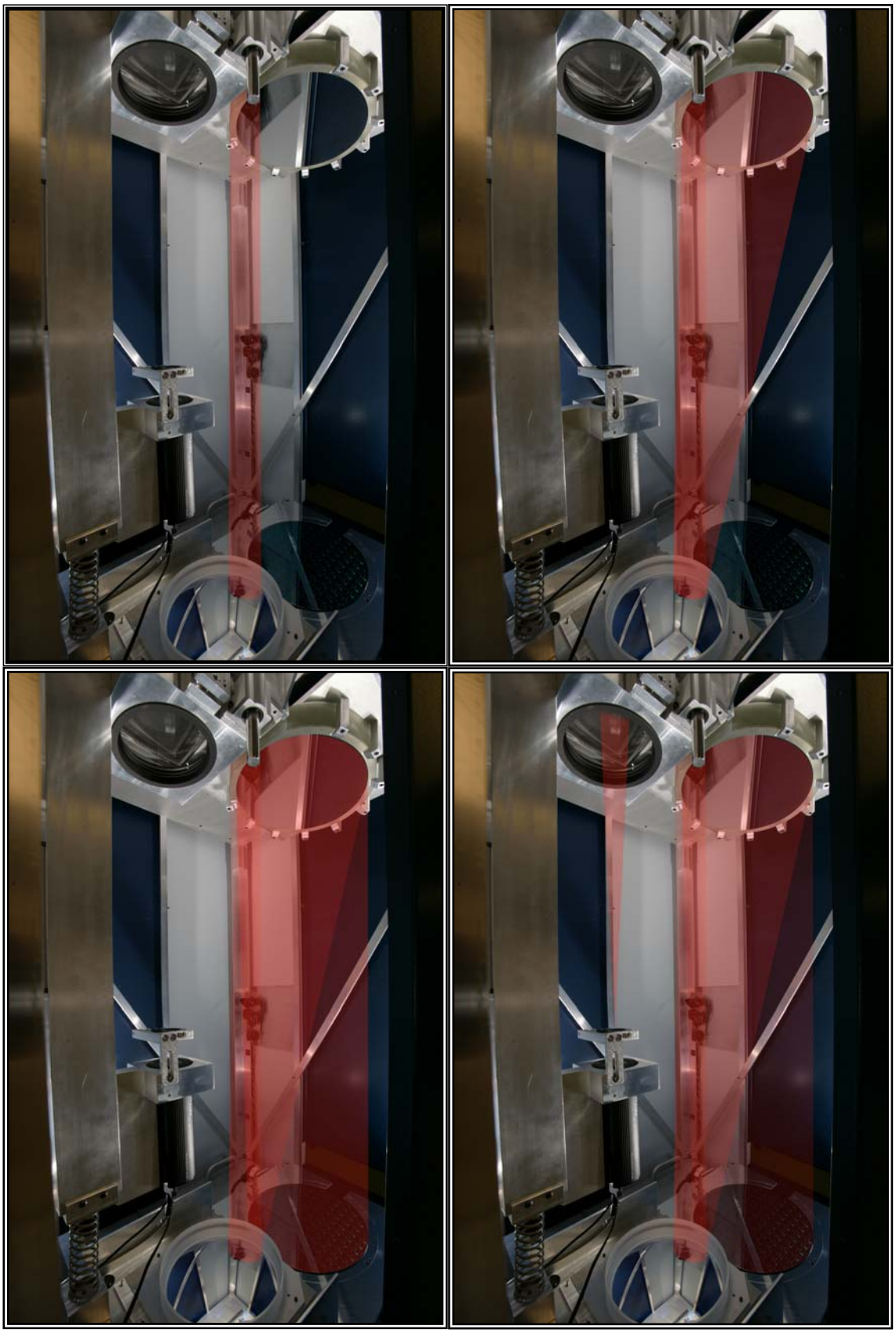

Figure 4-6. ALEX beam path.

The data collection process is as follows: First, the wafer is loaded into ALEX by being placed on an extended wafer stage that is then retracted back into the tool. At this point a live image is shown on the computer screen. When acquiring data, images are captured with the wafer stage at 0° and then 90° to get interferograms of *x* and *y* slope (Fig. 4-7 a,b).

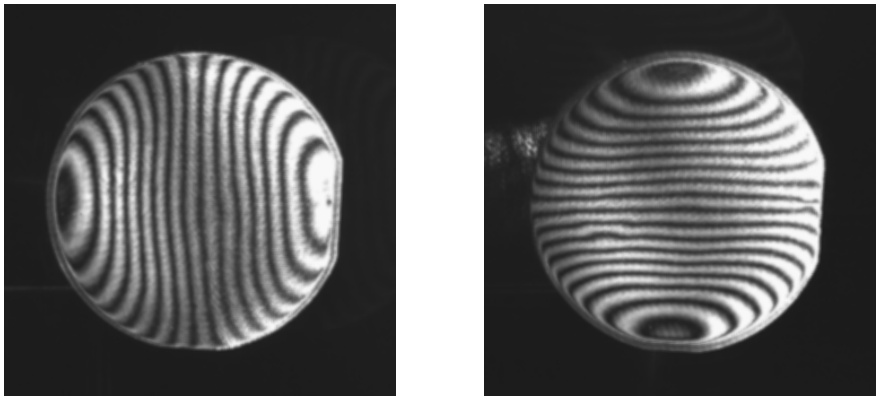

(a) (b)

Figure 4-7. Cu film on a 4" diameter Si wafer: (a) *x*-slope ($\partial f/\partial x$) and (b) *y*-slope ($\partial f/\partial y$) interferograms.

A process known as phase shifting is used to increase the resolution. Five images are taken both in *x*- and *y*- directions (Fig. 4-8). The diffraction gratings are shifted in a direction parallel each other by ¼ of the grating pitch for each image, so that the first and fifth images have the gratings aligned with each other. Viewing the five images in quick succession makes it look as if the fringes are marching across the wafer. The variation of light to dark of each pixel increases the effective resolution. Also, the direction that the fringes march indicates the sign of the curvature. This is absolutely necessary since a single image gives only slope and curvature magnitude, not sign.

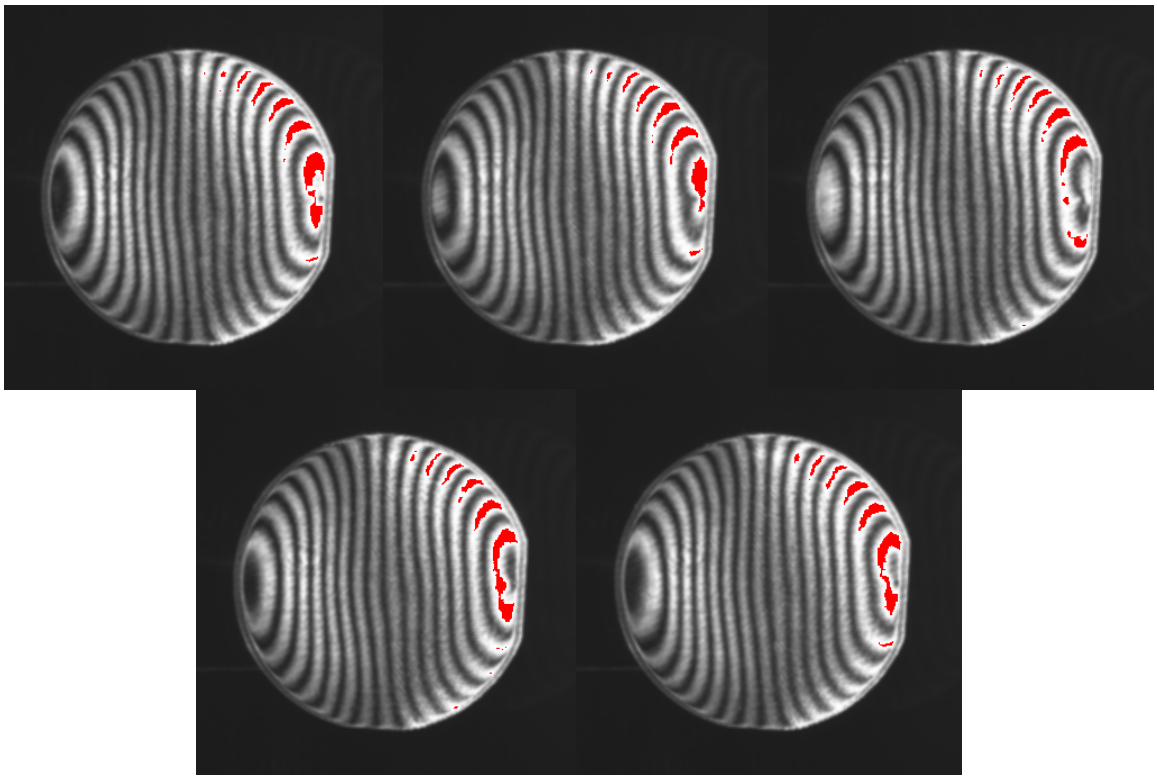

Figure 4-8. Phase shifting of $\partial f/\partial x$ from Fig. 4-7.

In order to obtain slope maps from the interferograms, the fringes must be moved to the center of the image. Since the wafer is placed on the sample stage by hand, there is no guarantee that the center of the wafer is equal to the center of stage rotation. To center the images, a circular mask with a diameter equaling that of the specimen is superimposed on the *x*-interferogram. The mask is typically off center with respect to the fringes. First, the mask is moved so that it is centered on the fringes, and the location of the mask, in pixels, is noted. The difference between the mask location and the center of the image (in pixels: 512, 512) is subtracted from the fringe location, moving the fringes to the image center. Finally, the mask is moved to the image center. The same procedure is then repeated for the y-interferograms.

The mask is at the same pixel location on the *x* and *y* images. Intelliwave assumes the wafer is also in the same location with respect to the mask in the two images

when doing its calculations; the mask is used as the reference for position on the wafer. Also, only data points inside the mask are considered when creating the digitized slope and curvature maps. Therefore, this centering process is an important step in minimizing error. Part of a screenshot showing the Intelliwave interface with the blue, circular mask on the centered *x* and *y* interferograms is shown in Fig. 4-9. The partial fringes on either side of the interferogram are due to the aperture in the filter plane being removed; they do not affect the results for a wafer this size, where they do not overlap the image of interest.

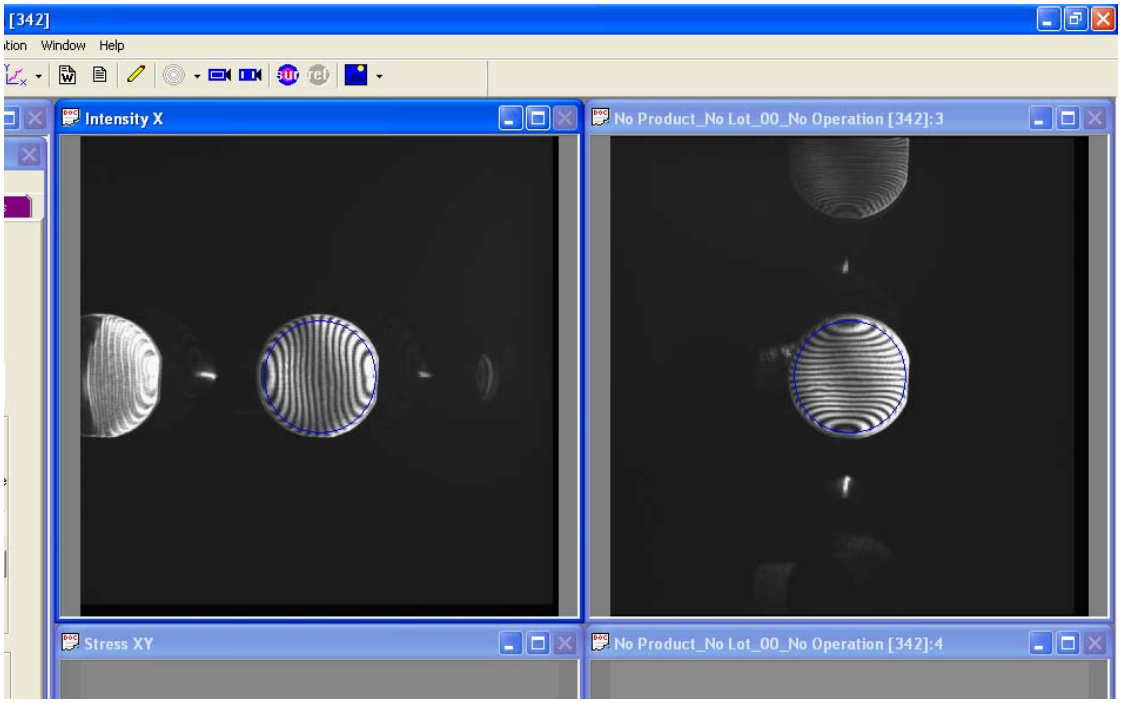

Figure 4-9. Partial screen shot of Intelliwave program, showing the centered blue circular mask on the *x*-slope and *y*-slope interferogram images. This is the same specimen as in Fig. 4-7.

The interferograms are subsequently digitized in Intelliwave, using Eq. 4.3, to produce slope maps (Fig. 4-10). During the digitization process, the data are fit to a polynomial function by a numerical analysis. This is done in order to later obtain the three curvature components by numerical differentiation of the two slope maps. The polynomial fitting uses Zernike polynomials, a 5th order polynomial set with 37 terms. While originally designed to characterize optical aberrations, this polynomial set is often

used to describe aspheric surfaces from interferometric data. In most cases, where spatial variations of slope and curvature are gradual, this fitting process is advantageous since it filters out noise and allows numerical differentiation to be performed. However, in the case of large nonuniformities, this fitting procedure can oversmooth the data (Fig. 4-11), and may need to be bypassed and replaced by offline processing.

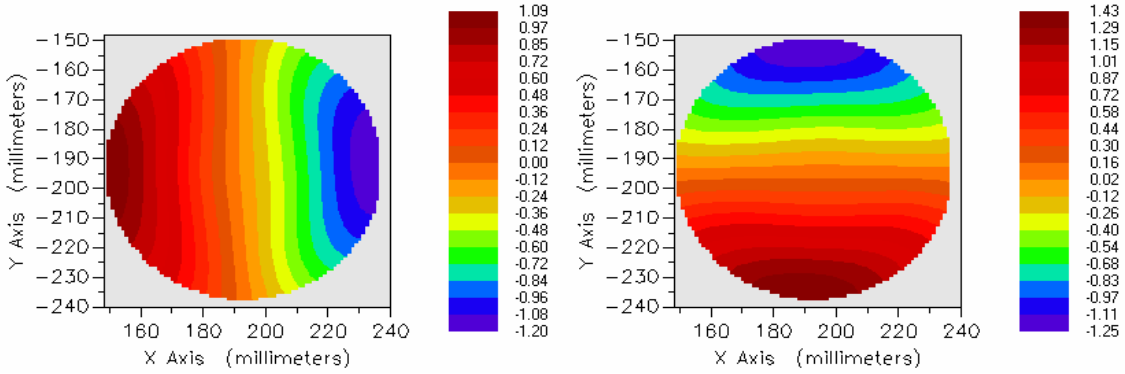

Figure 4-10. Slope maps in (a) x and (b) y, digitized from the interferograms in Fig. 4-7.

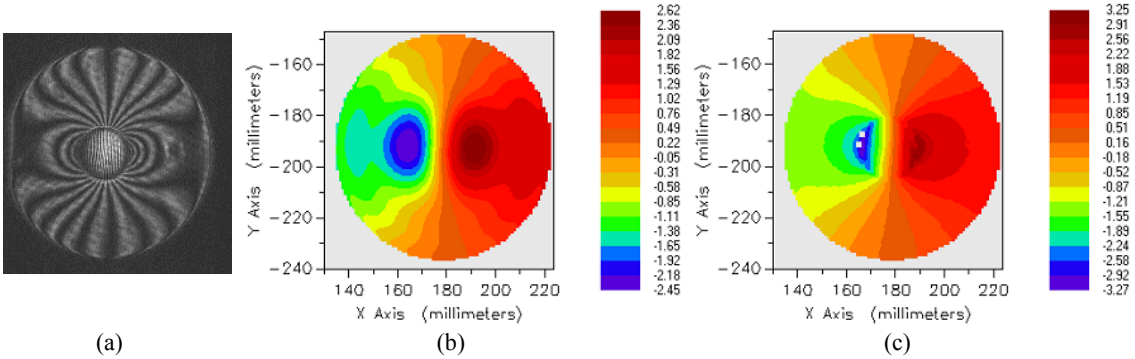

Figure 4-11. Example of oversmoothing on a specimen consisting of a 1" diameter W film island on the center of a 4" diameter Si substrate. (a) x-slope ($\partial f/\partial x$) interferogram and digitized slope maps: (b) with filtering and smoothing and (c) with no smoothing (raw data).

From here analysis can proceed in two ways: by either integrating the slope maps to get wafer topography, or differentiating to get the Cartesian curvature components. The Cartesian curvature maps κ_{xx}, κ_{yy}, and κ_{xy} are calculated by differentiating the slope

map through its polynomial fit (Fig. 4-12). The principal curvatures can also be found by using Eq. 4.9 (Fig. 4-13).

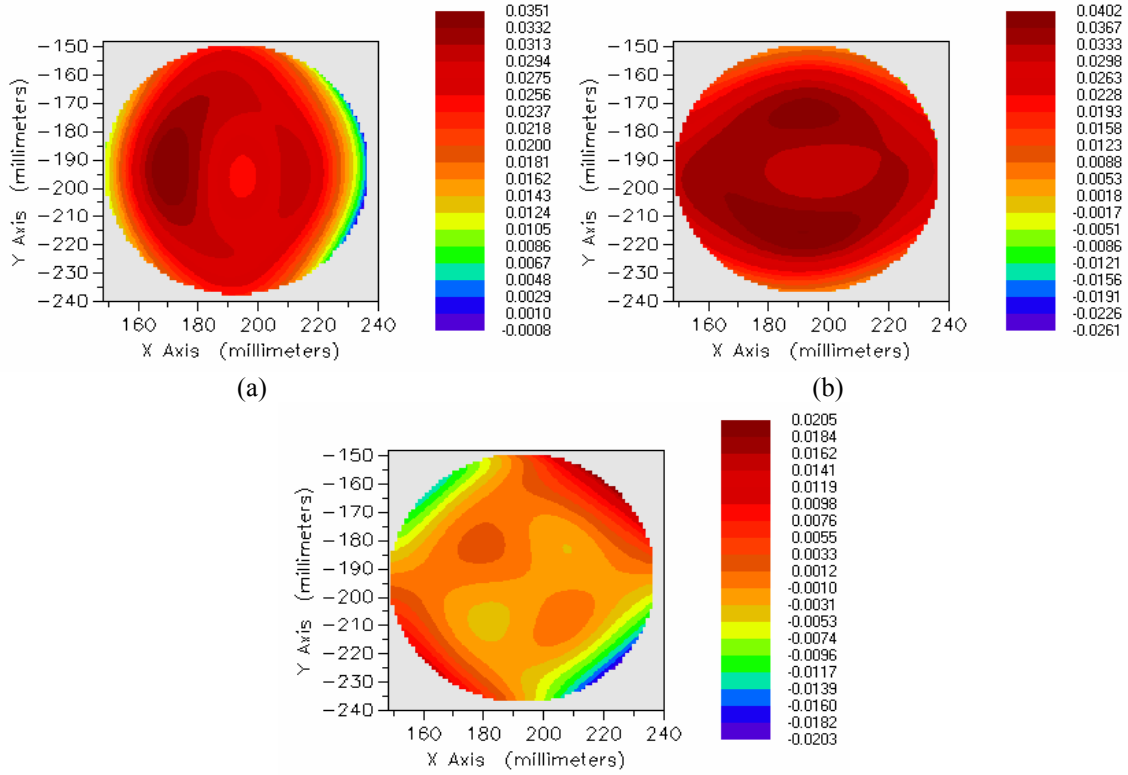

Figure 4-12. Curvature maps (a) κ_{xx}, (b) κ_{yy}, and (c) κ_{xy}, or twist, calculated from the slope maps in Fig. 4-10.

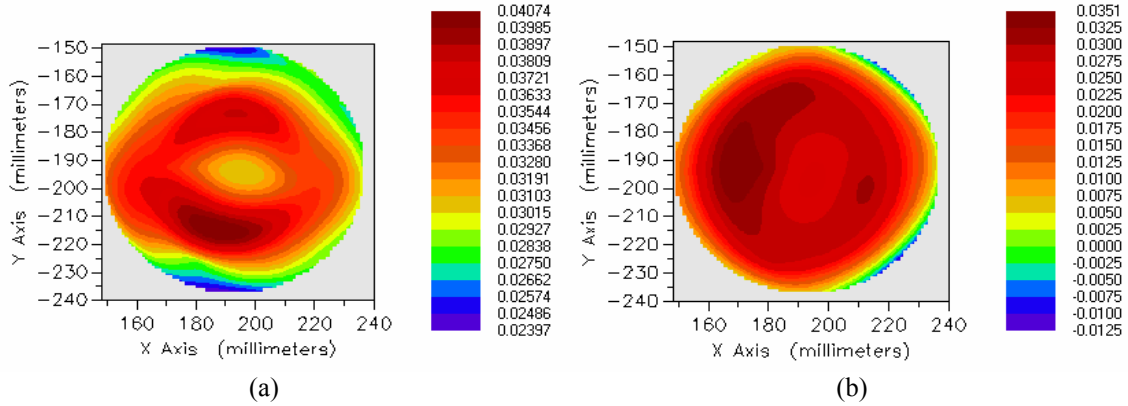

Figure 4-13. Principal curvature maps (a) κ_{max} and (b) κ_{min}, calculated from the Cartesian curvature components in Fig. 4-12 and Eq. 4.9.

Instead of using Intelliwave to calculate curvature, processing can be performed offline by using the program Matlab. In order to do this, the data are first exported from Intelliwave by saving the slope and curvature data matrices as text files. Then, they are opened in Matlab and manipulated to remove the headers and to be rotated to the correct orientation (the x and y vectors in Intelliwave and Matlab are reversed). The slope data are interpolated to create a much finer map (Fig. 4-14). Finally, this interpolated slope map is differentiated to obtain the κ_{xx}, κ_{yy}, and κ_{xy} curvature maps.

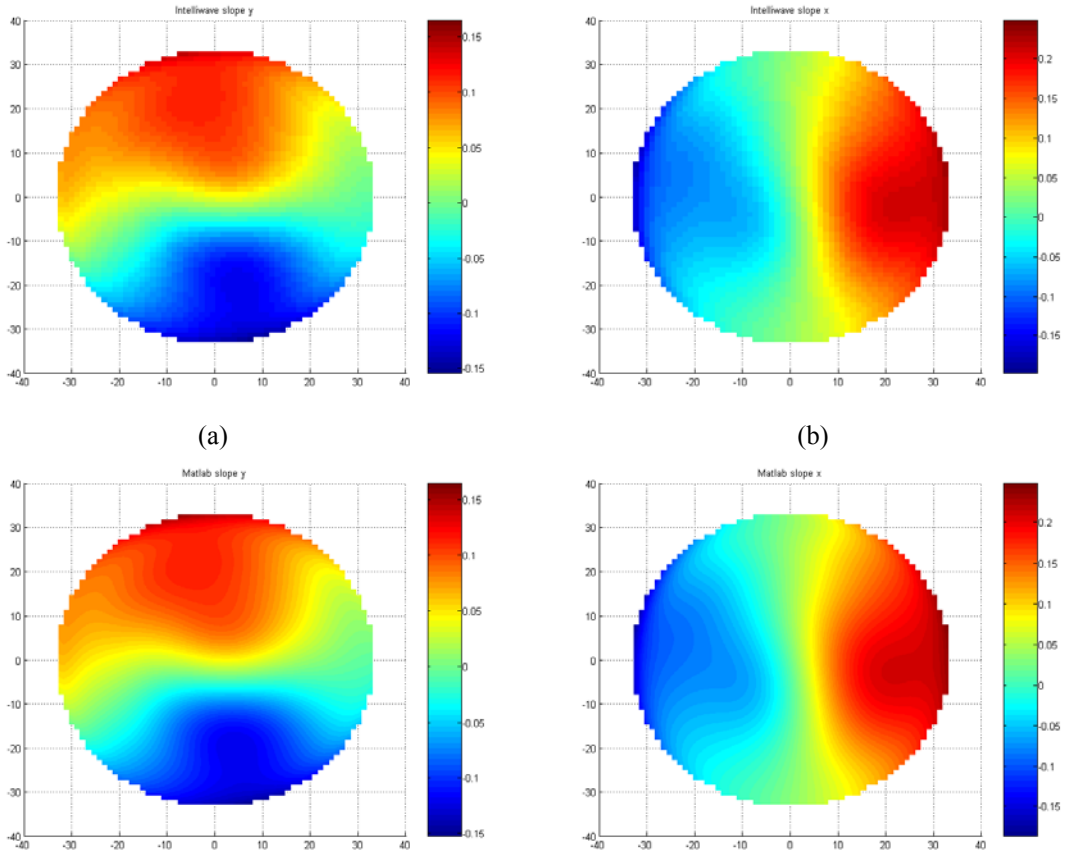

(a) (b)

(c) (d)

Figure 4-14. Slope maps in (a) x and (b) y from Intelliwave and interpolated in Matlab (c),(d). This specimen is a 3" diameter GaAs substrate with a InGaAs film.

In many practical cases, the curvature maps calculated using Intelliwave and Matlab are the same (Fig. 4-15). The exception to this is when curvature discontinuities are present and the slope maps are oversmoothed, as explained earlier. When this oversmoothing occurs, it is fairly obvious to see by eye by comparing the interferograms and digitized slope maps. When this happens, the raw data (before filtering and fitting) are exported from Intelliwave and the above procedure is followed in Matlab to obtain curvature maps. Otherwise, since it is easier to obtain curvature maps from Intelliwave than it is using Matlab, the curvature data calculated in Intelliwave are used.

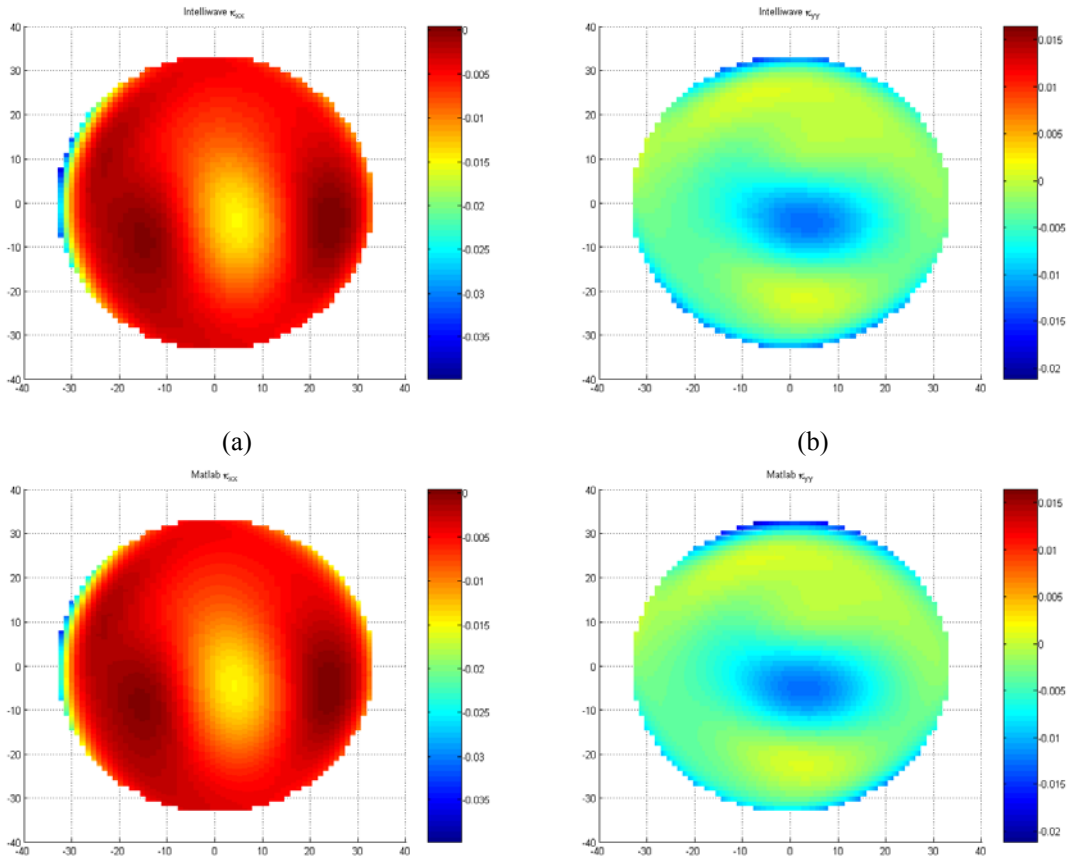

Figure 4-15. κ_{xx} (a,c) and κ_{yy} (b,d) maps from Intelliwave (top) and Matlab (bottom). The specimen is the same as in Fig. 4-14.

In order to determine stress, two sets of measurements are taken, one before and one after each processing step of interest. In the present study, this is typically done before and after film deposition (Fig. 4-16). In Intelliwave, the pre-process slope map (e.g., bare wafer substrate) is subtracted from the postprocessed map (e.g., wafer with deposited film) to obtain delta slope maps (Fig. 4-17). These new slope maps are then differentiated to obtain delta curvatures (Fig. 4-18), which are used as an input to the stress equations.

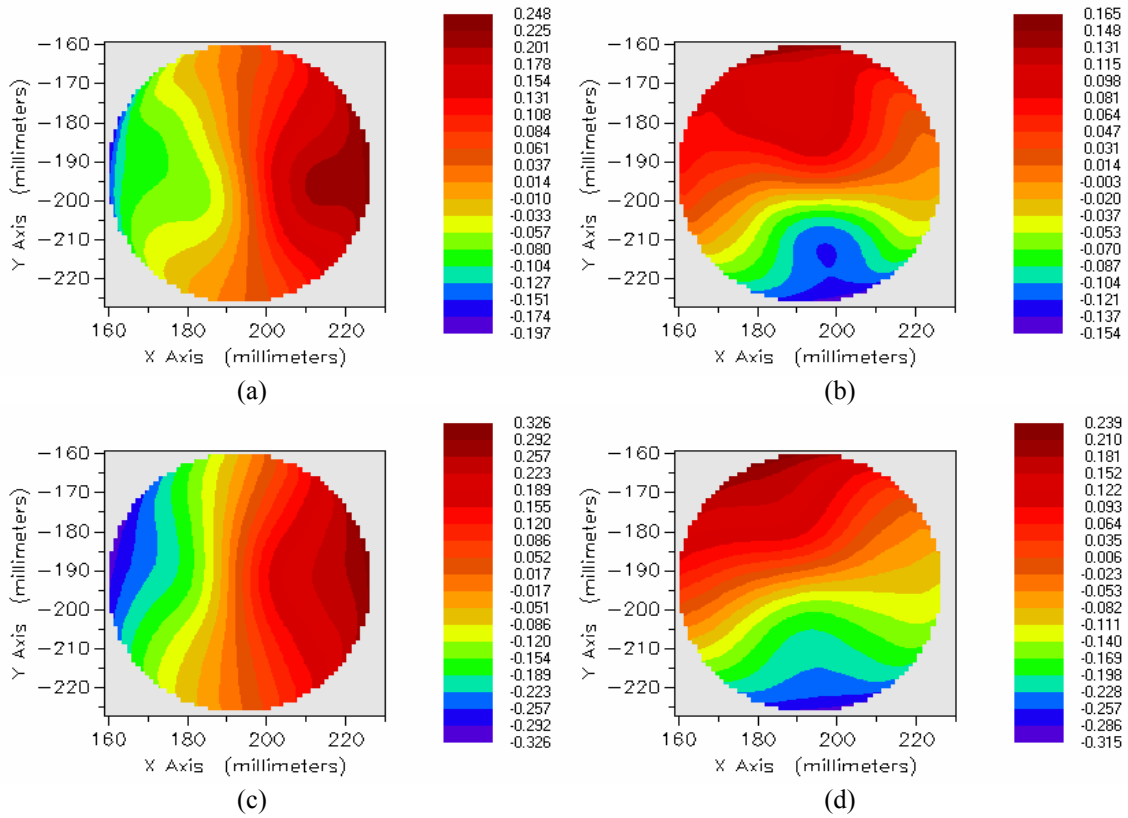

Figure 4-16. Slope maps in *x* (a),(c) and *y* (b),(d) of a 3" diameter GaAs wafer. Bare wafer (top) and with an InGaAs film (bottom).

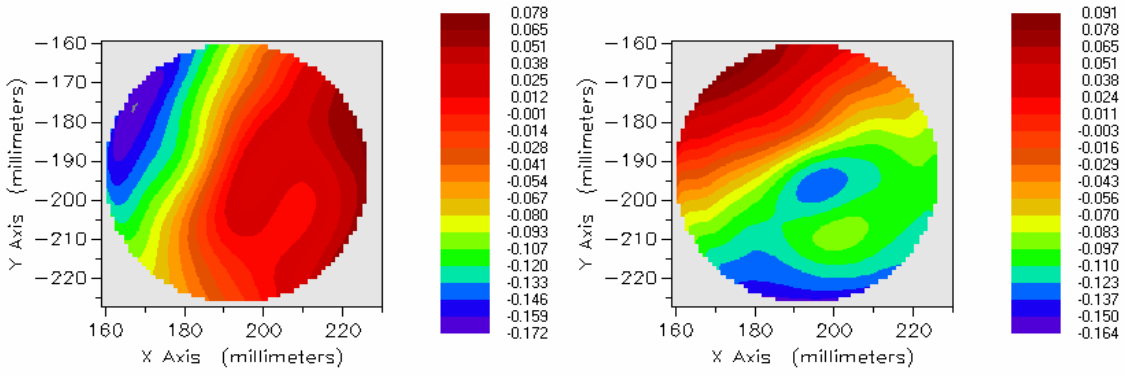

(a) (b)

Figure 4-17. Delta slope maps in (a) *x* and (b) *y*, post deposition minus bare wafer.

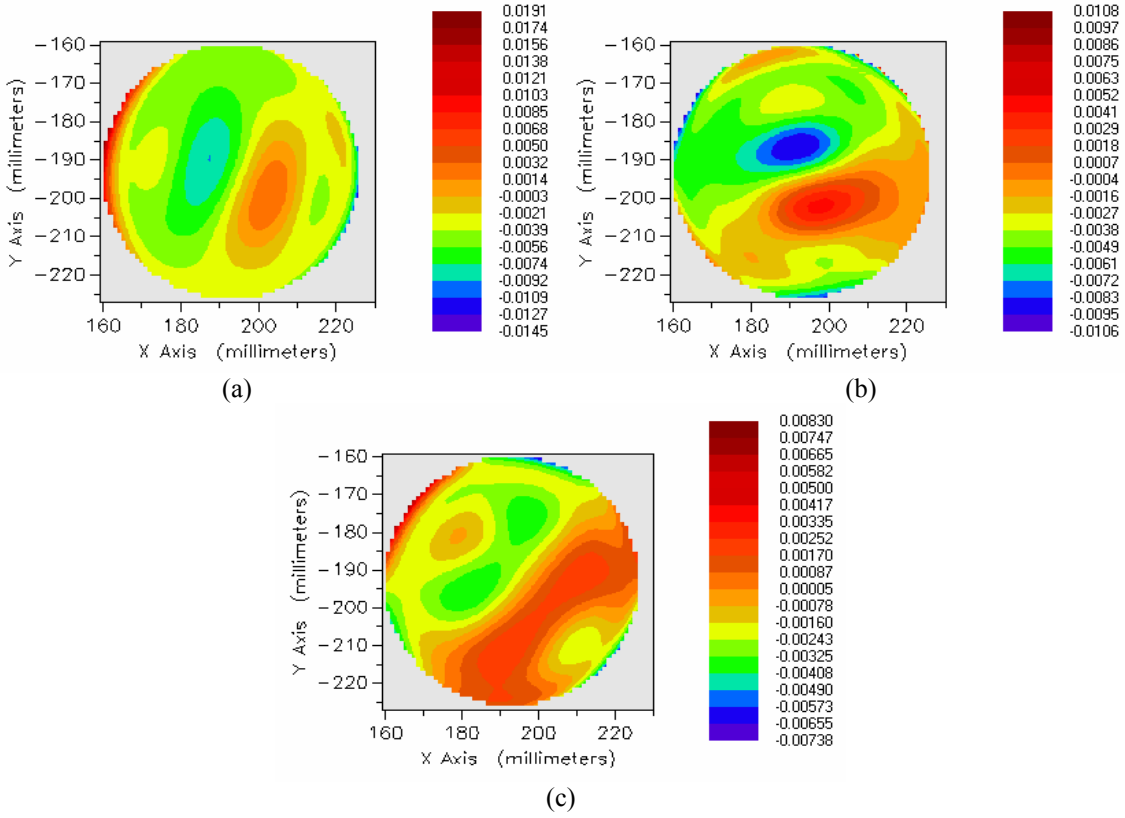

(a) (b)

(c)

Figure 4-18. Delta curvature maps obtained from slope maps in Fig. 4-17: (a) κ_{xx}, (b) κ_{yy}, and (c) κ_{xy}.

Stress can be inferred from delta curvature in Intelliwave only via the local Stoney relation. In order to use the new nonlocal HR relations, the data must be exported from Intelliwave and analyzed using Matlab.

5. CGS Measurements of Island Geometries

Thus far, a methodology which is able to determine film stress in the presence of nonuniformities has been introduced and verified by comparison to X-ray diffraction measurements. Since this methodology requires knowledge of curvature information over the entire wafer, a full-field curvature measurement technique, CGS, has also been introduced. In this chapter, CGS measurements are taken of several test wafers, and the HR methodology stress results are compared to those of Stoney.

The thin film-wafer substrate geometry used here consists of various arrangements of circular film islands on otherwise bare substrates. This generic type of geometry was chosen because it is fairly idealized, yet can easily cause both radially symmetric and non-symmetric curvature states in the wafer by just shifting the island position. Our goal is to examine the effect of island position (e.g., near the substrate center versus the substrate edge) on the stress state of the film material.

We first examine the general nature of deformation for a film island-wafer substrate geometry, with a central island. To do so, the radially symmetric specialization of the HR relations (Eq. 1.31) are further specialized to the case of film thickness described by a step function (i.e., zero film outside the island, and a constant thickness within the island) and constant film stress. These simplified relations are then integrated to find the relationship between wafer deformation and film stress. Although the film stress is not generally constant for a real system, the correlated slope and curvature profiles of the idealized constant stress and thickness case provide useful clues as to the

type of deformation that would be present in a "real" island-substrate system where neither film stress nor thickness are constant.

The analysis shows that the wafer curvature within the film-covered region is spatially constant and equibiaxial, i.e., $\kappa_{rr} = \kappa_{\theta\theta} = \kappa$, where κ is independent of the radial position r. (The radii of the island and substrate are denoted by R_f and R_s, respectively, while their respective thicknesses are h_f and h_s.) In the film-covered region the sample curvatures are given by

$$\kappa_{rr} = \kappa_{\theta\theta} = \kappa = \frac{6h_f\sigma_f(1-\nu_s)}{E_s h_s^2}\left[1-\frac{1-\nu_s}{2}\left(1-\frac{R_f^2}{R_s^2}\right)\right], \qquad 0 \le |r| \le |R_f|, \tag{5.1}$$

and the system deforms as a sphere.

Outside the film covered region, however, the system curvatures κ_{rr} and $\kappa_{\theta\theta}$ are not equal and are strong functions of the radial position r. Despite the fact that this region is not covered by the film, its curvature components are non-zero and their magnitude depends on the magnitude of the stress of the film island as

$$\kappa_{rr} = \frac{\partial^2 f}{\partial r^2} = \kappa\frac{1-\dfrac{1+\nu_s}{1-\nu_s}\dfrac{R_s^2}{r^2}}{1+\dfrac{1+\nu_s}{1-\nu_s}\dfrac{R_s^2}{R_f^2}},$$

$$\kappa_{\theta\theta} = \frac{1}{r}\frac{\partial f}{\partial r} = \kappa\frac{1+\dfrac{1+\nu_s}{1-\nu_s}\dfrac{R_s^2}{r^2}}{1+\dfrac{1+\nu_s}{1-\nu_s}\dfrac{R_s^2}{R_f^2}}, \qquad |R_f| \le |r| \le |R_s| \ . \tag{5.2}$$

Comparison of the expressions for κ_{rr} from within and outside the film-covered region reveals a finite jump in radial curvature which involves a change of curvature sign across the circular interface $r = R_f$.

The radial slope component $\partial f/\partial r$ can now be computed from Eqs. 5.1 and 5.2 and is given by the following relations for the two regions:

$$\frac{\partial f}{\partial r} = \kappa_{\theta\theta} r = \kappa_{rr} r = \kappa r, \qquad 0 \le |r| \le |R_f|, \tag{5.3}$$

$$\frac{\partial f}{\partial r} = \kappa_{\theta\theta} r = \kappa \frac{1 + \dfrac{1+\nu_s}{1-\nu_s}\dfrac{R_s^2}{r^2}}{1 + \dfrac{1+\nu_s}{1-\nu_s}\dfrac{R_s^2}{R_f^2}} r, \qquad |R_f| \le |r| \le |R_s|. \tag{5.4}$$

In this idealized case, the theory predicts that within the film-covered region, there is a linear variation of slope with position while the variation of slope outside the film-covered region is more complex. At the interface $r = R_f$, the slopes are, as expected, continuous. Figure 5-1 shows the predicted variations of the two non-zero curvature components and the radial slope component, based on the geometry and material parameters of the W-Si system described in chapter 3 and an assumed constant film stress, σ_f, of -1.5 GPa. The theoretically predicted features discussed above are obvious from the figure.

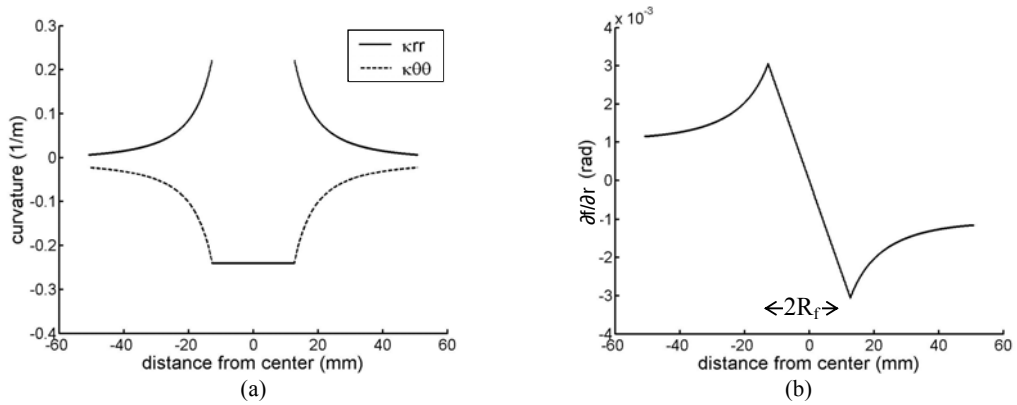

Figure 5-1. The curvature (a) and slope (b) profiles across the diameter of a wafer with a central film island of constant thickness. The film stress is assumed to be a constant -1.5 GPa.

An example of the CGS slope-interferograms from a real wafer with a central film island is shown in Fig. 5-2. This wafer was the specimen used in chapter 3 for the verification of the HR relations as compared to μXRD measurements. The film island is distinctly visible on the *x*- and *y*- interferograms as a circle in the middle of the image. The fringe pattern in that region consists of dense, straight, more or less evenly spaced lines that correspond to a constant equibiaxial curvature, as predicted by the analysis. Outside the film island, there is still a less dense but more complex fringe pattern, since there is a non-zero curvature in that area due to the circumferential constraints on the Si wafer. This is also qualitatively consistent with the analysis.

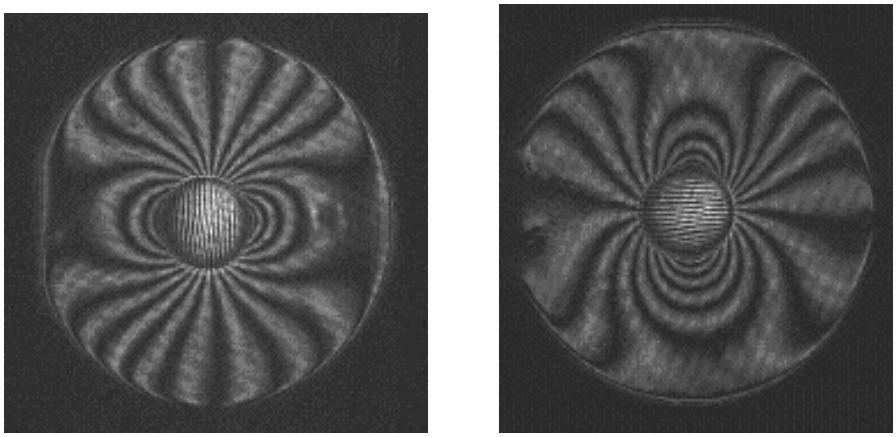

(a) (b)

Figure 5-2. CGS slope interferograms of a wafer with a central film island, (a) $\partial f/\partial x$ and (b) $\partial f/\partial y$.

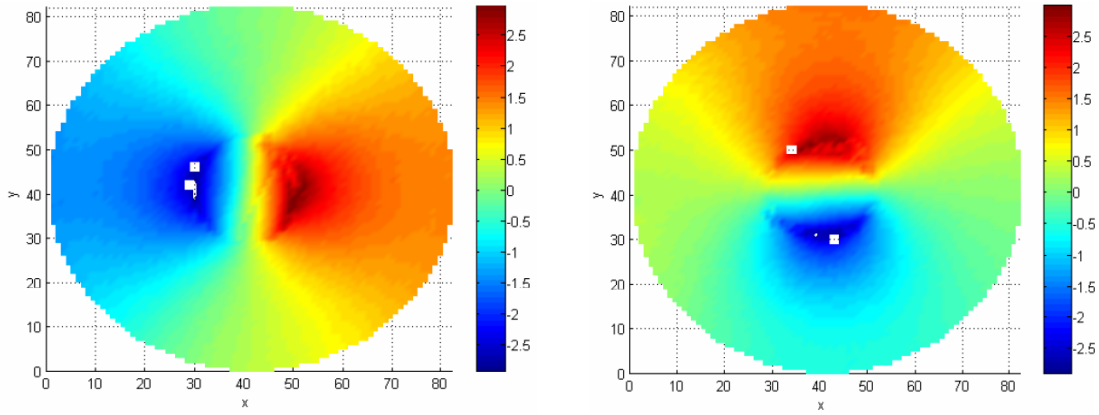

(a) (b)

Figure 5-3. CGS digitized slope maps of a wafer with a central film island, (a) $\partial f/\partial x$ and (b) $\partial f/\partial y$.

The slope maps are shown in Fig. 5-3. These maps feature the expected straight, evenly spaced lines of constant slope within the island. Also, the transition between film-covered and bare substrate regions is quite sharp; the outline of the island can be easily traced out on these maps.

The topography of a wafer with a central film island can be obtained by direct integration of the two slope maps of Fig. 5-3 and is shown in Fig. 5-4. Consistent with theory (as visualized in Fig. 5-1), the sign of the radial curvature component κ_{rr} changes across the film edge. The film region has a negative, constant curvature; there is a jump in curvature from negative to positive at the film edge; and there is a non-zero curvature outside the film.

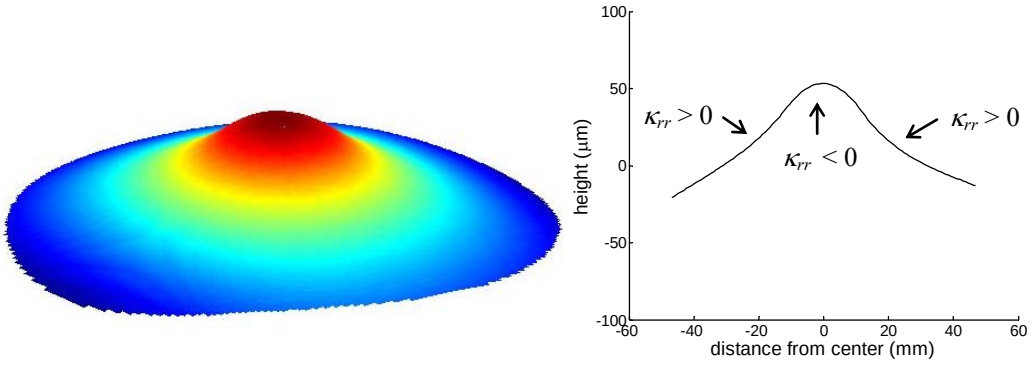

Figure 5-4. Wafer with a central film island. Shape: (a) full map and (b) profile across the wafer diameter.

Although the experimentally obtained wafer slopes and shape have the general shape predicted by the idealized case of constant stress and film thickness, the CGS measurements vary in detail with the predictions and suggest the presence of a nonuniform stress state in the island. Indeed this was already shown to be the case through the μXRD measurements described in chapter 3. In what will follow, CGS measurements will be used to extract the film stress distribution and to study the effect of film location on its magnitude and spatial distribution.

In general, to determine stress from CGS measurements, interferograms are taken before and after film deposition, and the delta (difference) slope maps are used to obtain delta curvature maps, and then film stress through the stress/curvature relations as described in chapter 1. From here on, the terms "slope" and "curvature" will actually refer to the delta slope and curvature, i.e., the difference between the postdeposition and predeposition maps.

Extracting Stress from CGS Measurements

The specimens used in this study consist of 1 mm thick, 100 mm diameter <111> Si wafer substrates with W film islands. It is important to note that the deposition was performed in a system without active heating or cooling. The substrate is thus not expected to incur deformation due to thermal effects. This particular orientation Si wafer was used because it is in-plane isotropic, as is W.

The island thickness is approximately 1.8 μm in the central part of the island, and decays near the island edge. The island diameters are all approximately 20 mm. The film and the in-plane substrate Young's moduli are 411 GPa and 160 GPa, and the Poisson ratios are 0.28 and 0.27, respectively.

Three specimens were examined. The first has a central film island. This is not, however, the same wafer that was examined earlier (Fig. 5-3), since that particular wafer was heavily damaged before the measurements could be completed. Instead, the wafer examined here is one of a new batch of wafers which have progressively more interesting island film geometries. The second specimen has an off-center film island, located approximately 20 mm from the wafer centerline. The third specimen consists of an array of four islands, equally spaced approximately 25 mm from the wafer center. All islands have an approximate radius of 20 mm.

For each island, the film thickness is approximately constant over the central region. At about 1.5 mm from the island edge, however, the film thickness begins to decrease, until it eventually drops to zero. The thickness profiles are very similar to that of the wafer measured in chapter 3.

For each wafer, slope and curvature maps are obtained, from CGS interferometry. The curvature maps are then used in conjunction with both the Stoney and the HR methodologies to determine film stress in the film islands.

Central Film Island

The new specimen featuring a central W film island is considered first. The slope map of this wafer is shown in Fig. 5-5. The island location and wafer radius are indicated in this figure and all of the following CGS maps.

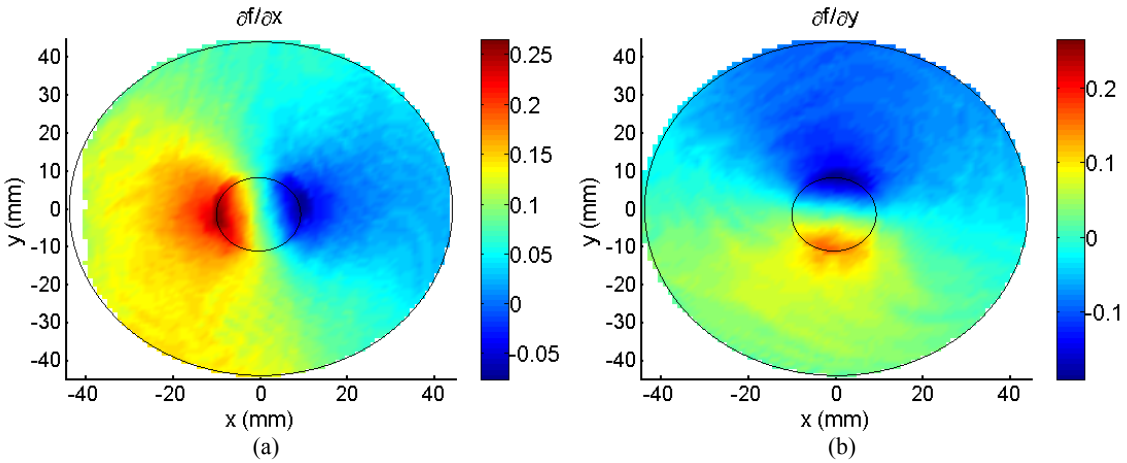

Figure 5-5. Slope maps of centered island: (a) $\partial f/\partial x$, (b) $\partial f/\partial y$.

As expected, within the island radius the lines of constant slope are straight and evenly spaced. Since this island lies in the center of the wafer, the wafer has radial symmetry. This is conclusively illustrated by using the Cartesian slope of Fig. 5-5 to construct the radial slope map, $\partial f/\partial r$. The axisymmetric shape of that map, shown here in Fig. 5-6, illustrates the axisymmetry of the film/substrate system.

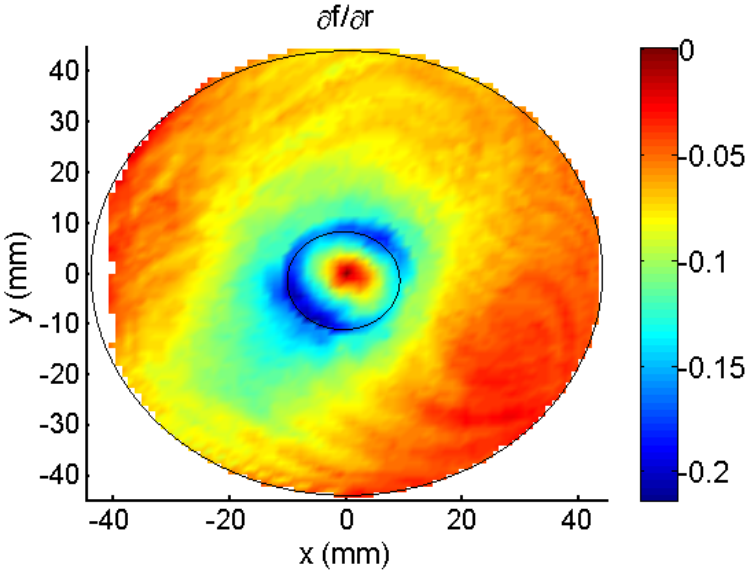

Figure 5-6. Radial slope map, $\partial f/\partial r$, of centered island.

A dataset corresponding to the straight line running through the diameter of the wafer, $x = 0$, was first extracted from the map of $\partial f/\partial y$. This diameter was chosen in order to compare results with the off-center wafer in a later section, and the resulting slope is shown in Fig. 5-7. Within the film island, the slope is relatively linear. Outside of the island, however, the slope changes direction (curvature changes sign) and then drops back to zero, as qualitatively expected based on the highly idealized analytical prediction in the first part of this section (Eqs. 5.3 and 5.4).

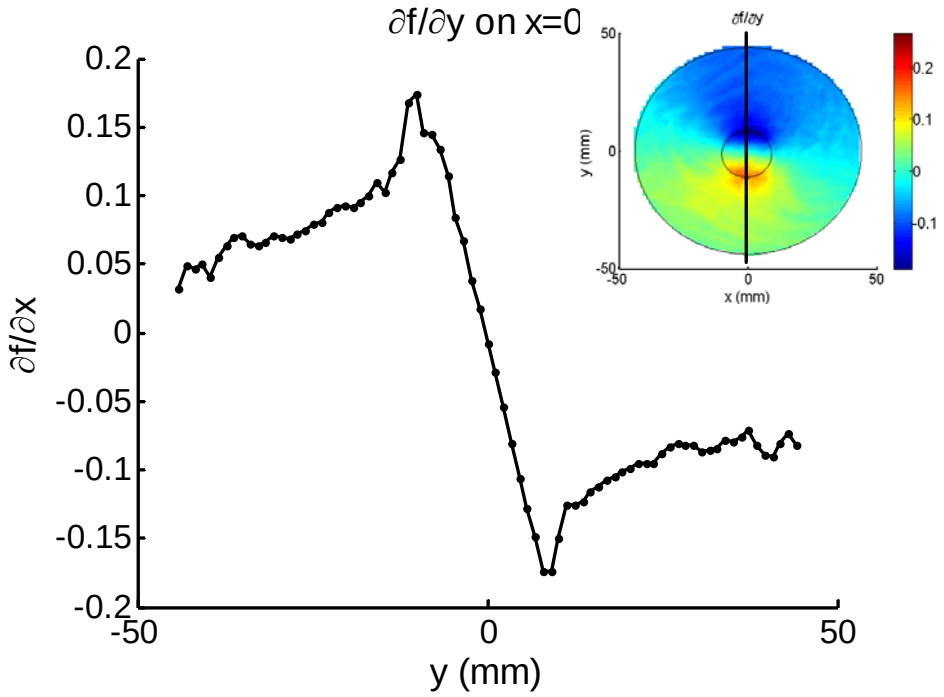

Figure 5-7. Plot of slope ($\partial f/\partial y$) through wafer diameter.

Curvature maps are displayed in Fig. 5-8. These include κ_{xx}, κ_{yy}, and the principal curvatures κ_{max} and κ_{min}. Recall that for the stress analysis both curvature components are required for the evaluation of stresses (Eq. 1.31). As expected, the maximum curvature map is also radially symmetric, with a slowly varying negative curvature within the film island which jumps to a narrow band of positive curvature just outside the island and then drops to zero as the distance from the island edge is increased.

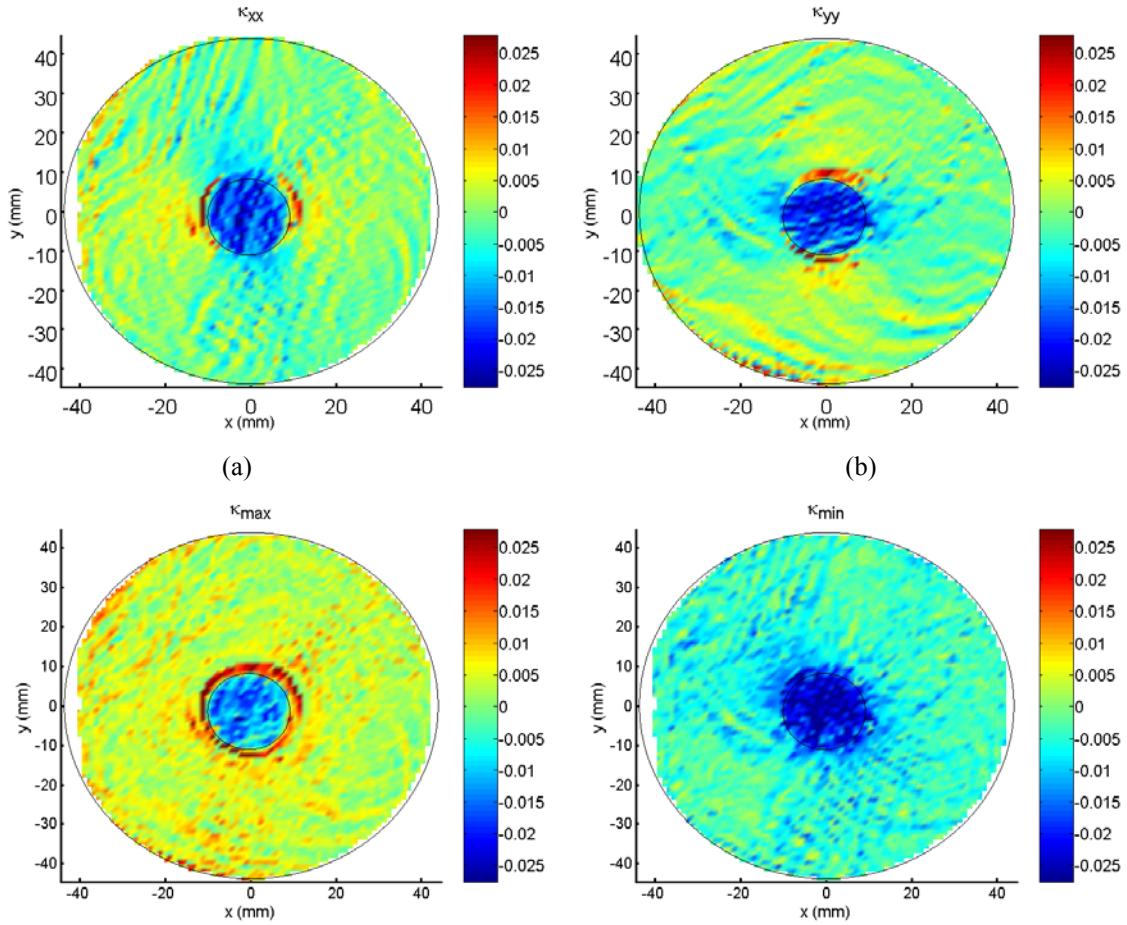

Figure 5-8. Curvature maps for a central film island: (a) κ_{xx}, (b) κ_{yy}, (c) κ_{max} and (d) κ_{min}.

Since the wafer is only covered in film within the island, that is obviously the only location where film stress exists. The magnitudes of the sum of stresses ($\sigma_{xx} + \sigma_{yy}$) obtained from the Stoney and HR methodologies are shown in Fig. 5-9.[1] As expected, the HR stresses are of a higher magnitude than Stoney predicts, since there is curvature outside the film that is not considered by Stoney. Also, only the HR methodology takes into account the varying film thickness. Near the island edge, where the film thickness drops drastically, the stress magnitude increases precipitously.

[1] The stress sum is compressive, so the negative of the stress is shown for reasons of clarity of discussion.

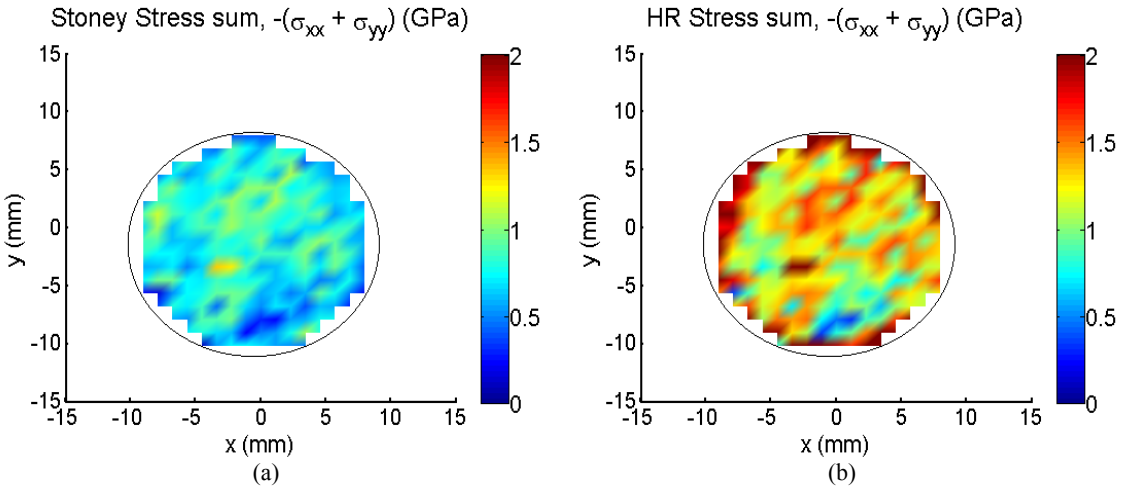

Figure 5-9. Stoney and HR stress sum ($\sigma_{xx}+\sigma_{yy}$) maps for a central film island.

The stress concentration near the film edge is also shown in Fig. 5-10. This figure compares the Stoney and HR stresses along the same diameter as was used to display the earlier slope and curvature distributions. Figure 5-10a shows the actual (raw) data points, while Fig. 5-10b displays a smoothed fit to the data, which becomes useful for comparison purposes later. In the center of the island, the two analyses reveal similar spatial distributions, though the HR methodology predicts a higher magnitude of stress. Near the island edge, the HR methodology captures a strong increase in film stress. This is undetected by the Stoney analysis. Qualitatively the stress distribution measured by CGS is very similar to those measured in a similar wafer through μXRD as discussed in Fig. 3-9.

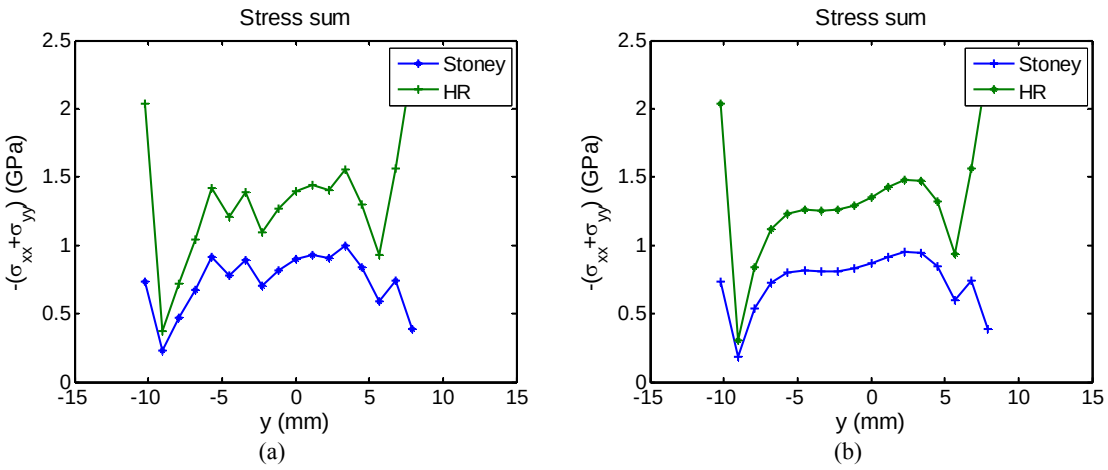

Figure 5-10. Stoney and HR stress sum ($\sigma_{xx}+\sigma_{yy}$) line plots through the diameter $x = 0$ for a central film island, (a) data and (b) fit to data, for ease of comparison.

From the HR analysis, the interfacial shear stresses, τ_r and τ_θ, can also be calculated, and are shown in Fig. 5-11. Both shear stresses are extremely small compared to the in-plane stresses. It is interesting to point out, however, that the radial shear stress exists mostly near the film edge and is related to the strong radial gradient of $\kappa_{rr} + \kappa_{\theta\theta}$. It should also be noted at this point that the formula relating this stress to the curvature gradients does not explicitly depend on h_f.

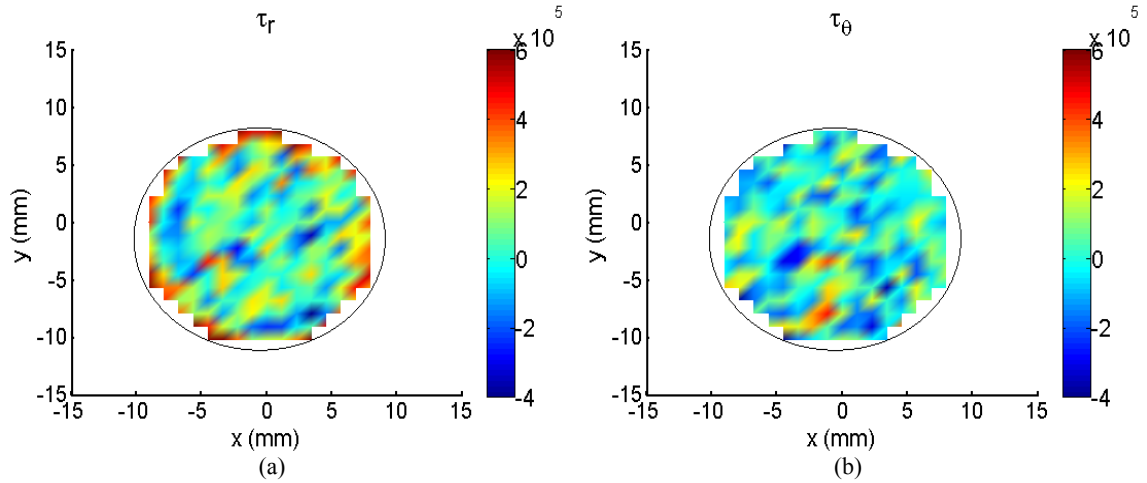

Figure 5-11. Interfacial shear stress in a central film island, (a) τ_r and (b) τ_θ.

Off-center Film Island

The next specimen to be examined has an off-center W film island, located approximately 20 mm below the centerline, $y = 0$. The slope maps, $\partial f/\partial x$ and $\partial f/\partial y$, are shown in Fig. 5-12.

While the lines of constant slope within this film island are still approximately straight and evenly spaced, the global radial symmetry of the first case is now broken. This is illustrated by the radial slope map, $\partial f/\partial r$ (Fig. 5-13), which no longer has the constant slope rings which indicate axisymmetry and were seen in Fig. 5-6.

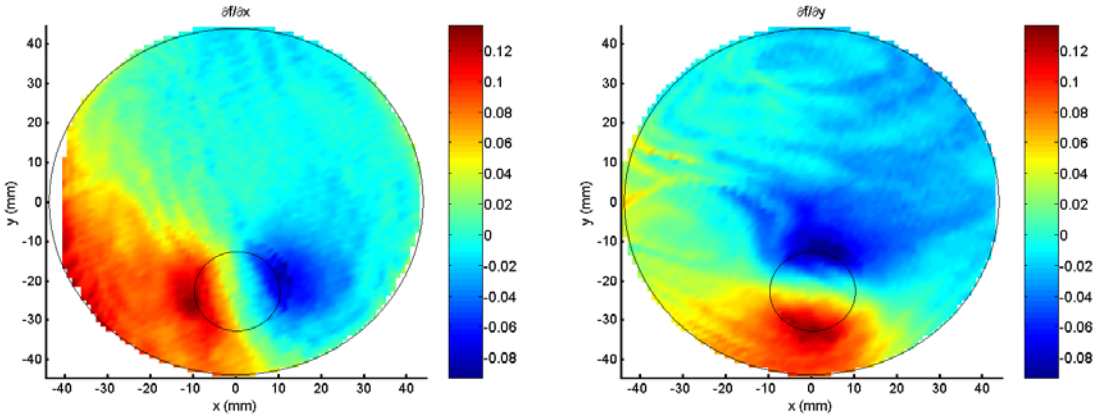

(a) (b)

Figure 5-12. Slope maps (a) ∂f/∂x and (b) ∂f/∂y of an off-center island wafer.

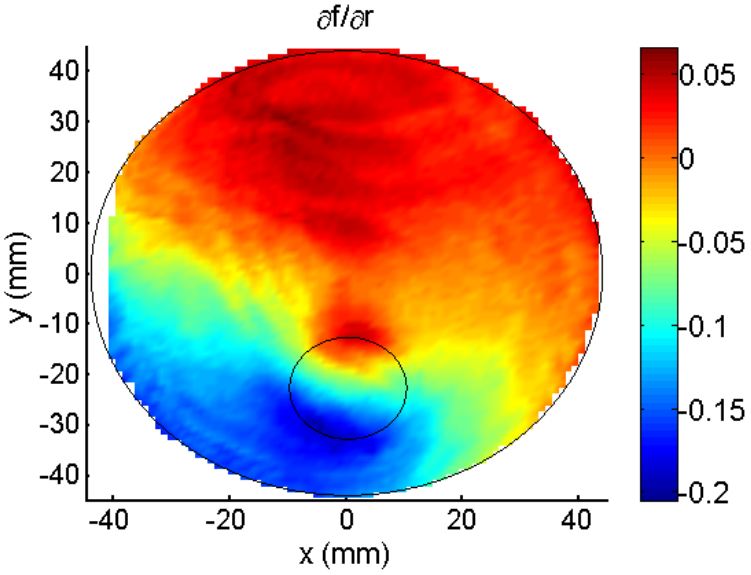

Figure 5-13. Slope map $\partial f/\partial r$ of an off-center island wafer.

The data from a straight line running through the wafer diameter ($x = 0$) were extracted. This diameter was chosen so that the line would run though the island diameter, and the data are displayed in Fig.5-14. The film island is centered approximately at $y = -20$ mm, and once again the slope is approximately linear within the island. Outside of the film island, the slope changes direction and goes back toward being constant (i.e., zero curvature). Since this island is near one side of the wafer, the slope is able to reach a constant value. It takes approximately 20 mm for this to happen.

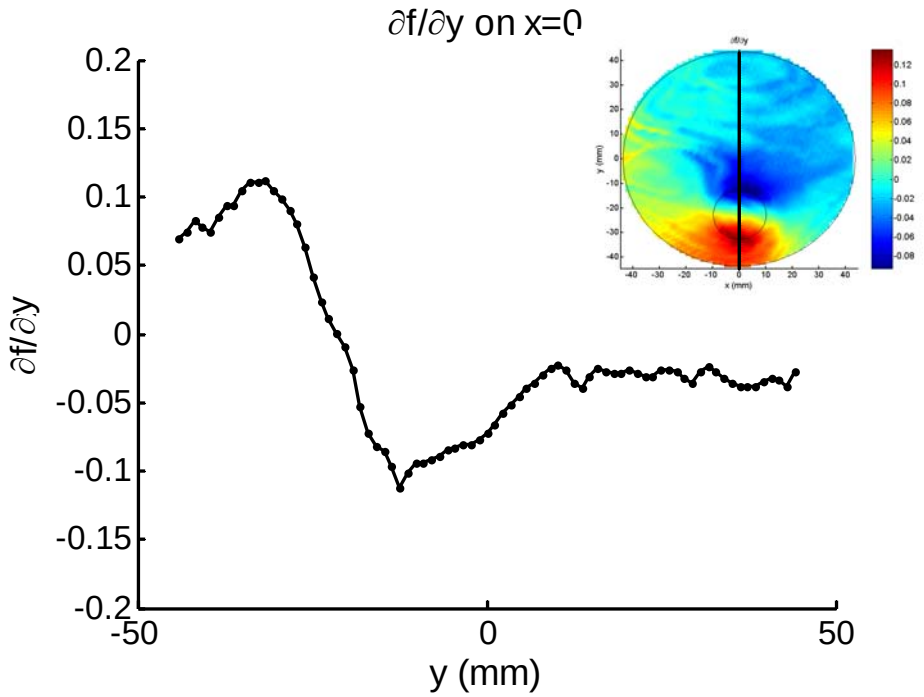

Figure 5-14. Slope line through the diameter, $x = 0$.

Curvature maps for this wafer, including κ_{xx}, κ_{yy}, and the principal curvatures κ_{max} and κ_{min}, are displayed in Fig. 5-15. The maximum curvature map shows that within the island, the curvature is approximately constant. Outside of the island, there is a faint ring of high curvature, but then far from the island the curvature drops to zero. The effects of the film island on the wafer deformation are thus qualitatively consistent to those of the central film island wafer, even though symmetry is broken and the location of the curvature maxima is now changed.

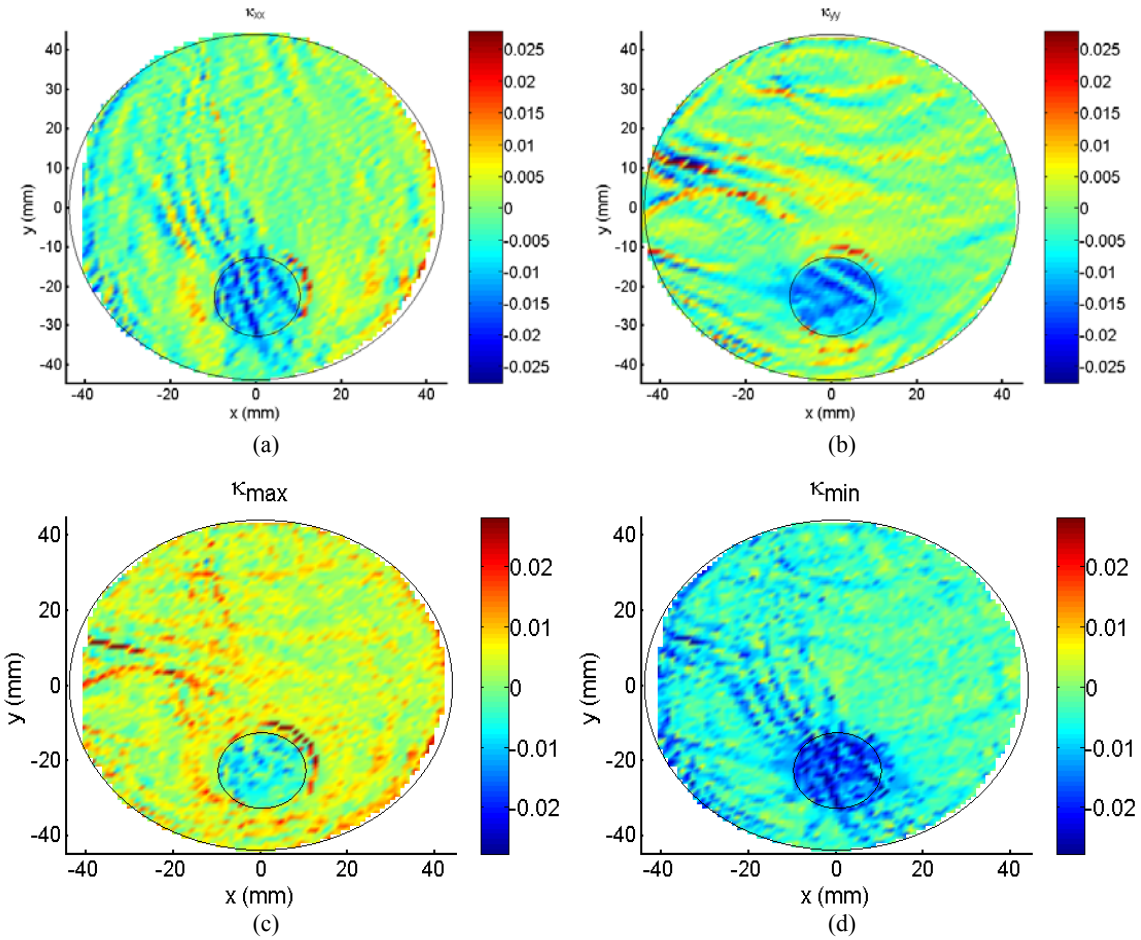

Figure 5-15. Curvature maps κ_{xx}, κ_{yy}, and principal curvature maps κ_{max} and κ_{min} for the off-center film island wafer.

The sum of stresses obtained from the Stoney and HR analyses are shown in Fig. 5-16. In Fig. 5-17, the stresses are displayed along the same diameter as the one that was used to display the slope in Fig. 5-14. Once again, near the film edge there is an intensification of film stress. The stress sum predicted by the Stoney analysis is slowly varying, while the HR methodology shows stronger variations throughout the film.

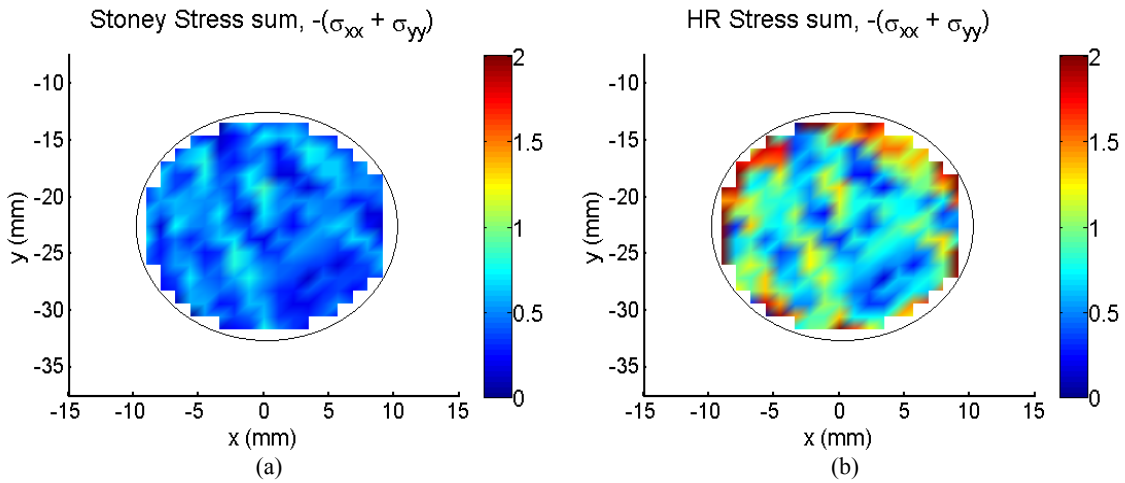

Figure 5-16. HR and Stoney stress sum ($\sigma_{xx} + \sigma_{yy}$) maps.

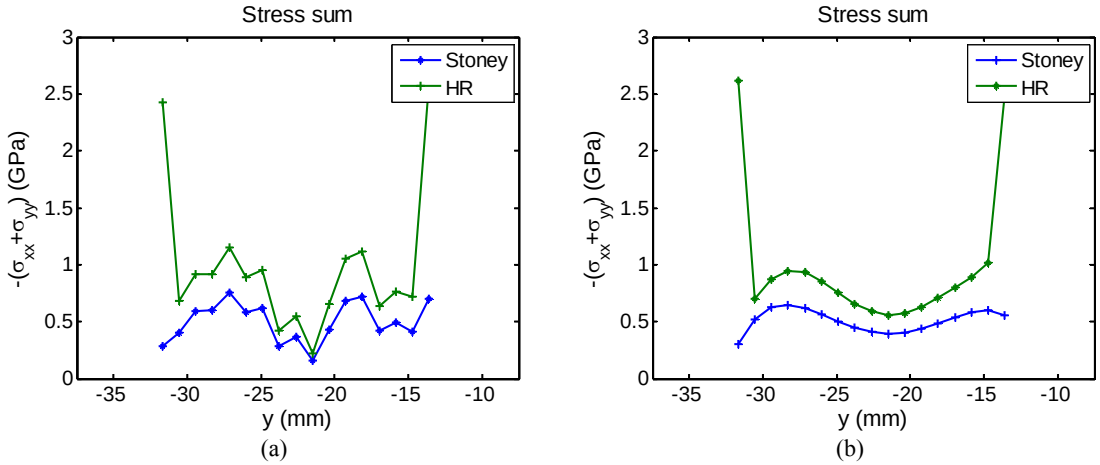

Figure 5-17. Stress along the diameter $x = 0$, a) data and b) polynomial fit for ease of comparison.

The interfacial shear stresses, τ_r and τ_θ, were also calculated, and are shown in Fig. 5-18.

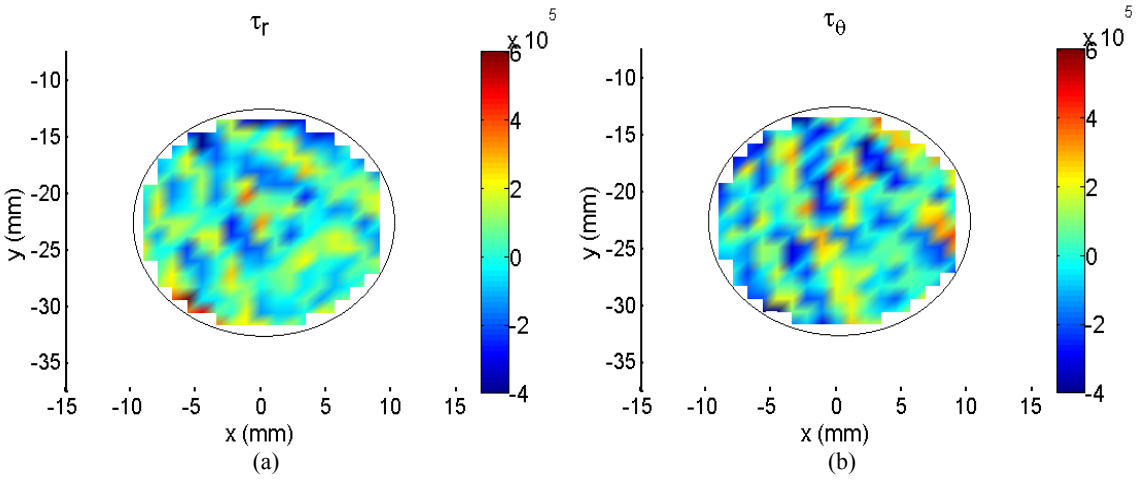

Figure 5-18. Interfacial shear stress

Comparison: Central vs. Off-Center Film Islands

Comparing the results of these two sets of measurements reveals some interesting characteristics. The slopes of the centered and off-center island wafers along the *y*-diameter are plotted in Fig.5-19. Negative *y* corresponds to points at the bottom of the wafer, while positive *y* corresponds to points at the top.

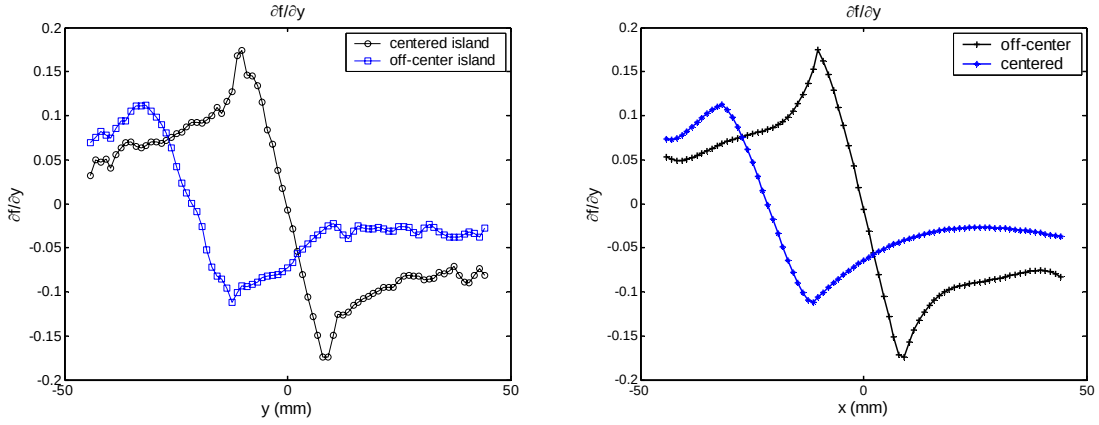

Figure 5-19. Comparison of slope ($\partial f/\partial y$) of centered and off-center islands.

Although the basic shape of the slope profile is consistent between the two wafers, note that the region of linear slope is not in the same location on the two wafers. Indeed, the slope linearity occurs where the island film is located, which is in the center

of one wafer but near one edge of the other. Also, the amount of slope change over the wafer diameter is much less for the off-center wafer than it is for the central one.

The maximum curvature maps are shown in Fig. 5-20. The magnitude of the maximum curvature is much larger in the case of the central film island. Also, there is more of a pronounced jump in curvature at the ring located just outside the edge of the central island. By inspecting these maps, and considering that the film thickness profile which was used in the analysis is the same for the two wafers, the average stress in the central island is expected to be larger than in the off-center island.

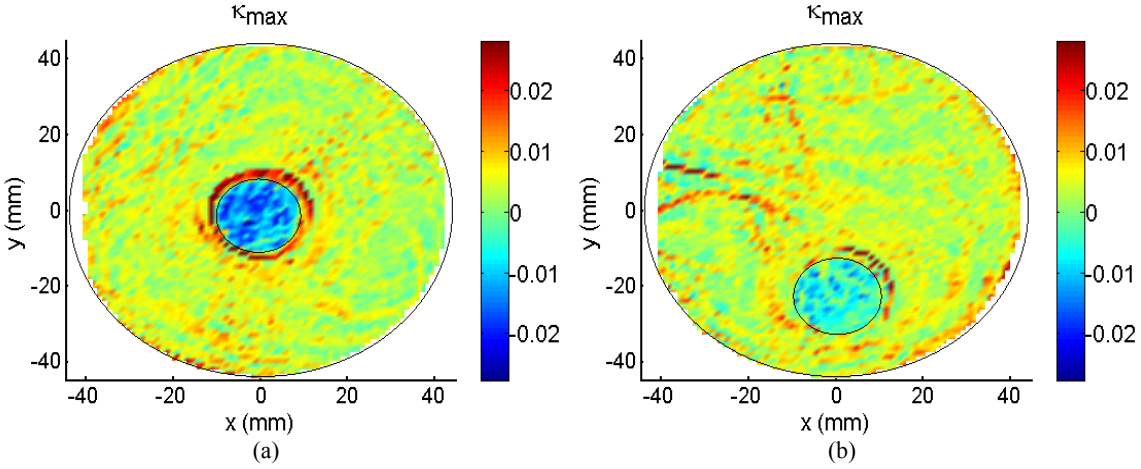

Figure 5-20. Maximum curvature maps for the central (a) and off-center (b) film island wafers.

The sum of stresses obtained from the HR analysis for the central and off-center film island wafers are shown in Fig. 5-21. As expected, the magnitude of stress is much greater for the central film island.

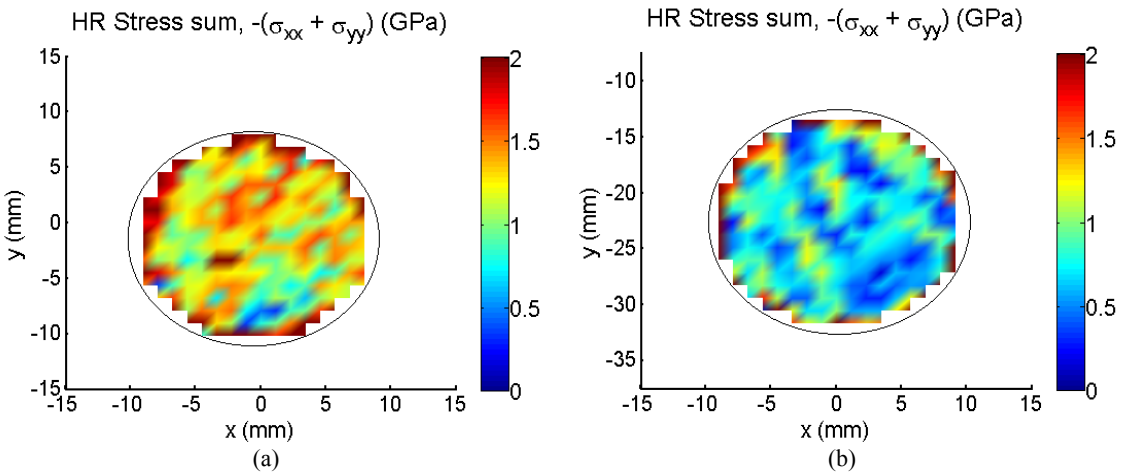

Figure 5-21. HR stress sum maps for the (a) central and (b) off center film island wafers.

A line through the same diameter ($x = 0$) was also extracted from both the HR and Stoney stress maps. The comparison is displayed in Fig. 5-22. As the curvature within the island-covered region of the wafer was greater for the central film island than that for the off-center island, so is the general level of stress inferred by both analyses. However, the stress profile across the island itself varies between the two wafers. Both wafers exhibit strong variations in stress. This is mostly the case near the film edge, where the film thickness decreases quickly. However, even within the middle portion of the film island there is a varying stress distribution. The differences in average stress levels between the two cases (central versus edge islands) could be attributed to the location of the island in relation to the substrate boundary. It can perhaps be hypothesized that the higher stresses of the central island are a result of the higher level of in-plane constraints experienced by the film in this case.

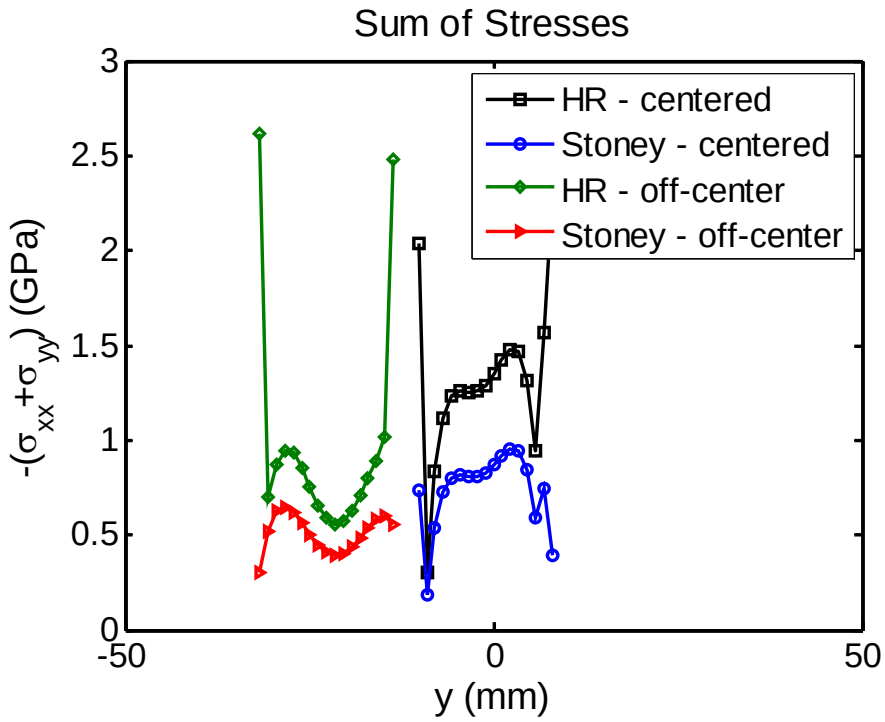

Figure 5-22. HR and Stoney stresses along x=0 for the central and off-center film island wafers.

Figure 5-23 displays the difference between the stress states inferred by the Stoney and HR stress/curvature relations. Near the film edge, of course, the difference between the two methodologies is quite large and is due to the fact that only the HR analysis is capable of including the effects of thickness change. Over the rest of the film island, however, the difference between the Stoney and HR stresses is not simply a fixed percentage of the stress magnitude, but also depends on the location of the island on the wafer. Not only is the stress inferred from the HR analysis greater in the central film island than in the off-center island, but also the difference between the HR and Stoney stresses is greater in this case.

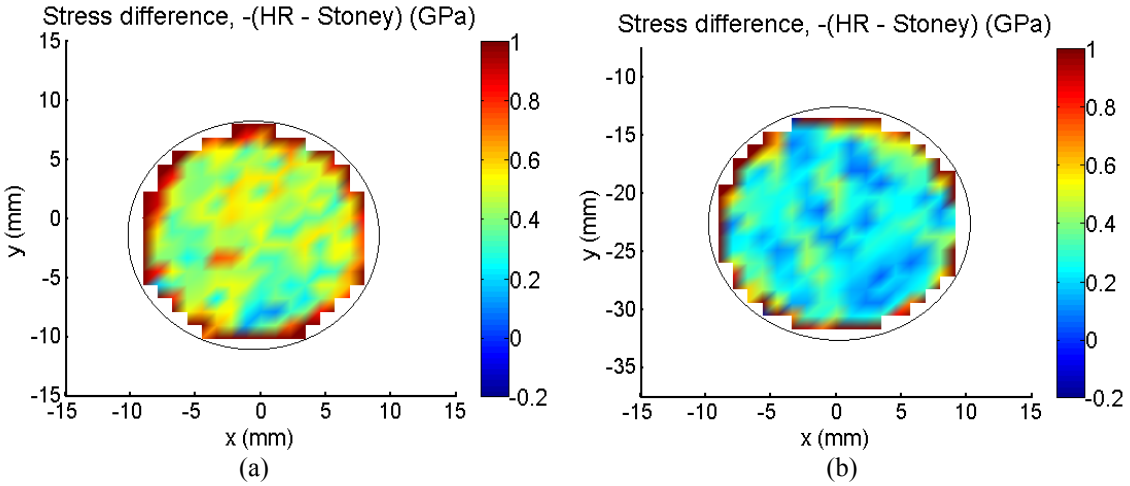

Figure 5-23. Maps of the difference between the stress sum determined by the HR and Stoney analyses, for (a) the central and (b) the off-center film island wafers.

The comparison between these two wafer geometries shows that stress is not simply an intrinsic material parameter which is only determined by deposition conditions and processing. Instead, stress is a film/substrate system property and there is an additional relationship between the location of a specific feature on the wafer and the stress in that feature. For this reason, it is imperative to have a measurement technique such as CGS which can measure full wafer curvatures and can be used in conjunction with non-local stress/curvature relations such as the HR relations.

Examples from a More Complex Film Geometry

In addition to the effects of the location on a wafer of a single film feature, there are additional interactions that may occur when features are placed in proximity to each other. In order to examine these effects, the final idealized specimen geometry chosen for this study consists of a wafer with an array of four film islands. The resulting slope maps are shown in Fig. 5-24.

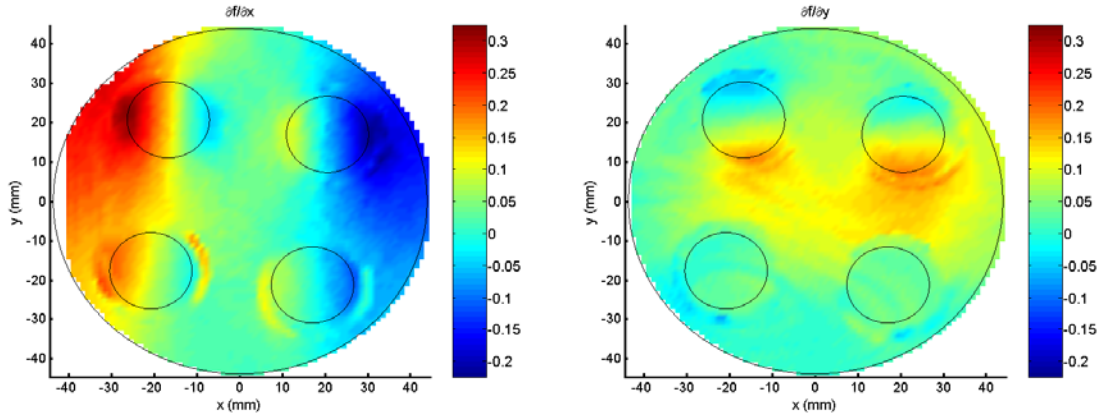

Figure 5-24. Slope maps (a) *∂f/∂x* and (b) *∂f/∂y*.

The horizontal slope, *∂f/∂x*, of this wafer is displayed in Fig. 5-25, and is overlaid with a line that represents the linear dataset which was extracted from this map for comparison with the first two wafers. Since the four islands are not located on either centerline of the wafer, a line through the island diameter was chosen. This slope profile is also plotted in Fig. 5-25b. This line spans two film islands. The slope of each can clearly be identified as the linear portions of the profile.

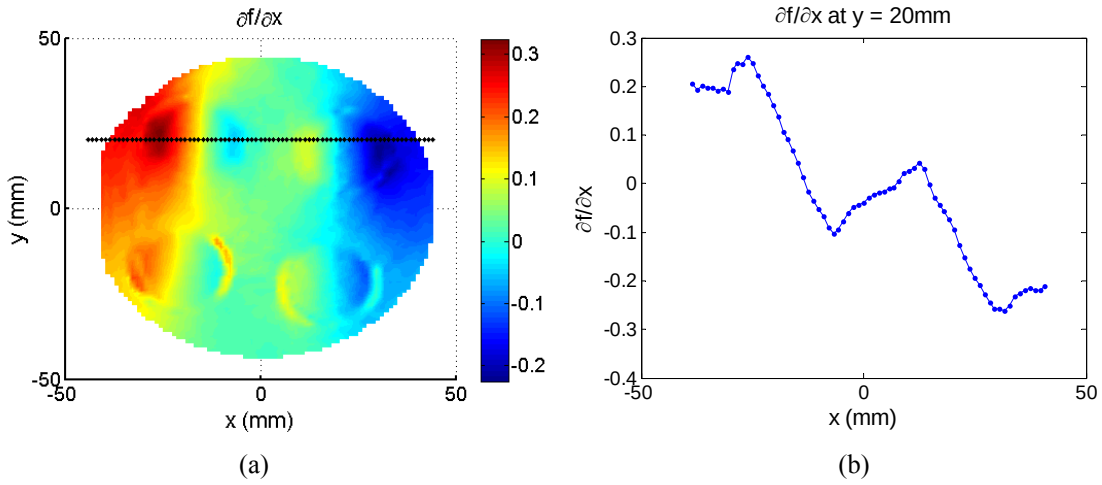

Figure 5-25. Horizontal slope map, *∂f/∂x*, of four island wafer with line indicated where data was extracted, and the extracted slope at $y = 20$ mm.

The horizontal slope map of the off-center island wafer is shown in Fig. 5-26. In order to compare a linear dataset with the slope plotted in Fig. 5-25b, a line was chosen

that is the same distance from the wafer centerline and also goes through the island diameter. Note that in this case the island is in the center of the extracted dataset. In Fig. 5-26b, the slope of the off-center island wafer is compared with the slope extracted in Fig. 5-26b.

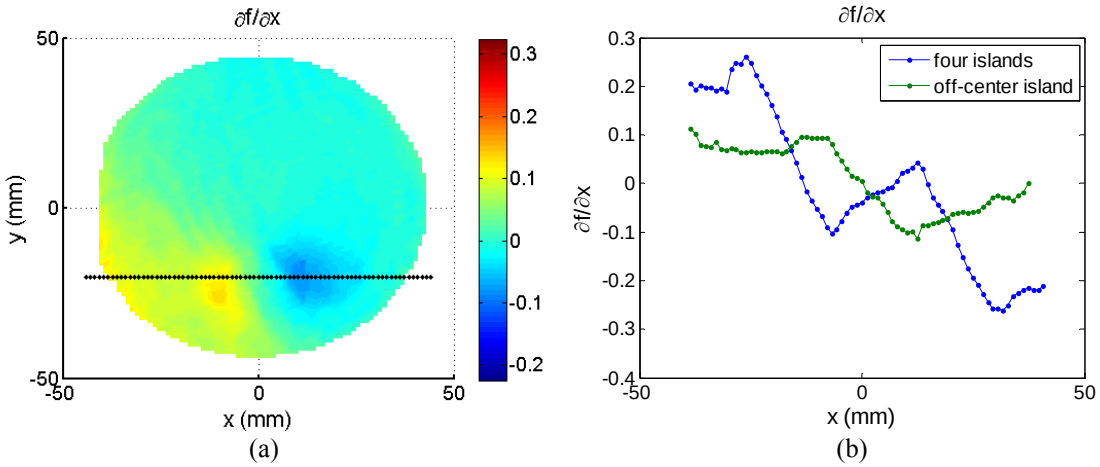

Figure 5-26. Horizontal slope map, $\partial f/\partial x$, of the off-center island wafer and comparison of extracted slope line at y = -20 mm with slope from four island wafer.

The horizontal slope map of the central island film wafer is shown in Fig. 5-27. Since this island is in the center of the wafer, a line through the wafer diameter was extracted to compare with the four island wafer. The two datasets are at different locations on the wafer, but both pass through their respective film island diameters.

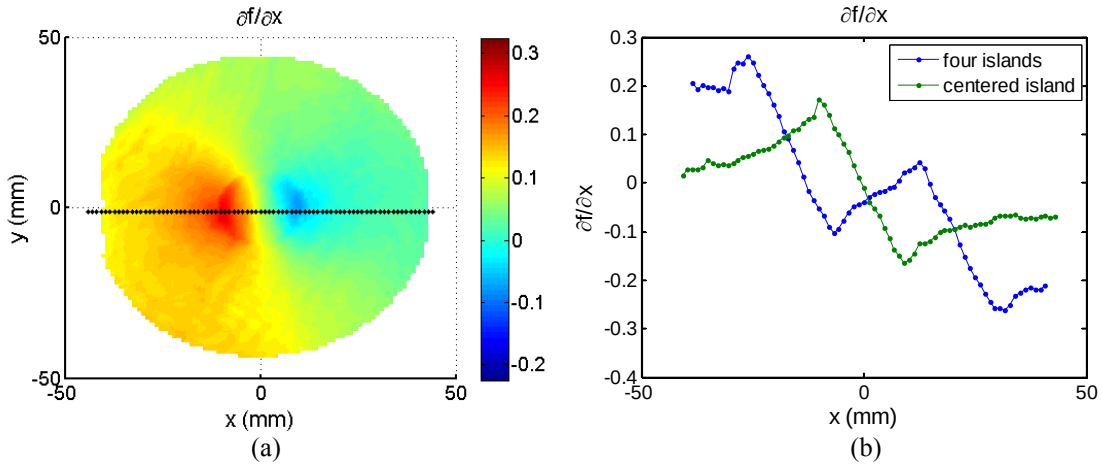

Figure 5-27. Horizontal slope map, $\partial f/\partial x$, of centered island wafer and comparison of extracted slope line at $y = 0$ mm with slope from four island wafer.

Note that in all cases the shape of the slope profile within each film island is similar. Outside each film island, however, the slopes differ from one geometry to another. For a single film island, the slope at the island edge changes abruptly, and then curves back down to a constant value. In the space between the two islands that lie on the line of extracted data from the four island array wafer, however, the slope is not allowed to develop in a similar manner. The slope profile does display the distinctive sharp change in direction, and the line begins to curve away from the islands as expected, but the slope never reaches a constant value. Instead, the two islands interfere with each other to produce a close to linear region of slope between them.

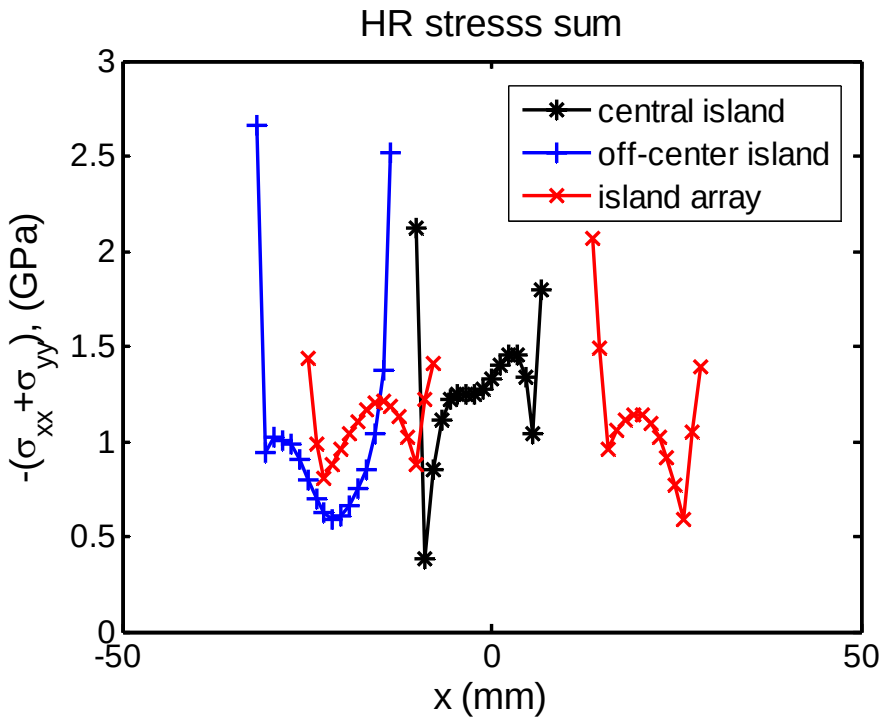

Figure 5-28. Comparison of the HR stress sum for the central island, off-center island, and four island array wafers.

The stresses from the three wafers along the extracted linear datasets are compared in Fig. 5-28. The stress intensifications near the film edge, which exist for all the film islands due to the decreasing film thickness in that region, are present in all cases. The stress level and distribution across the middle of the island, however, vary with position on the wafer, with the central island always featuring the higher average stress levels.

In this chapter, three wafers with varying geometries of W island films were studied using CGS. The delta slope and curvature maps were first obtained. From these, the stress was determined using both the Stoney and the new HR methodologies. The HR analysis generally produces an intensified stress as compared to Stoney. Near the film edge, where the thickness is greatly reduced, the differences between the Stoney and HR analyses are dramatic. This study shows that there is a noticeable effect of film feature

geometry on wafer deformation. Also, both the stress intensity and film stress profile reveal a strong dependence on the location of the feature on the wafer with higher stresses developing in islands deposited at the wafer center. Finally, a more complex case was chosen to consider the interactions between features which lead to additional changes in wafer deformation and film stress.

6. Ongoing Work: Collaboration with Northrop Grumman Space Technologies

A study in collaboration with Northrop Grumman Space Technologies, furthering the investigation the effects of spatial non-uniformities on the measurement of film stress, is currently underway. The original goal of this study was twofold: to compare CGS measurements with the NGST standard measuring techniques, and to utilize the new HR relations, instead of just using the classical Stoney formula, to determine the stress distribution in "real," industrial standard, wafers. Ideally, this could also culminate in the modification of the standard measurement methodologies to eventually incorporate the HR relations in new metrology tools.

The specimens used in this study consist of 625 μm thick, 3" diameter GaAs wafer substrate with blanket InGaAs films deposited on them. Varying the thickness and composition of InGaAs changes the amount of relaxation in the film, and specimens with different amounts of film relaxation were produced.

The initial stress analysis results were quite unexpected and seemed physically impossible. Since the lattice parameter of InGaAs is greater than that of the GaAs substrate, the film should only be negatively strained. The preliminary stress results, however, indicated a large variation in film stress across the wafer that ranged from negative to positive values. The specimens and processing conditions were, therefore, examined more closely.

The analysis of film stress due to some process requires full-field delta curvature maps, i.e, the difference in curvature before and after that particular process is performed.

It is implicitly assumed that the resulting change in curvature is caused solely by the film stress.

However, when temperature gradients exist in a wafer, stresses are induced by the uneven thermal expansion within the substrate itself. If the gradients are large enough, the resulting stresses can surpass the yield stress of the material and be locked in, i.e., cause permanent deformation in the wafer even without the action of a film. This effect would occur individually in both the film and the substrate even if these two constituents were not bonded together, and the resulting wafer deformation is in addition to that caused by stresses induced in the film due to a difference in coefficients of thermal mismatch between the film and substrate.

In compound semiconductors, film deposition often occurs at high temperatures. There may be non-uniformities in the thermal chambers that result in temperature gradients during the heating process. Even if such non-uniformities in heating do not exist, the cooling process is often uncontrolled, and is inherently non-uniform.

For the GaAs wafers being studied, it was hypothesized that the thermal effects due to processing, which were not being considered in the analysis, might be an additional cause of substrate deformation. This would throw off the film stress results, since that analysis only allows for deformation caused by film stress. To determine whether this was the case, a bare GaAs wafer was put through the same processing conditions (i.e., the same thermal environment) as the other specimens, using the exact same equipment, but without actually depositing a film. The wafer was measured with CGS before and after processing to see whether there was deformation of the substrate apart from that caused by the film.

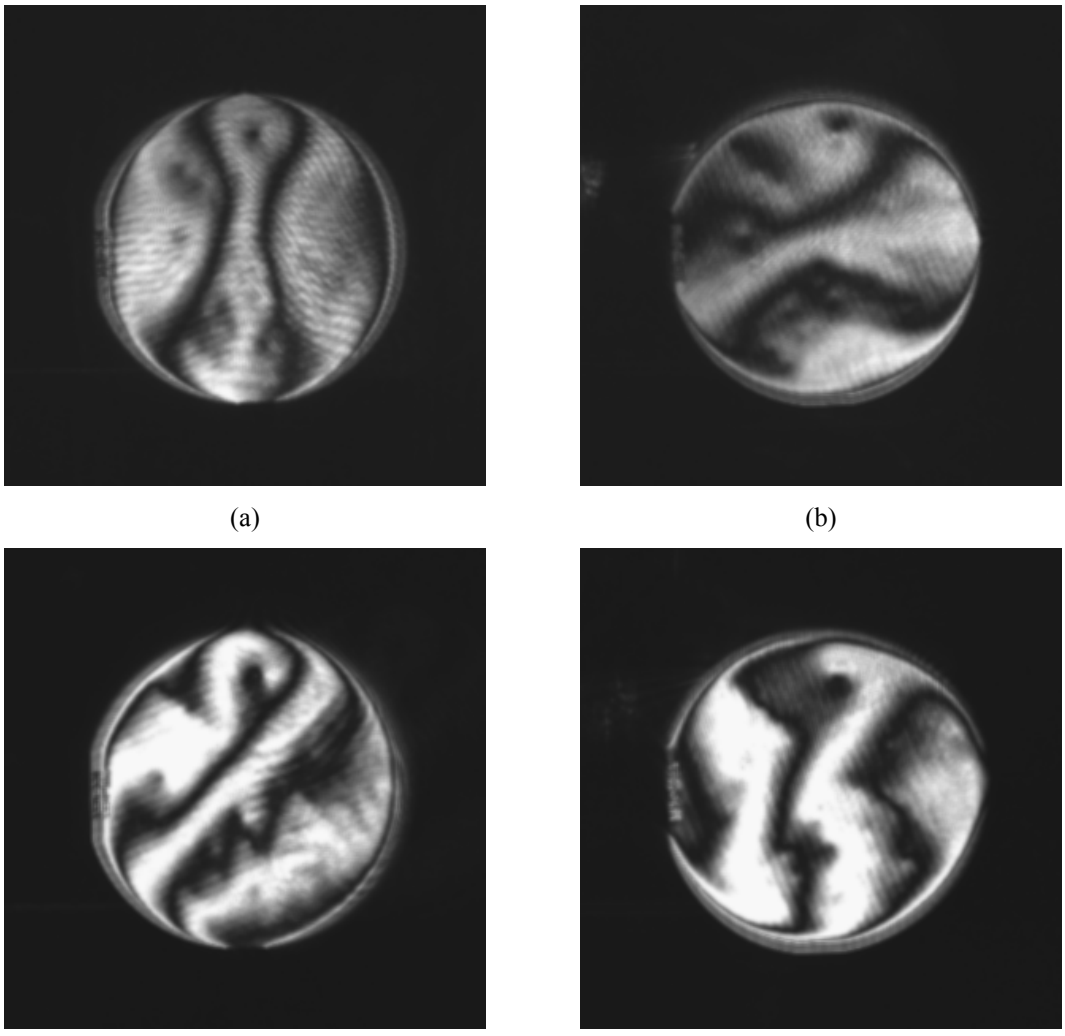

(a) (b)

(c) (d)

Figure 6.1. CGS slope interferograms of the bare substrate before and after processing: (a) $\partial f/\partial x$ before, (b) $\partial f/\partial y$ before; (c) $\partial f/\partial x$ after, (d) $\partial f/\partial y$ after.

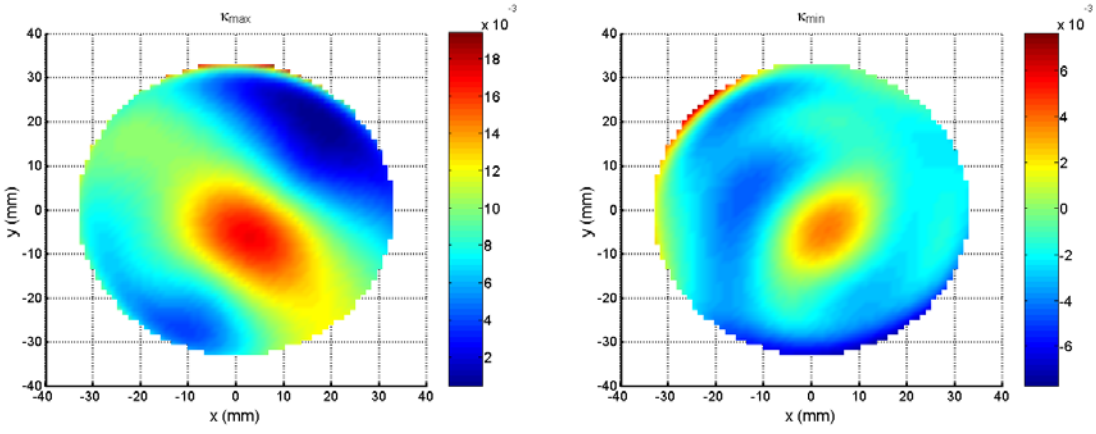

(a) (b)

Figure 6.1. CGS principal curvature maps of delta curvature, (a) κ_{max} and (b) κ_{min}.

The CGS slope interferograms demonstrate that the processing was, in fact, causing permanent deformation in the substrate wafer itself. This permanent deformation which is clearly due to thermal gradients must also be considered in determining film stress on the affected wafer.

This study, therefore, has morphed from one examining only the effects of a partially relaxed film, i.e., a spatially varying misfit strain, to one that also must consider effects of a temperature gradient on the substrate deformation. Relations between curvature and stress have been derived for the case of temperature gradient-induced stresses [14]. The ongoing work consists of merging this analysis with the methodology considered elsewhere in this thesis, to consider the effects of temperature gradients in addition to those of misfit strain in the thin film-wafer substrate system deformation and resulting stress distribution.

Conclusions

This thesis has focused on establishing a validated methodology for inferring thin film stresses in the presence of spatially non-uniform film thickness and misfit strain. A configuration of central importance in many areas of engineering application consists of a thin film structure composed of one or more materials deposited on a substrate of yet another material. Especially as feature sizes continue to grow smaller, buildup of stresses in the thin film causes deleterious effects on process yield, since stress can lead directly to film failure. Film stress is accumulated during each of the many processes required to build a film structure. Some mechanisms by which stress causes failure include delamination, voiding, and cracking of the film.

Since stress cannot be measured directly, a common method for quick stress inference is to measure the change in substrate curvature due to some process and apply appropriate relations that connect curvature to stress in order to determine the film stress from that process. The relation generally used for this is called the Stoney formula, which has been derived based on several quite restrictive assumptions. The assumptions include, among others, constant film thickness, and constant misfit strain over the entire wafer surface. A spatially constant film thickness and misfit strain implies spatially constant curvature and stress components which are not allowed to vary over the wafer surface. In practice, these assumptions are rarely met, and yet the Stoney analysis is still, arbitrarily, applied.

Recently an analysis was performed which relaxed the assumptions of spatial uniformity, and Stoney-like relations between film stress and system curvature were

established. An interesting outcome of this analysis was that the relation connecting film stress and curvature at a given in-plane location depends not only on the curvature at that particular location, as expected by the Stoney analysis, but also involves important terms that include integrals of curvature across the entire wafer. Therefore, full-field curvature information is absolutely necessary to determine film stress, even at a single location.

This methodology was validated by comparison with μXRD measurements. The μXRD technique used here involved two independent types of measurements: one that estimates film stress from measurements of lattice spacing change, and one that estimates substrate curvature. Since these two measurements are not related to each other, they can both be used as both input to the analysis and the benchmark against which to test it. Specifically, the μXRD measurement of substrate curvature was used as an input to the HR relations, and also to Stoney, to determine film stress based on each of the two methodologies. These film stresses were then compared with the μXRD measurements of film stress to determine whether the HR relations were an improvement over Stoney. It was found that, indeed, the stresses determined using the HR methodology are much closer to the μXRD data, both in predicting general level throughout the film feature and in capturing the stress increase near the film edges. Near the film edges, where the film thickness drops drastically, the HR relations were able to capture the resulting increase in film stress which Stoney completely misses.

The HR relations require curvature information over the entire system. Following their validation, Coherent Gradient Sensing, an optical measurement technique, was introduced as a convenient alternative to μXRD measurements. This technique is

uniquely suited to the HR methodology since it has the ability of capturing instantaneous full-field information.

Finally, CGS measurements were made of several test wafers with increasingly more complex geometries. The location of a feature in relation to the substrate center or boundaries was found to have an effect on the stress level and spatial distribution within that feature. Also, it was found that neighboring film features interfere with each other, which has an effect both on the wafer deformation and film stress distribution within the features. This indicates that film stress is not simply an intrinsic material or film processing property. Instead, it depends strongly on details of geometry of the entire thin film - substrate system.

Further studies are underway which also consider an additional source of wafer deformation, namely the effects of temperature gradients which can cause permanent deformation in a wafer substrate. This effect is completely separate from those caused by film stress.

References

1. The National Technology Roadmap for Semiconductor Technology (2003)
2. Stoney, G. G., The tension of metallic films deposited by electrolysis. *Proc. R. Soc. Lond.* A82, 172-175 (1909).
3. Freund, L. B., and S. Suresh, *Thin Film Materials: Stress, Defect Formation and Surface Evolution.* Cambridge University Press, Cambridge, UK, (2004).
4. Wikstrom, A., P. Gudmundson, and S. Suresh, Thermoelastic analysis of periodic thin lines deposited on a substrate. *J. Mech. Phys. Solids* 47, 1113-1130 (1999).
5. Shen, Y. L., S. Suresh, and I. A. Blech, Stresses, curvatures, and shape changes arising from patterned lines on silica wafers. *J. Appl. Phys.* 80, 1388-1398 (1996).
6. Wikstrom, A., P. Gudmundson, and S. Suresh, Analysis of average thermal stresses in passivated metal interconnects. *J. Appl. Phys.* 86, 6088-6095 (1999).
7. Park, T. S. and S. Suresh, Effects of line and passivation geometry on curvature evolution during processing and thermal cycling in copper interconnect lines. *Acta Mater.* 48, 3169-3175 (2000).
8. Masters, C. B. and N. J. Salamon, Geometrically nonlinear stress-deflection relations for thin film/substrate systems. *Int. J. Engrg. Sci.* 31, 915-925 (1993).
9. Salamon, N. J. and C. B. Masters, Bifurcation in isotropic thin film/substrate plates. *Int. J. Solids Struct.* 32, 473-481 (1995).
10. Finot, M., I. A. Blech, S. Suresh, and H. Fijimoto, Large deformation and geometric instability of substrates with thin-film deposits. *J. Appl. Phys.* 81, 3457-3464 (1997).
11. Freund, L.B., Substrate curvature due to thin film mismatch strain in the nonlinear deformation range. J. *Mech. Phys. Solid*s 48, 1159 (2000).
12. Lee, H., A. J. Rosakis, and L. B. Freund, Full-field optical measurement of curvatures in ultra-thin-film/substrate systems in the range of geometrically nonlinear deformations. *J. Appl. Phys.* 89, 6116-6129 (2001)

13. Park, T. S., S. Suresh, A. J. Rosakis, and J. Ryu, Measurement of full-field curvature and geometrical instability of thin film-substrate systems through CGS interferometry. *J. Mech. Phys. Solids* 51, 2191-2211 (2003).

14. Huang, Y. and A. J. Rosakis, Extension of Stoney's formula to non-uniform temperature distributions in thin film/substrate systems. The case of radial symmetry. *J. Mech. Phys. Solids* 53, 2483-2500 (2005).

15. Huang, Y., D. Ngo, and A. J. Rosakis, Non-uniform, axisymmetric misfit strain in thin films bonded on plate substrates/substrate systems: the relation between non-uniform film stresses & system curvatures. *Acta Mech. Sin.* 21, 362-370 (2005)

16. Ngo, D., Y. Huang, A. J. Rosakis, and X. Feng, Spatially non-uniform, isotropic misfit strain in thin films bonded on plate substrates: the relation between non-uniform film stresses and system curvatures. *Thin Solid Films* 515, 2220-2229 (2006)

17. Ngo, D., X. Feng, Y. Huang, A. J. Rosakis, and M. A. Brown, Thin film/substrate systems featuring arbitrary film thickness and misfit strain distributions: Part I. Analysis for obtaining film stress from non-local curvature information. *Int. J. Solids Struct.* 44, 1745-1754 (2006)

18. Noyan, I.C., and J. B. Cohen, *Residual Stress: Measurement by Diffraction and Interpretation*. Springer-Verlag, New York (1987).

19. Tamura, N., A. A. MacDowell, R. Spolenak, B. C. Valek, J. C. Bravman, W. L. Brown, R. S. Celestre, H. A. Padmore, B. W. Batterman, and J. R. Patel, Scanning X-ray microdiffraction with submicrometer white beam for strain/stress and orientation mapping in thin films. *J. Synch. Rad.* 10, 137-143 (2003)

20. Brown, M., A. J. Rosakis, X. Feng, Y. Huang, and E. Üstündag, Thin film/substrate systems featuring arbitrary film thickness and misfit strain distributions: Part II. Experimental validation of the non-local stress/curvature relations. *Int. J. Solids Struct.* 44, 1745-1754 (2006).

21. Gouldstone, A., Y-L. Shen, S. Suresh, and C.V. Thompson, Evolution of stresses in passivated and unpassivated metal interconnects. *J. Mat. Res.* 13, 1956-1966 (1998).

22. Rosakis, A. J., R. P. Singh, Y. Tsuji, E. Kolawa, and N. R. Moore, Jr., Full-field measurements of curvature using coherent gradient sensing: application to thin film characterization. *Thin Solid Films* 325, 42-54 (1998).

23. Park, T. S., and S. Suresh, Effects of line and passivation geometry on curvature evolution during processing and thermal cycling in copper interconnect lines. *Acta Mater*. 48, 3169-3175 (2000).

24. Park, T. S., M. Dao, S. Suresh, A. J. Rosakis, D. Pantuso, and S. Shankar, Some practical issues of curvature and thermal stress in realistic multi-level metal interconnect structures. Submitted to *J. Elect. Mat.*

25. Rosakis, A. J., Park, T. S., and S. Suresh, Analytical and numerical modeling of stress in multi-level interconnect structures and vias. Submitted to *Solid Thin Films.*

26. Mason, J.J., J. Lambros, and A. J. Rosakis, The use of a coherent gradient sensor in dynamic mixed-mode fracture mechanics experiments. *J. Mech. Phys. Solids* 40, 641-66 (1992).

27. Tippur, H.V., S. Krishnaswamy, and A. J. Rosakis, A coherent gradient sensor for crack tip deformation measurements: analysis and experimental results. *Int. J. Fract.* 48, 193-204 (1991).